2008

Advances in Magnetic Resonance Electrical Impedance Mammography

Nataliya Kovalchuk
University of South Florida

Advances in Magnetic Resonance Electrical Impedance Mammography

by

Nataliya Kovalchuk

A dissertation submitted in partial fulfillment
of the requirements for the degree of
Doctorate of Philosophy
Department of Physics
College of Arts and Sciences
University of South Florida

Co-Major Professor: John J. Heine, Ph.D.
Co-Major Professor: David A. Rabson, Ph.D.
Ernest Wollin, M.D., P.E.
Maria Kallergi, Ph.D.
Sarath Witanachchi, Ph.D.
Pritish Mukherjee, Ph.D.

Date of Approval:
April 4, 2008

Keywords: Electrical Impedance Imaging, Magnetic Resonance Imaging simulations, Boundary Value Problem, breast phantom, breast tissue conductivity

Dedication

To my precious family: my mother Olena for constant encouragement, support, care, and prayers, my father Bohdan for nurturing my love for sciences and continuous interest in my research, my brother Nazar for his motivation and love.

Acknowledgments

I would like to express my gratitude to all those who have contributed in any way, shape or form to the completion of this dissertation. First of all, I would like to thank my advisors, Ernest Wollin, John Heine, Maria Kallergi, and David Rabson. My thanks also go to all the members of the Graduate Committee for reading this work and providing many valuable comments that improved the presentation and contents of this dissertation.

Dr. Kallergi has given me an opportunity to join the Digital Medical Imaging Group at the H. Lee Moffitt Cancer Center although I had very little experience in this area. She served as an example for me being such a versatile intellectual with a warm and, at the same time, strong personality. Dr. Kallergi inspired and motivated me with her enthusiasm and encouragement throughout my graduate studies.

Dr. Heine has overtaken the hardships of being my immediate supervisor after Dr. Kallergi left for Greece. His guidance in computer simulation was essential to the completion of this dissertation.

Dr. Rabson has agreed to be my Co-advisor at physics department and became a corner-stone in all the problems and roadblocks that unavoidably crop up in the course of performing research. My studies at University of South Florida would not be possible without his help with visa documentation. His response to all my questions and requests approached the time of e-mail delivery. I was always amazed with his intellectual abilities that are far beyond my reach.

Dr. Wollin, M.D., P.E., FACR, despite of his numerous titles struck me with a down-to-earth personality: working with him was a great pleasure for me. Magnetic Resonance Electrical Impedance Mammography is his creation, and I just assisted him in its experimental development and testing. He was the major editor of this dissertation helping in its prenatal stages with numerous comments and suggestions. Dr. Wollin deserves my deepest gratitude for his invaluable help in all aspects of this work.

I am also grateful to German Diaz, MR technician, for helping considerably with realizing the experimental tests and Anand Manohar, a member of medical imaging group, for his help in the early stages of this work.

I would also like to thank the Physics Department at USF, especially its representatives Dr. Mukherjee and Dr. Witanachchi, for accepting me to the Applied Physics Ph.D. program and for providing financial support throughout my graduate studies.

Last, but not least, I would like to thank my family for their understanding and love. Their support and encouragement was in the end what made this dissertation possible.

Thank You, oh God, for giving me strength to finish this work. Glory to You for everything You have mercifully revealed to me!

Table of Contents

List of Tables

List of Figures

List of Abbreviations

BI-RADS - Breast Imaging Reporting and Data System
BVP - Boundary Value Problem
CM - Cell Membrane
CNR - Contrast-to-Noise Ratio
CP - Constant Phase
DCIS - Ductal Carcinoma in Situ
ECM - Extra Cellular Medium
EIS - Electric Impedance Scanning
EPI - Echo Planar Imaging
FDM - Finite Difference Method
FID - Free Induction Decay
FOV - Field of View
FP - False Positive
FSs - Faraday Shields
GSE - Gradient Spin Echo
ICM - Intra Cellular Medium
LCIS - Lobular Carcinoma in Situ
MRCDI - Magnetic Resonance Current Density Imaging
MREIM - Magnetic Resonance Electrical Impedance Mammography
MREIT - Magnetic Resonance Electrical Impedance Tomography
MRI - Magnetic Resonance Imaging
MRM - Magnetic Resonance Mammography
NMR - Nuclear Magnetic Resonance
RF - Radiofrequency
ROI - Region of Interest
SDSE - Spin Density Spin Echo
SE - Spin Echo
SNR - Signal-to-Noise Ratio
SOR - Successive Over-Relaxation
TE - Echo Time
TR - Repetition Time
TS - Sampling Time
US - Ultrasound

Advances in Magnetic Resonance Electrical Impedance Mammography

Nataliya Kovalchuk

ABSTRACT

Magnetic Resonance Electrical Impedance Mammography (MREIM) is a new imaging technique under development by Wollin Ventures, Inc. in conjunction with the H. Lee Moffitt Cancer Center & Research Institute. MREIM addresses the problem of low specificity of magnetic resonance mammography and high false-positive rates, which lead to unnecessary biopsies. Because cancerous tissue has a higher electrical conductivity than benign tissue, it may serve as a biomarker for differentiation between malignant and benign lesions. The MREIM principle is based on measuring both magnetic resonance and electric properties of the breast by adding a quasi-steady-state electric field to the standard magnetic resonance breast image acquisition. This applied electric field produces a current density that creates an additional magnetic field that in turn alters the native magnetic resonance signal in areas of higher electrical conductivity, corresponding to cancerous tissue.

This work comprises MREIM theory, computer simulations, and experimental developments. First, a general overview and background review of tissue modeling and electrical-impedance imaging techniques are presented. The experimental part of this work provides a description of the MREIM apparatus and the imaging results of a custom-made breast phantom. This phantom was designed and developed to mimic the magnetic resonance and electrical properties of the breast. The theoretical part of this work provides an extension to the initial MREIM theoretical developments to further understand the MREIM effects. MREIM computer simulations were developed for both idealized and realistic tumor models. A method of numerical calculation of electric potential and induced magnetic field distribu-

tion in objects with irregular boundaries and anisotropic conductivity was developed based on the Finite Difference Method. Experimental findings were replicated with simulations. MREIM effects were analyzed with contrast diagrams to show the theoretical perceptibility as a function of the acquisition parameters. An important goal was to reduce the applied current.

A new protocol for an MREIM sequence is suggested. This protocol defines parameters for the applied current synchronized to a specific magnetic resonance imaging sequence. A simulation utilizing this protocol showed that the MREIM effect is detectable for a 3-mm-diameter tumor with a current density of 0.5 A/m^2, which is within acceptable limits.

Chapter 1

Introduction

According to the World's Health Organization, breast cancer is the most common form of cancer in females, affecting, at some time in their lives, approximately one out of 39 to one out of three women who reach age 90 in the Western world (World Health Organization Cancer Fact Sheet 2006). In 2007, more than 178,000 new female breast cancer cases and about 40,000 breast cancer related deaths were expected in the United States (Breast Cancer Facts and Figures 2007–2008). Worldwide, more than 1.2 million people will be diagnosed with breast cancer each year and over 500,000 will die from this disease (World Health Organization Fact Sheet 2006). **Early detection and diagnosis of breast cancer are critical to its successful treatment and cure.**

According to the American Cancer Society, when breast cancer is confined to the breast, the five-year survival rate approaches 100%. Not only does early detection improve survival, but it also increases the probability that the cancer will be amenable to breast conservation therapy, which benefits the patient by reducing the physical and psychological morbidity of therapy (Esserman, Hylton et al. 1999). Accurate staging of breast cancer ensures that patients receive the correct treatment. Highly specific breast cancer detection methods minimize the risk of unnecessary biopsy or surgery.

Magnetic Resonance Mammography (MRM) has emerged as a promising technique for detecting, diagnosing, and staging of breast cancer (Esserman, Hylton et al. 1999). Despite its advantages, MRM suffers from a low specificity, the necessity of giving intravenous contrast, a long imaging time caused by fat suppression, and expense, which ultimately impacts its use in broader communities (Duchesne, Burbank et al. 2006). Since cancerous breast tissue has a higher electric conductivity than that of benign and normal breast tissue, electric conductivity may be used as a biomarker for detection of cancer (Fricke and Morse 1926; Singh, Smith et al. 1979; Surowiec, Stuchly et al. 1988; Jossinet 1996; Jossinet 1998).

The MREIM goal is to improve breast cancer diagnostics and eliminate unnecessary biopsies representing a novel imaging technology that will provide information about both magnetic and electrical properties of the breast.

The specific goals of this work include the following:

- to collect and analyze the supporting material on the differentiation of normal and malignant breast tissue in terms of electrical conductivity;
- to design and develop a breast phantom that imitates both magnetic resonance and electric properties of normal and cancerous breast tissue;
- to conduct experimental phantom imaging tests;
- to extend the initially developed MREIM theory to broaden understanding of MREIM effects;
- to develop a method for calculation of electric potential and induced magnetic field distribution for a realistic tumor model with tumors of irregular boundaries and anisotropic conductivities;
- to develop MREIM simulation for both idealized and realistic tumor models;
- to replicate experimental phantom imaging results with MREIM simulation;
- to develop a method of quantitative description of MREIM effects;
- to study MREIM effects based on simulation results;
- to suggest sequence protocol that would produce the most conspicuous MREIM effect at the lowest applied electric energy.

The accomplishment of the aims specified above will serve as a prerequisite for further MREIM developments, clinical testing, and commercial development. When fully developed, MREIM has potential to detect breast cancer in early stages, decreasing the false-positive rate for MRM and eliminating unnecessary invasive, costly, and distressing biopsies.

This dissertation contains ten Chapters. The Introduction outlines problems in current breast cancer diagnostics, a proposal for a new imaging technique that is capable of resolving these problems, and a list of specific aims for the course of this work. The second

Chapter discusses the current breast diagnostic imaging. The third Chapter provides a thorough review of bio-impedance research on electrical properties of malignant and normal breast tissue, since its differentiation in terms of electrical conductivities serves as a core for MREIM developments (Heine, Kovalchuk et al. 2008a). Chapter 4 reviews the current imaging modalities based on electrical impedance measurements and the MREIM's potential to overcome their limitations. Chapter 5 briefly explains the fundamentals of Magnetic Resonance Imaging required to grasp the theoretical concepts of MREIM. In the sixth Chapter, the theoretical development for the initial MREIM study is provided (Heine, Kovalchuk et al. 2008b) and extended to further understanding of the MREIM effect on native MRI image formation. The Chapter also includes the model developed to solve a Dirichlet Boundary Value Problem (BVP) of finding electric potential and the induced magnetic field distribution for realistic tumor model with irregular shapes and anisotropic conductivities. Chapter 7 elaborates on the experimental developments and provides breast phantom imaging results. In Chapter 8, the MREIM simulation and BVP solution algorithms and contrast method for finding MREIM effect detectability are provided. This Chapter also presents the replication of experimental results. The MREIM effect study based on the SDSE sequence and the simulation images for both analytical and numerical solution of MREIM fields. Chapter 9 dwells on further investigation of MREIM effects, outside the MRI sequence used in experiment, to lower the applied current necessary to obtain a detectable MREIM effect. It provides the MREIM protocol utilizing which it is possible to obtain detectable MREIM signal at safe applied current limits. A summary of this work and of its results is presented in the Conclusion along with the author's perspective.

Chapter 2

Significance

2.1 Current Stage of Breast Diagnostic Imaging

Most breast cancers are diagnosed by mammography, but early cancers can be difficult to detect within the complex architecture of the breast. Research has shown that 10% to 30% of breast Magnetic Resonance Imaging (MRI) visible cancers are overlooked in mammography (Walsh and Lee 1991; Heywang, Viehweg et al. 1997). Human factors related to perception and interpretation also contribute to false negative mammograms. Classification errors are detrimental to the patient and costly to the health care system. Although the mammogram remains the only test that has been proven to reduce mortality due to breast cancer, it is limited in cases with dense breasts, augmented breasts, and breasts that have undergone breast conservation surgery and radiation therapy. The high false negative rate of mammography has prompted investigation into other imaging modalities.

Out of all imaging techniques, breast Magnetic Resonance Imaging has the highest sensitivity and provides information about tissue vascularity that is not available from mammography (Morris 2006). Breast MRI performed for cancer detection requires the use of intravenous contrast agent, such as Gadolinium-DTPA, which is taken up by areas of the breast with the increased vascularity. Malignant lesions exhibit an increased number of blood vessels and increased vascular permeability due to leaky endothelial cells (Morris 2006). When contrast is injected, malignant lesions will generally enhance rapidly and strongly. Malignant lesions also demonstrate wash-out that is defined as a decrease of enhancement after the peak has been reached. Wash-out is thought to result from increased vascular permeability and the presence of arterio-venous shunts (Morris 2006). In general, the breast cancers enhance more rapidly and wash out faster than benign lesions. Alas, infiltrating lobular carcinoma, medullary carcinoma, and ductal carcinoma in situ can

demonstrate slow uptake of contrast and no wash-out, mimicking a benign lesion (Morris 2006). Conversely, false-positive examinations can be seen in all types of benign pathology such as fibroadenomas, recent scars, inflammations, proliferative and non-proliferative changes, atypia, sclerosing adenosis, and lobular carcinoma in situ. Any breast pathology with increased vascularity will demonstrate enhancement; therefore, when interpreting breast MRI exams, one cannot rely on enhancement alone. Kinetic and morphologic features of enhancement help to decide which lesions warrant biopsy and which lesions should be imaged with Ultrasound and/or monitored in the future. False-positive findings pose a significant problem in the interpretation of breast MRI. The rate of false positives varies greatly in the literature, and reported specificity ranges from 37% to 100% (Morris 2006). High false-positive rate, necessity of giving intravenous contrast, long imaging time caused by fat suppression, and expense of breast MRI ultimately impact its broader use.

Table 1: The BI-RADS distribution of x-ray mammography in 2004–2006 performed at H. Lee Moffitt Cancer Center (personal communication with Heine J J). Values in parenthesis show the number of malignancies. Generally, BI-RADS 4 and 5 are warranted to be biopsied. Approximately 80% of BI-RADS 4 and 20% of BI-RADS 5 are benign.

BI-RADS	0 Incomplete	1 Negative	2 Benign	3 Probably Benign	4 Suspicious Abnormality	5 Highly Suspicious of Malignancy
2004	131(7)	1316(0)	5899(1)	474(0)	416(84)	84(68)
2005	212(10)	1229(0)	6191(0)	433(2)	296(50)	70(55)
2006	368(14)	1008(0)	6032(6)	478(1)	275(47)	58(46)

Table 1 is a vivid illustration of the area in breast cancer diagnostics which requires improvement. The term BI-RADS (Breast Imaging Reporting and Data System) refers to the mammography assessment categories (Breast Imaging Reporting and Data System Atlas 2007). BI-RADS 4 and 5 are the particular cases that necessitate an adjunctive diagnostic technique to eliminate unnecessary biopsies. As a result of high false-positive rate of breast

mammography, a high number of biopsies lead to negative histology — out of five patients that undergo biopsy, only one tissue sample leads to malignant histological diagnosis (Chen, Lehman et al. 2004).

2.2 MREIM as a Potential Diagnostic Technique

The proposed MREIM technique may address several limitations of MRM and, if used as an independent imaging modality, it has a potential to revolutionize current breast cancer diagnostics by

- reducing the number of False Positives (FP) by introducing an additional parameter in imaging, electrical conductivity;
- eliminating many unnecessary invasive, costly, and stressful biopsies;
- making breast MRI more cost-effective and less time consuming by excluding the necessity of intravenous contrast injection and fat suppression.

If used as an adjunctive diagnostic technique (specifically targeting BI-RADS 4, 5, and 0), MREIM can significantly reduce the high negative biopsy rates.

Chapter 3

Electric Properties of Normal and Cancerous Breast Tissues

In biological tissues, the electric-field distribution, as well as the associated electrical currents, depends on the electrical properties of the tissues under consideration. The electrical properties of biological substances have been studied extensively since the beginning of the last century, initially at low radio-frequencies (below 100 MHz) and then at microwave frequencies up to 10 GHz.

This chapter presents the outline of micro- and macro- electric properties of breast tissue. First, an analysis of the electric properties of biological tissue is provided. It is followed by a review of electrical models for measuring the dielectric properties of human tissue with the emphasis on breast tissue. Conductivity/impedivity values measured by various authors are provided to obtain the conductivity ratio between malignant and normal breast tissue.

3.1 Microscopic Electric Properties of Biological Tissue

The matrix of cells composing biological tissues possesses electrical properties and has a capacity to conduct electric current. The major charge carriers in biological organisms are negatively charged electrons, positively charged hydrogen protons, positively charged sodium, potassium, calcium, and magnesium ions, and negatively charged anions, particularly phosphate ions. According to Charman (Charman 1996), a cell contains four electrified zones (Fig. 1). The **central zone** contains negatively charged organic molecules and maintains steady bulk negativity. An **inner positive zone** exists between the inner aspect of the cell membrane and the central negative zone. It is composed of a thin layer of freely mobile mineral cations (particularly potassium, the concentration of which is 20 times higher inside the cell than that outside) and a small amount of calcium and sodium (Nieper 1985). The **outer positive zone** exists around the outer surface of the cell membrane and consists

of a denser zone of mobile cations composed mostly of sodium (with 30-fold extracellular concentration as compared to intracellular one), calcium, and a small amount of potassium. Cell membranes are composed of a bilayer of highly mobile lipid molecules that electrically act as an insulator. Due to a selective permeability of the cell membrane to sodium and potassium ions a different concentration of these and other charged minerals will build up on each side of the membrane. Because the concentration of positive charges is larger on the outer surface of the cell membrane than the concentration of the positive charges on the inner surface of the membrane, an electrical potential exists across the cell membrane. Healthy living cells have a membrane potential of about -60 to -100 mV (Charman 1996). Separated from the positive cell membrane surface by a distance of about 20 μm, the **outermost negative zone** is composed of negatively charged sialic acid molecules that cap the tips of glycoproteins and glycolipids that extend from the cell membrane like tree branches (Charman 1996).

As a first approximation, tissue can be considered to take a form of an electrolyte containing densely packed cells. The extracellular matrix occupies an intermediate position between the blood vessels and the cell membrane and acts as a transit and storage area for nutrients, water, and waste. Anatomically, the extracellular medium consists of two subcompartments: interstitial fluid (amino acids, sugars, fatty acids, coenzymes, hormones, neurotransmitters, salts, and waste products from the cells) and blood plasma (Cure 1991). Chemically, the extracellular matrix contains cations (sodium, potassium, and calcium) and anions (chlorides and hydrogen carbonate).

Normal cells possess the ability to communicate information inside themselves and among other cells. The coordination of information by the cells of the body is involved in the regulation and integration of cellular functions and cellular growth. When cancer arises, cells are no longer regulated by the normal control mechanisms. When an injury occurs in a body, normal cells proliferate and replace the destroyed and damaged cells with new cells or scar tissue. One characteristic feature of both proliferating cells and cancer cells is that these cells have cell membrane potentials that are lower than the cell membrane potential of healthy adult cells (around -15 mV)(Cone 1974).

After the repair is completed, the normal cells in the area of an injury stop growing, and

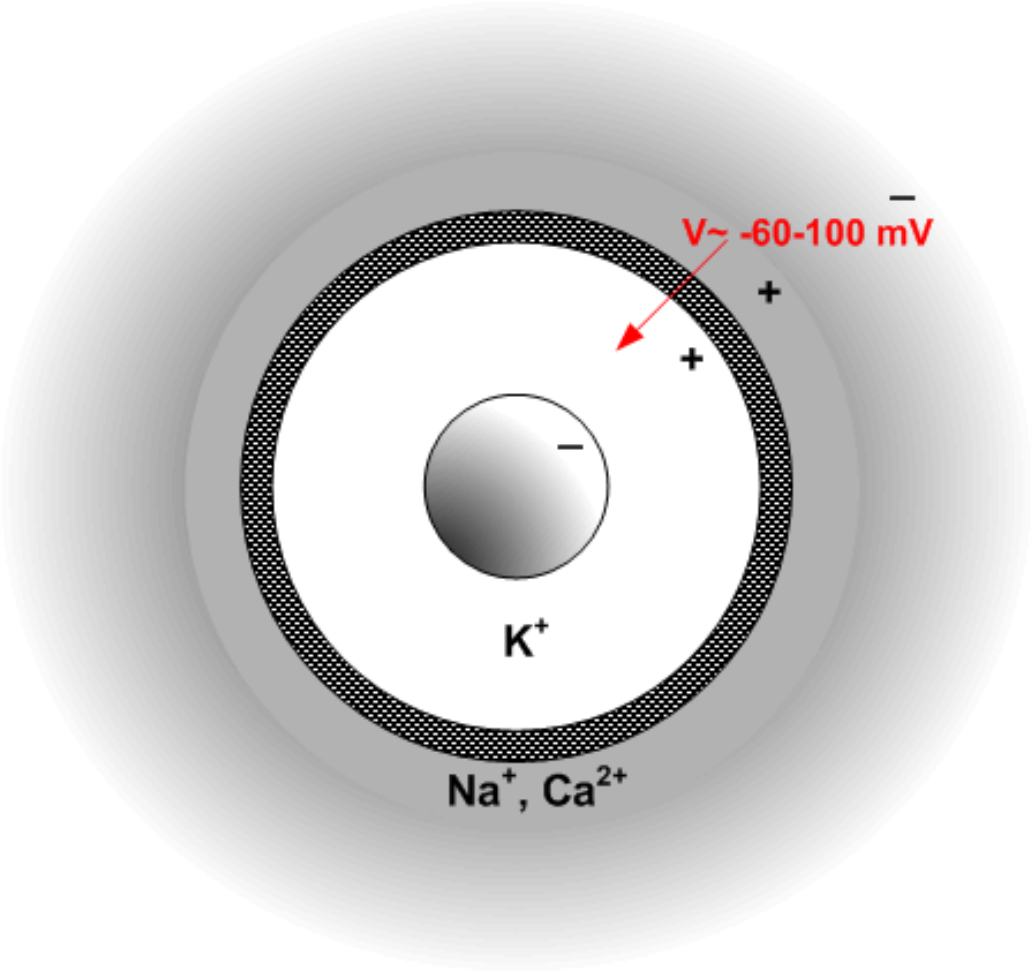

Figure 1.: Four electrical zones in healthy cell: negative central zone, inner positive zone, outer positive zone, and outermost negative zone. Due to a larger concentration of positive charges on the outer surface of the cell membrane than the concentration of the positive charges on the inner surface of the membrane an electrical potential exists across the cell membrane. Healthy living cells have a membrane potential of about -60 to -100 mV.

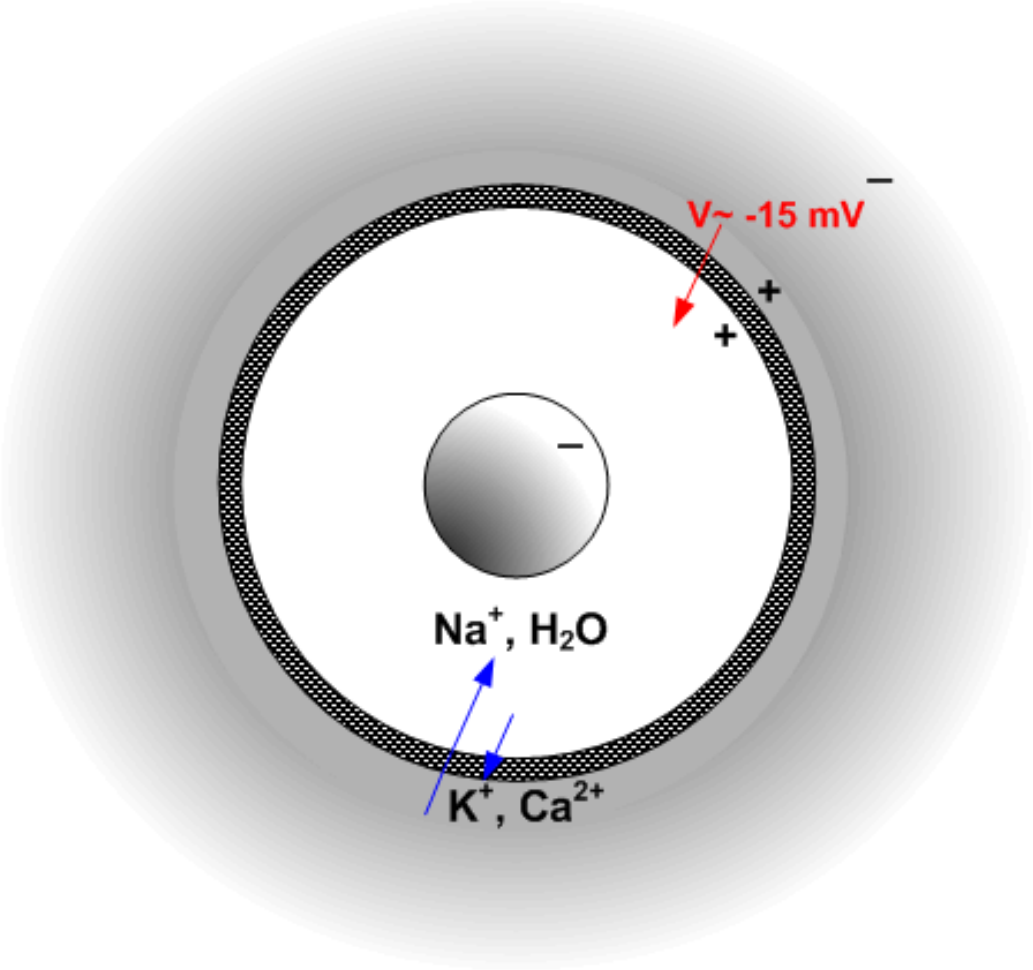

Figure 2.: Changes of electrical properties in cancerous cell: increase in intracellular sodium concentration which in turn perturbs osmotic balance and causes the inward diffusion of water, decrease in intracellular potassium and calcium concentration, increase of negative charges on cell surface. The above factors lead to a lower transmembrane potential and altered membrane permeability blocking the access of oxygen and nutrients into the cell. The latter causes the cell to rely mostly on anaerobic metabolism and promotes further division.

their membrane potential returns to normal. In cancerous tissue, the electrical potential of cell membranes is maintained at a lower level than that of healthy cells, and bonding between the cells is disrupted, making the extracellular medium more conductive. Cancer cells possess altered membrane composition and membrane permeability, which results in the movement of potassium, magnesium, and calcium out of the cell and the accumulation of sodium and water in the cell (Cone 1970; Cone 1974; Cope 1978; Seeger and Wolz 1990) (Fig. 2). Cancer cells have lower potassium concentrations and higher sodium and water content than normal cells (Cone 1970; Cone 1974; Cone 1985). A change in mineral content of the cell, particularly an increase in the intracellular concentration of positively charged sodium ions and increase in negative charges on the cell coat (glycocalyx), are two major factors causing cancerous cells to have lower membrane potentials than that of healthy cells (Cure 1991). The above changes interfere with the flow of oxygen and nutrients into a cell and impair aerobic metabolism causing a cancer cell to rely more on anaerobic metabolism for energy production. Anaerobic metabolism, excessive sodium concentrations, low transmembrane potential, and pH alterations in turn create intracellular conditions more conducive to cellular division (Cure 1991).

Figure 3 shows a scanning electron micrograph of a breast-cancer cell (from the NCI-Science Photo Library).

3.2 Macroscopic Electric Properties of Biological Tissue

A study of the relevant literature on electrical properties of biological tissue over the past 100 years reveals several interesting points. First of all, there has been an extensive cross-fertilization of ideas from various fields of science, i.e. physics, electrochemistry, electrophysiology, biomedical engineering, etc., leading to positive advancements in the area, but on the other hand, resulting in a great extent of confusion. It seems that the measurements of the tissue impedivity narrowed down to the experimental procedure only, neglecting the importance of the choice of an appropriate conduction model, its validation tests, and clear understanding of the quantities being measured.

Our need to obtain the ratio between the conductivities of malignant and normal breast tissue resulted in an extensive literature review in this area (Heine, Kovalchuk et al. 2008a),

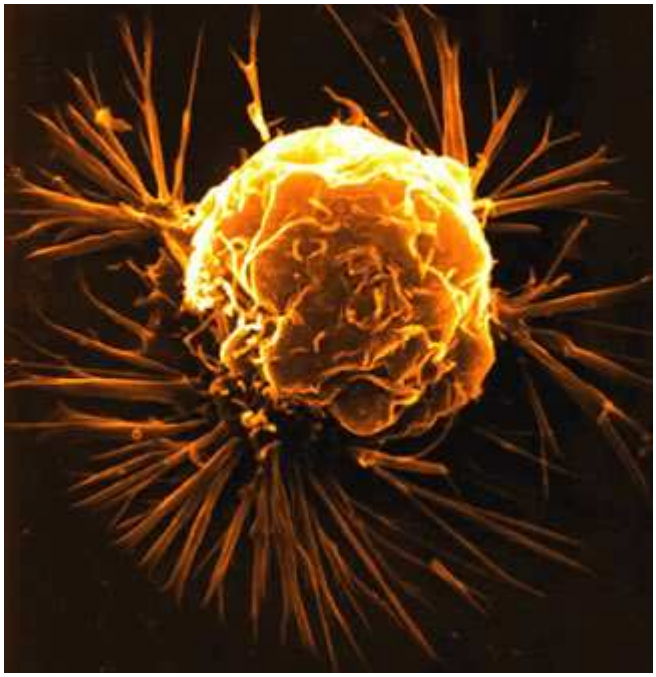

Figure 3.: Scanning electron micrograph of a breast-cancer cell, showing an abnormally uneven surface and cytoplasmic projections (from NCI-Science Photo Library/Photo Researchers).

since no single source provided a convincing outcome based on theoretical firm ground and consistency in results from various authors. The following developments parallel our previous work (Heine, Kovalchuk et al. 2008a).

3.2.1 Complex Conductivity and Permittivity

The form of complex permittivity follows from Maxwell's equation (Heine, Kovalchuk et al. 2008a)

$$\vec{\nabla} \times \vec{H} = \sigma_s \vec{E} + \varepsilon \frac{\partial \vec{E}}{\partial t}, \tag{3.1}$$

where $\vec{H}$ is the magnetic field, $\vec{E}$ is the time-varying electric field intensity oscillating with frequency ω, σ_s is static conductivity, and ε is complex permittivity. The right side of Eq. (3.1) comprises the total current density including the conduction and displacement currents and can be written as

$$\vec{i} = \sigma_s \vec{E} + \varepsilon \frac{\partial \vec{E}}{\partial t} = \sigma_s \vec{E} + j\omega\varepsilon \vec{E} = \sigma \vec{E} \tag{3.2}$$

with $j = \sqrt{-1}$. Complex conductivity can be expressed as follows:

$$\sigma = \sigma_s + j\omega\varepsilon(\omega), \tag{3.3}$$

where the complex permittivity ε is given as

$$\varepsilon = \varepsilon^{'} - j\varepsilon^{''}. \tag{3.4}$$

Here $\varepsilon^{'}$ and $-\varepsilon^{''}$ are the real and imaginary parts of the complex permittivity, respectively. Through the frequency dependence of the permittivity, the real and imaginary parts of complex conductivity, $\sigma^{'}$ and $\sigma^{''}$, are also frequency dependent. They are given by

$$\sigma^{'} = \sigma_s + \omega\varepsilon_0\varepsilon^{''} \text{and } \sigma^{''} = \omega\varepsilon_0\varepsilon', \tag{3.5}$$

where ε_0 is a permittivity of free space. Thus, the imaginary part of permittivity defines the real part of conductivity, and vice versa.

There has been much confusion in the literature over the complex conductivity nomenclature. Some researchers (Foster and Schepps 1981) include the static conductivity, σ_s, in the real part of permittivity, so the alternative form of Eq. (3.3) is presented as

$$\sigma = j\omega\varepsilon, \tag{3.6}$$

and $\vec{i} = (\sigma + j\omega\varepsilon^{'})\vec{E} = j\omega\varepsilon\vec{E}$. Both Eq. (3.3) and Eq. (3.6) are used in the literature and yield different expressions for complex permittivity. Thus, the complex permittivity from Eq. (3.6) can be written as follows:

$$\varepsilon = \varepsilon^{'} - j\varepsilon^{''} = \varepsilon^{'} - j\frac{\sigma}{\omega}. \tag{3.7}$$

Since both definitions are used in the literature, one should be careful in referring to these terms from various sources.

The chemistry literature contains many references to the dielectric constant of materials, which is meant as the real part of complex permittivity $\varepsilon^{'}$, typically, at low frequencies at which $\varepsilon^{'}$ is essentially independent of frequency (McAdams and Jossinet 1995). Also, some authors use the unit-less permittivity, regarding to it as a ratio of the permittivity to the permittivity of free space.

3.2.2 Tissue Electric Behavior with Frequency

When an electric current approaches a biological cell, it will divide into two parts: one part will bypass the cell by means of the extracellular medium (ECM), as characterized by the extracellular resistance R_e, while the other part will penetrate through the cell membrane (CM) and intracellular medium (ICM), characterized by the membrane capacitance C_m, and the intracellular resistance R_i (Fig. 5). This is a simplification since the cell membrane also has a conductance, but it is considered negligible.

Since current passes through three different media (ECM, ICM, and CM), the tissue behaves differently compared to simple RC circuits due to the distinctive response of these media to current density and frequency.

Because both conductivity and permittivity depend on frequency, this dependence should be investigated. At low frequencies (<1 kHz), the capacitive reactance of the cell membrane is large; therefore, the capacitance of the cell membrane acts as an insulating layer at low frequencies so that current flows only in the extracellular medium. With the frequency increase, the interior of cells becomes progressively involved in the conduction. From about 30 kHz to 30 MHz, the capacitive charging of the cell membrane and the dipolar relaxation of the proteins in the tissue determine the permittivity. As the frequency increases, insufficient time is available during each cycle to allow complete charging of the cell membranes. As a

result, the total charge per cycle and the membrane capacitance decrease with increase in frequency. There exists a limited frequency range in which the charging of the organelles within the cells contributes significantly to the permittivity of the tissue. At frequencies in the gigahertz range, the permittivity is due to bipolar relaxation of water.

The electric properties of biological tissues seem to follow the same dependence on frequency. As first fully described by Schwan (Schwan 1957; Schwan and Kay 1957), the relative permittivity of most tissues has a frequency-dependence pattern normally divided into three frequency domains of relaxation: α, β, and γ (Fig. 4). The α-relaxation is generally considered to be associated with extracellular surface polarization of large cells, β-relaxation is related to an increase in capacitive charging and discharging of the cell membranes, and γ-relaxation arises from the relaxation of bulk water in the tissue (Schwan 1957). For many applications, α- and β-relaxation regions are particularly interesting since most changes between normal and pathological tissues seem to appear in this frequency range. Moreover, it is more practical to design a measuring system dedicated to low frequencies.

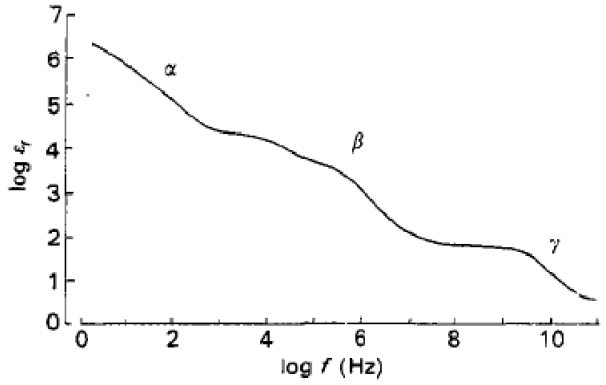

Figure 4.: An idealized plot of frequency variation of the relative permittivity for a typical biological tissue (from Schwan 1957).

3.2.3 Tissue Conduction Models

From the beginning of the 20^{th} century, there were numerous attempts to model electrical behavior of tissue. In 1925, Fricke developed a theory for the resistance of suspensions of spherical cells, modeling behavior of cells in the extracellular medium. Figure 5 shows

the electric circuit diagram used by Fricke and Morse (Fricke and Morse 1926) as a tissue model. This simplified tissue model was later used by Morimoto et al., and Chauveau et al. (Morimoto, Kinouchi et al. 1990; Morimoto, Kimura et al. 1993; Chauveau, Hamzaoui et al. 1999; Ohmine, Morimoto et al. 2000). In this diagram, R_e represents the extracellular resistance, R_i is an intracellular resistance, and C_m is a membrane capacitance. Although Fricke showed that his model, incorporating a pure frequency-independent capacitance, was satisfactory in representing the electrical properties of suspensions of red blood cells, other tissues showed a more complex behavior. In simple RC circuits, the permittivity is usually considered independent of frequency. Tissues exhibit a frequency-dependent behavior beyond the simple RC circuits. This is because the different components (ECM, ICM, and CM) contribute differently to the impedance.

Cole (Cole 1928) in his early work in 1928 developed the tissue equivalent circuit approach, finding the impedance of a fundamental cell, and then expanded the work to a suspension of homogenous spheres that modeled the bulk tissue. The novelty of Cole's study was that it incorporated a "constant phase (CP) impedance element" in the circuit diagram. He also showed that any network containing any combination of resistances and single variable impedance with a constant phase angle independent of frequency produces reactance versus resistance plots in the form of an arc of a circle with a center displaced along both axes ("depressed circle").

The phase angle between the resistance and reactance (Fig. 6) can be found as $\theta = \tan^{-1}(X/R)$, which is constant in the CP element and results in a linear relationship between the two, $R = mX$, where m is a constant. Note that the CP element does not contain the explicit form of reactance X and becomes a perfect conductor in the high-frequency limit.

The Cole-Cole paper in 1941 (Cole and Cole 1941) provided a major turning point in the research history of the electrical properties of tissues and membranes. The dispersion and absorption of many liquids and dielectrics were found to follow this empirical expression:

$$\varepsilon - \varepsilon_\infty = \frac{\varepsilon_0 - \varepsilon_\infty}{1 + (j\omega\tau)^{1-\alpha}}. \tag{3.8}$$

In this equation, ε is a complex dielectric constant, and ε_0 and ε_∞ are the dielectric constants in the low- and high-frequency limits, respectively, τ is a general relaxation time, and α is a

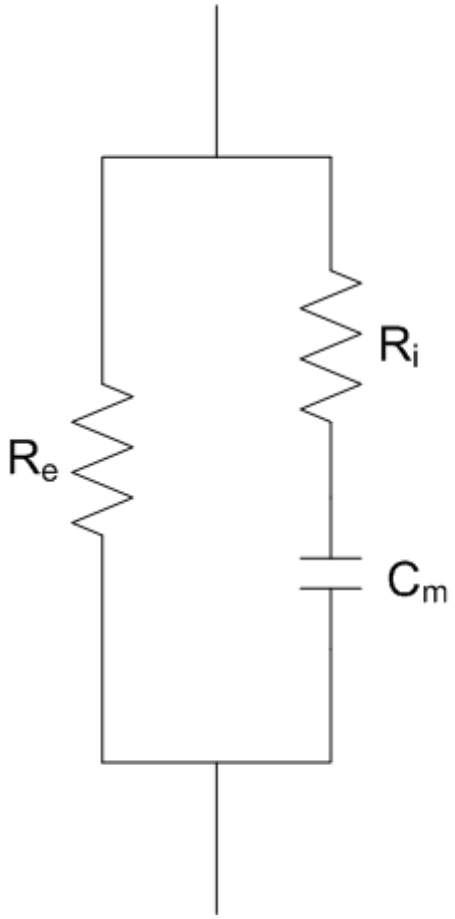

Figure 5.: A simplified equivalent electrical circuit corresponding to the electrical behavior of tissues (used by Morimoto, Kinouchi et al. 1990; Morimoto, Kimura et al. 1993; Chauveau, Hamzaoui et al. 1999; Ohmine, Morimoto et al. 2000).

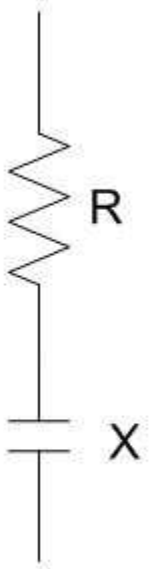

Figure 6.: A part of the electric circuit with resistance R and reactance X.

parameter changing between 0 and 1. Eq. (3.8) was modified based on the classical theory of the effect for polar liquids by Debye, where $\alpha = 0$.

Only in this special case, at $\alpha = 0$, Eq. (3.8) can be used to obtain the relation between ε and σ. Adding the static conduction term to Eq. (3.8) by using the definition of the complex conductivity in form of Eq. (3.6), we have the following

$$\varepsilon - \varepsilon_\infty = \frac{\varepsilon_0 - \varepsilon_\infty}{1 + (j\omega\tau)^{1-\alpha}} - \frac{j\sigma_s}{\omega}. \tag{3.9}$$

With $\alpha = 0$, after separation of Eq. (3.9) into real and imaginary components, multiplying the imaginary component by $j\omega$, we can find the limit of the obtained expression for $\omega \to \infty$:

$$j\omega\varepsilon'' = \lim_{\omega\to\infty}\left[\frac{\omega^2\tau(\varepsilon_0 - \varepsilon_\infty)}{1 + (\omega\tau)^2} + \sigma_s\right] = \sigma_\infty. \tag{3.10}$$

Equation (3.10) gives the following relationship between the permittivity and conductivity exclusively when $\alpha = 0$:

$$\sigma_\infty - \sigma_s = \frac{(\varepsilon_0 - \varepsilon_\infty)}{\tau}. \tag{3.11}$$

In spite of the fact that Eq. (3.11) holds only in the Debye form of Eq. (3.9), i.e. $\alpha = 0$ (otherwise the upper limit does not exist), some researchers generalized it for $\alpha \neq 0$ (Jossinett and Schmitt 1999).

When plotted on the Nyquist diagram (Fig. 7), Eq. (3.8) represents the arc of a circle with the center displaced along both axes, and the depression of an arc is represented by angle $\alpha\pi/2$.

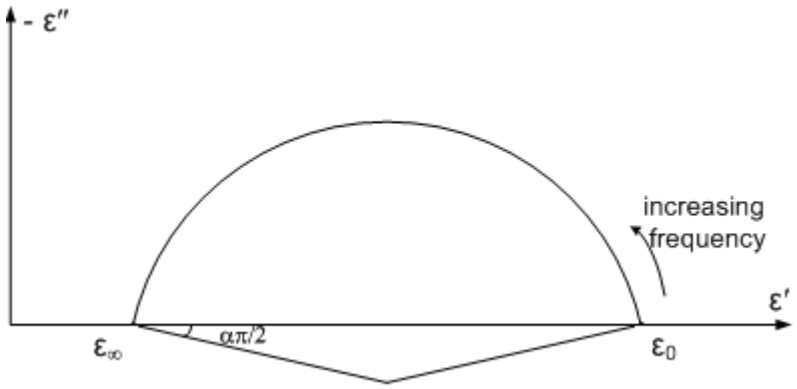

Figure 7.: Complex plane plot of Eq. (3.8) representing the "depressed circle" with the depression determined by angle $\alpha\pi/2$. Here, $\varepsilon^{'}$and $\varepsilon^{''}$ are the real and imaginary parts of dielectric constant, respectively, and ε_0 and ε_∞ are the dielectric constants in the low- and high-frequency limits, correspondingly.

Some sources assume that the quantities such as permittivity and conductivity for the same circuit may be represented by the depressed circles simultaneously (Jossinet 1996; Jossinet 1998; Jossinet and Schmitt 1999). To prove the opposite, we will refer to the original work by Cole-Cole (Cole and Cole 1941). Figure 8 shows the electric circuit diagram used by Cole (Cole and Cole 1941) to model the dispersion and absorption of many fluids and dielectrics. We will show that the following circuit results in the empirical Eq. (3.8).

Since the impedivity of the left leg is $\frac{1}{\varepsilon_\infty j\omega}$ and impedivity of the right leg is $\frac{1}{(\varepsilon_0-\varepsilon_\infty)j\omega} + \frac{\tau(j\omega\tau)^{-\alpha}}{\varepsilon_0-\varepsilon_\infty}$, the total impedivity for a circuit is

$$z = \frac{\tau}{j\omega\tau}\frac{\left[1+(j\omega\tau)^{1-\alpha}\right]}{\varepsilon_0+\varepsilon_\infty(j\omega\tau)^{1-\alpha}}. \tag{3.12}$$

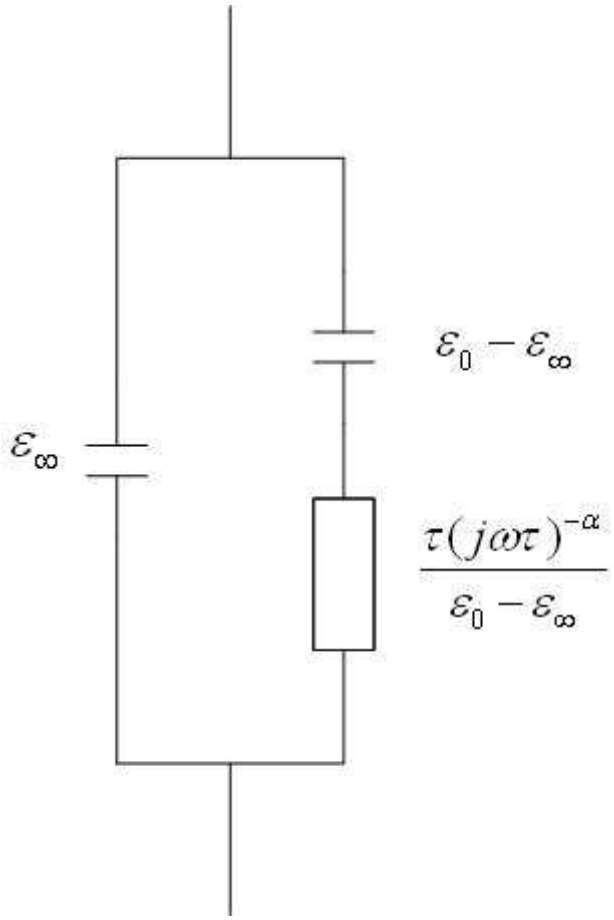

Figure 8.: Electrical circuit developed by Cole-Cole (Cole and Cole 1941) as a model for the dispersion and absorption of many liquids and dielectrics, which is represented by empirical Eq. (3.8). This circuit is modified from the Debye classical theory of the effect for polar liquids by changing the resistance in the right leg with the constant phase element.

The conductivity then can be obtained inverting Eq. (3.12)

$$\sigma = j\omega \left[\frac{\varepsilon_0 + \varepsilon_\infty (j\omega\tau)^{1-\alpha}}{1 + (j\omega\tau)^{1-\alpha}} \right]. \tag{3.13}$$

Comparing Eq. (3.13) with Eq. (3.6) we can write the term in brackets as permittivity

$$\varepsilon = \frac{\varepsilon_0 + \varepsilon_\infty (j\omega\tau)^{1-\alpha}}{1 + (j\omega\tau)^{1-\alpha}} = \varepsilon_\infty + \frac{\varepsilon_0 - \varepsilon_\infty}{1 + (j\omega\tau)^{1-\alpha}}, \tag{3.14}$$

which is equivalent to Eq. (3.8). As mentioned previously, Eq. (3.14) represents the depressed circle on the Nyquist plot diagram as shown in Fig. 9. On the same hand, the corresponding conductivity, derived from the same circuit, does not represent the depressed circle as shown in Fig. 10, which contradicts the statement of some researchers (Jossinett and Schmitt 1999).

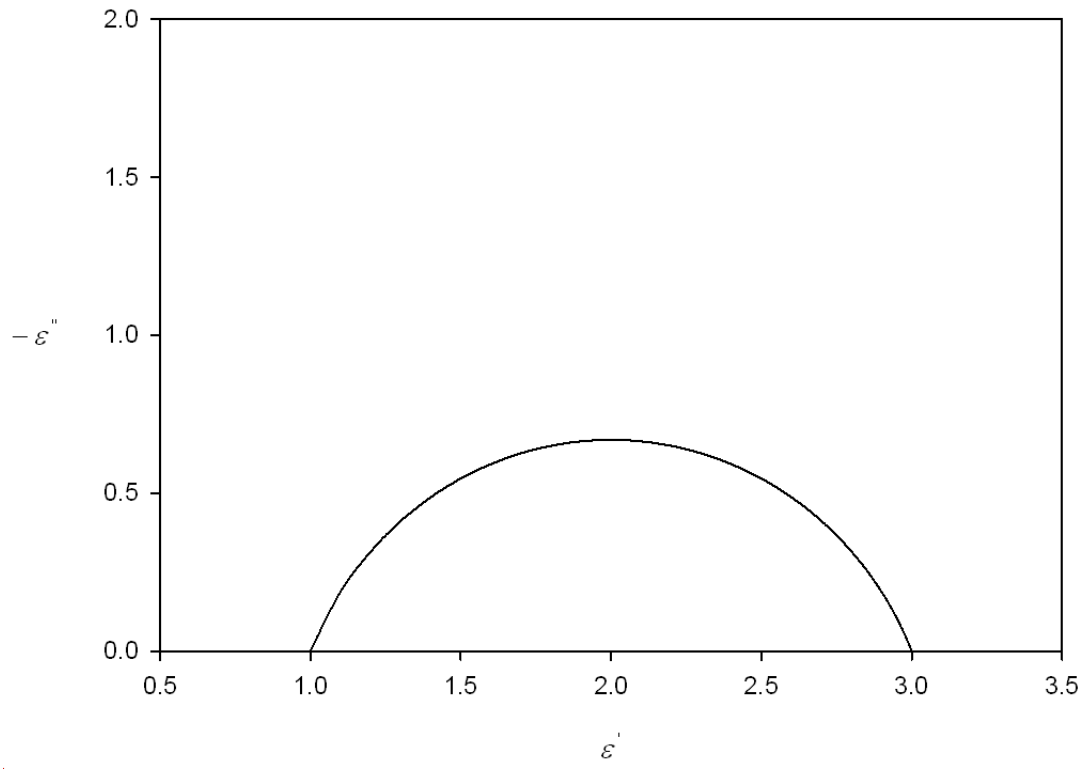

Figure 9.: A graphical representation of Eq. (3.14), where $\varepsilon_0 = 1$ F/m, $\varepsilon_\infty = 3$ F/m, and $\alpha = 0.25$.

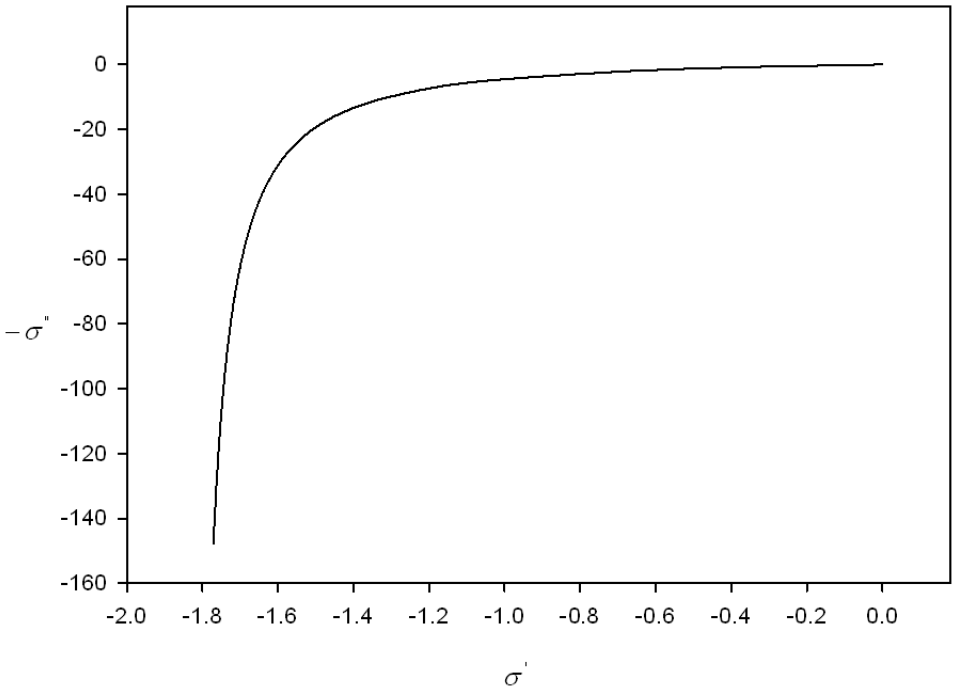

Figure 10.: A graphical representation of Eq. (3.13), where $\varepsilon_0 = 1$ F/m, $\varepsilon_\infty = 3$ F/m, and $\alpha = 0.25$.

To find an accurate model representing the behavior of biological tissues, we refer to the work by Cole, Chauveau, and McAdams (Cole 1932; Chauveau, Hamzaoui et al. 1999, McAdams and Jossinett 1995). Figure 11 shows the modified circuit from Fig. 5 with the capacitance replaced by the CP element.

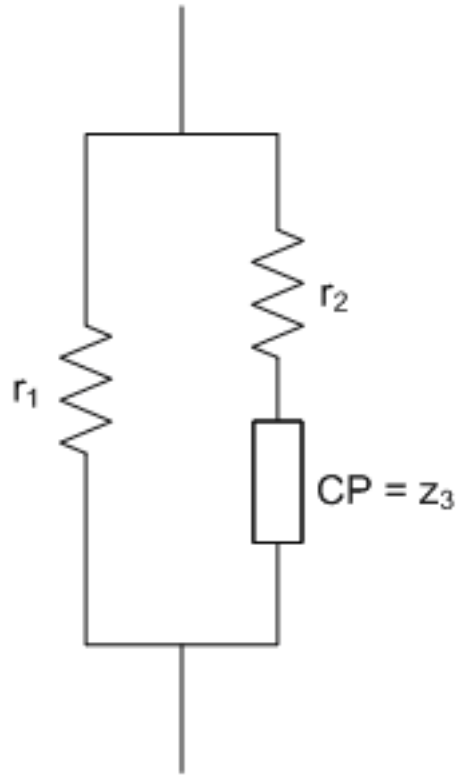

Figure 11.: The tissue equivalent circuit diagram incorporating the constant phase element. Here r_1 is an extracellular resistivity, r_2 is an intercellular resistivity, and CP is a constant phase element with the impedivity z_3.

The total impedance of the circuit is given as

$$z = \frac{r_1(r_2 + z_3)}{r_1 + r_2 + r_3}, \tag{3.15}$$

where $z_3 = r_3 + jx_3$ represents the constant phase element, and $r_3 = mx_3$, where m is a constant, and x_3 is not defined explicitly. Letting $z = r + jx$ and $t = r_1 + r_2$, separating Eq. (3.15) into real and imaginary parts will result in

$$rt - r_1 r_2 = (mr_1 - mr + x)\, x_3 \tag{3.16}$$

and

$$tx = (r_1 - mx - r)\, x_3. \tag{3.17}$$

Solving this system of equations will give

$$tx^2 + tr^2 + mr_1tx - mr_1r_2x - r_1tr - r_1r_2r = -r_1^2r_2. \tag{3.18}$$

At low frequency limit, the impedivity of the circuit will be due to the resistivity of the left leg (extracellular resistivity); thus

$$r_0 = r_1. \tag{3.19}$$

At high frequency limit, the impedivity is also real and equal to

$$r_\infty = \frac{r_1 r_2}{r_1 + r_2}. \tag{3.20}$$

It should be noted that $r_\infty < r_0$.

Dividing Eq. (3.18) by t and applying Eqs. (3.19)–(3.20) gives the equation for a circle

$$x^2 + r^2 + m(r_0 - r_\infty)x - (r_0 + r_\infty)r = -r_0 r_\infty \tag{3.21}$$

with a center located at

$$(r_c; x_c) = \left(\frac{[r_0 + r_\infty]}{2}; -m\frac{[r_0 - r_\infty]}{2} \right) \tag{3.22}$$

and radius given by

$$Radius = \frac{1}{2}\left[m^2 + 1\right]^{\frac{1}{2}} (r_0 - r_\infty)\,. \tag{3.23}$$

The Nyquist plot of Eq. (3.21) is presented in Fig. 12.

The next step forward is to compare the theoretical parameters from Fig. 12 with the experimental values. A number of measurements were performed at various frequency ranges. The next section will elaborate on some of them, concentrating on the electrical properties of normal and malignant breast tissue.

3.2.4 Electric Properties of Breast Cancer

From as early as 1926, researchers have been studying the electrical properties of breast tumors. Having investigated 58 breast tumor cases, Fricke and Morse stated that "certain types of malignant tumors have a rather high capacitance in comparison with benign

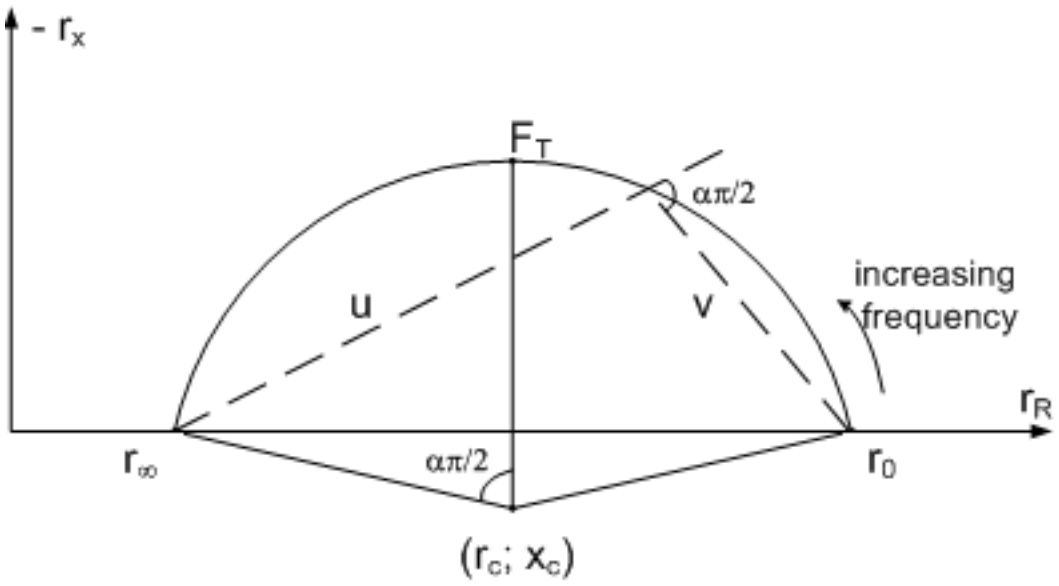

Figure 12.: Reactance r_x versus resistance r_R plot ("depressed circle") typical for biological tissue. Here the negative sign of the reactance axis is taken as a convention. The important parameters are labeled as follows: r_∞ and r_0 represent the high- and low-frequency limit resistances, respectively; $(r_c; x_c)$ are the coordinates of the displaced center of a circle; the depression of an arc is represented by angle $\alpha\pi/2$; vectors $\vec{u}$ and $\vec{v}$ are used to derive the above angle.

tumors." For a biological tissue model the authors considered a parallel combination of pure resistance and pure capacitance. Measurements of the resistance and capacitance of breast tissue placed in the conductivity cell were made on a Wheatstone bridge of a special design at 20 kHz and resulted in a consistently larger capacitance of malignant tumors in comparison with that of benign tumors or normal tissue.

In 1988, Surowiec at al. (Surowiec, Stuchly et al. 1988) performed in-vitro tests on tumor specimens from 7 different patients completed within 4 hours after the surgery. The relative permittivity of infiltrating breast carcinoma and the surrounding tissue was measured at frequencies from 20 kHz to 100 MHz using an automatic network analyzer and an end-of-the-line capacitive sensor. It should be noted that in order to minimize the electrode polarization effect below 100 kHz, a substitution technique developed by Schwan (Schwan 1963) was used. According to this technique, the tissue was replaced by a saline solution of the same conductivity, and its dielectric properties were determined at low frequencies. Three main categories of tissues were considered in this study: the central part of the tumor, the tumor surrounding tissue, and the peripheral tissue. Figure 13 shows one of the specimens with the selected cylindrical regions corresponding to the measured samples.

The first type of tissue represented the bulk of a tumor (e.g., Fig. 13, sample E2) and consisted of collagen, elastic fibers, and tumor cells. These samples had low-frequency conductivities between 2 and 4 mS/cm with dielectric constants ranging from 2×10^3 to 6×10^3.

The second type of samples was taken from the infiltrating margins of the tumor near the edge of the lesion (e.g., Fig. 13, sample E4), where fewer tumor cells and a larger portion of normally distributed collagen and fat from the surrounding unaffected breast tissue were present. The dielectric constants ranged from 2.5×10^3 to 8×10^3 at 100 kHz.

The third type of samples was taken from the periphery distant from the tumor by approximately 2 cm (e.g., Fig. 13, sample E1). This tissue is composed of connective and glandular tissue. The dielectric properties of the third type of tissue differed significantly from the other two types. The conductivities of normal tissue were less than 1 mS/cm with dielectric constant less than 500 at 100 kHz.

As a summary of the dielectric properties measurements, Surowiec et al. (Surowiec,

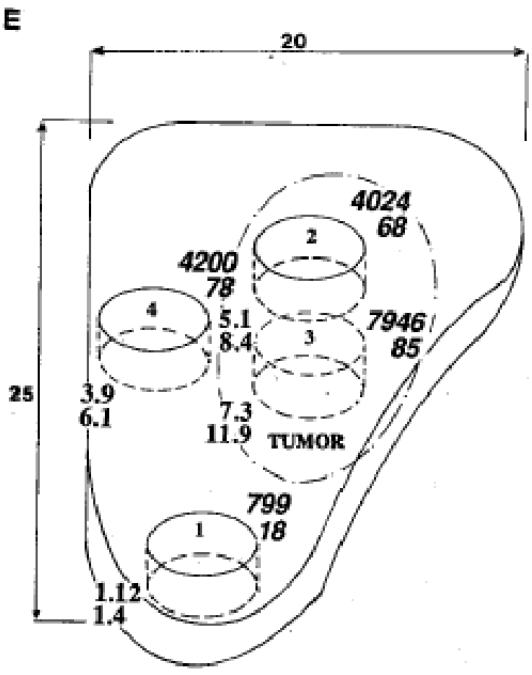

Figure 13.: Location of the tissue samples excised from a specimen of infiltrating lobular carcinoma (specimen E). Dash-dot lines describe the visible boundary of the tumor tissue. The two numbers indicate the upper-right corner the dielectric constants at 100 kHz and 100 MHz, respectively, the lower-left corner conductivities at the same frequencies (from Surowiec, Stuchly et al. 1988).

Stuchly et al. 1988) presented a plot of conductivity dependence on frequency for certain samples of breast carcinoma (Fig. 14).

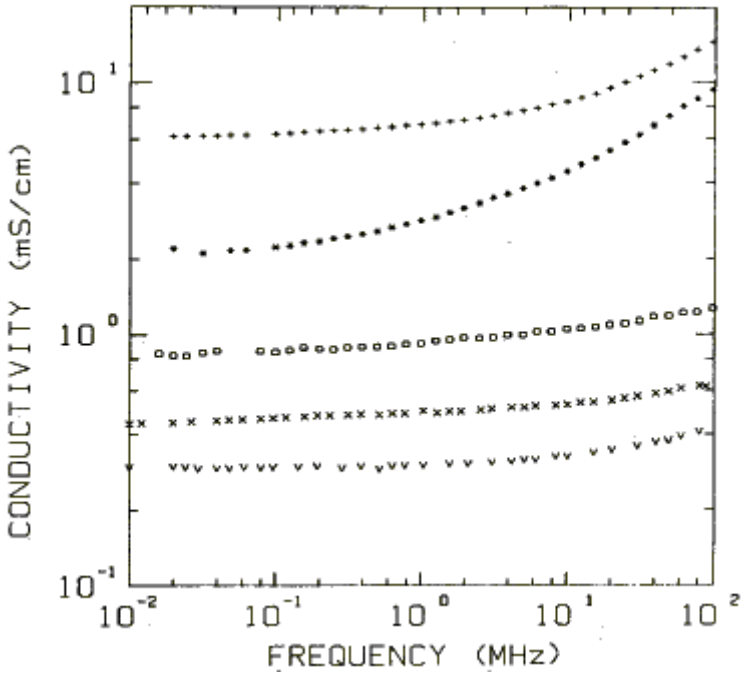

Figure 14.: Conductivity of breast carcinoma as a function of frequency (adapted from Surowiec, Stuchly et al. 1988). (+) Tissue surrounding the tumor, (∗) central part of tumor, (∘) fatty tissue containing infiltrating tumor cells, (×) peripheral tissue, and (∨) normal breast tissue. Note: in the original paper, the captions on the plots of conductivity versus frequency and dielectric constant versus frequency are reversed.

From the plot above (Fig. 14), the conductivities of the central part of the tumor and tissue surrounding the tumor at 10 kHz range from 2 mS/cm to 6 mS/cm. The conductivity of normal tissue is 0.3 mS/cm. Then the ratios of conductivities for cancerous and normal tissue will be in a range from 6 to 20 at $f = 10$ kHz.

Since the measurements were conducted at a significantly higher frequency region than that of our present study (200–300 Hz), and Schwan's substitution algorithm was used for dielectric properties measurements at frequencies below 100 kHz, the results of Surowiec et al. (Surowiec, Stuchly et al. 1988) study should be considered carefully in terms of our work.

Comparatively little work has been reported for the dielectric properties of breast tissue in the frequency range up to a few kHz. But a good example of α-dispersion was obtained by Singh et al. (Singh, Smith et al. 1979) for in-vivo measurements using external electrodes for normal breasts and breasts with malignant tumors. Some of these results are shown in Fig. 15.

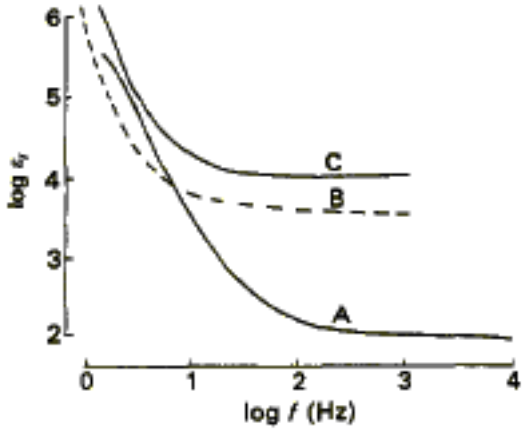

Figure 15.: Values of the relative permittivity for: (A) human kidney, (B) normal breast, and (C) breast with malignant tumor (from Singh, Smith et al. 1979).

From Fig. 15, the relative permittivity of breast with malignant tumor is around 10^4, and for normal breast tissue approximately 3500, making the ratio between the relative permittivities for malignant and normal tissue 2.5.

An in-vivo measurement of dielectric properties of breast tissues was conducted by Morimoto et al. (Morimoto, Kinouchi et al. 1990). The authors used a three-electrode measuring system consisting of a coaxial needle electrode inserted into the tumor (right before a biopsy was performed) and a large reference electrode placed on the upper abdominal wall. The electrical impedance was measured in 54 patients with breast tumors. The tissue-equivalent model consisted of the extracellular resistance, R_e, in parallel with a series combination of the intracellular resistance, R_i, and capacitance of cell membrane, C_m (Fig. 5). These three parameters were calculated on the basis of a bio-equivalent circuit by means of curve-fitting technique (Ackmann and Seitz 1984). Morimoto et al. made an assumption that the impedance-spectrum trajectory follows a semicircle having its center at the real axis

with the real-axis intercepts at points R_e and $R_e \cdot R_i / (R_e + R_i)$ (Morimoto, Kinouchi et al. 1990). Then, these three parameters were compared between the fatty tissue, normal tissue, fibroadenoma, and breast cancer. Worthy of notice is the definition of "normal breast tissue" by Morimoto et al. (Morimoto, Kinouchi et al. 1990; Morimoto, Kimura et al. 1993):

> "the data of 'normal breast tissue' comprised the values of mastopathy and mammary tissue around the tumor."

The authors stated the values for three components, R_e, R_i, and C_m, at the single frequency of $f = 10$ kHz (see Table 2).

Table 2: Dielectric properties of breast tissue at $f = 10$ kHz (measured by Morimoto, Kinouchi et al. 1990). "Normal tissue" is defined as mastopathy and mammary.

Tissue Type	Total Impedance Impedance, Z, Ω	Extracellular Resistance, R_e, Ω	Intracellular Resistance, R_i, Ω	Membrane Capacitance, C_m, pF
Breast cancer	1,271 ± 508	1,445 ± 586	2,493 ± 1,490	3,525 ± 1,879
Fibroadenoma	806 ± 144	954 ± 156	1,179 ± 446	6,171 ± 2,365
"Normal tissue"	674 ± 157	772 ± 203	1,955 ± 1,414	5,946 ± 3,194
Fatty tissue	5,668 ± 3,166	6,044 ± 3,388	8,622 ± 4,210	554 ± 262

According to the authors, "the values of R_e and R_i in breast cancer were significantly higher than those in benign tumor, and the value of C_m in breast cancer was significantly smaller than that of fibroadenoma." This statement contradicts the conclusion reached by most researchers that the resistance of breast cancer is much lower than that of normal tissue. A possible argument here might lie in the definition of normal breast tissue, and one should compare the cancerous-tissue parameters with those for fatty tissue. According to Jossinet (Jossinet 1998), whose work will be considered next, "the low-frequency-limit resistance of carcinoma was found to be larger than that of all other groups (i.e., mammary gland, mastopathy, and fibroadenoma), fatty groups, connective tissue and adipose tissue excepted."

Jossinet et al. (Jossinet 1996; Jossinet 1998; Jossinet and Schmitt 1999) studied impedance of six groups of breast tissue (mammary gland, connective tissue, adipose subcutaneous fatty tissue, mastopathy, fibro-adenoma, and carcinoma) at twelve frequencies over a frequency range from 488 Hz to 1 MHz. One hundred and twenty spectra were collected in excised tissue samples from 64 patients within 10 minutes of excision. Measurements were made using a hand-held probe, ensuring a constant geometry factor, and a micro-computer-controlled impedance-spectroscopy system. All three articles (Jossinet 1996; Jossinet 1998; Jossinet and Schmitt 1999) present studies using the same data.

In his first article (Jossinet 1996), Jossinet investigated the variability of impedivity in breast tissue by assessing the standard deviation and the reduced standard error. The mean and standard deviation values of the magnitude of impedivity in the six groups of tissue are shown in Table 3. It was concluded that below 10 kHz, the variability was attributed to the dispersion of measurement errors in conjunction with the dispersion of the size of the examined tissue samples.

Table 3: Mean and standard deviation of the magnitude of impedivity in six groups of tissue at $f = 0.488$ kHz (measured by Jossinet 1996).

Tissue Type	Magnitude of Impedivity at f = 0.488 kHz, Ω·cm
Mammary gland	246 ± 147
Connective tissue	1109 ± 371
Adipose tissue	2188 ± 338
Carcinoma	373 ± 97
Fibroadenoma	245 ± 70
Mastopathy	284 ± 110

In the second study by Jossinet (Jossinet 1998), the objective was to distinguish malignant and benign tissues using the Cole-Cole parameters. The Cole-Cole parameters, ρ_0, ρ_∞, etc., were found by fitting the plots of reactivity versus resistivity to the circular arcs. It

appeared that "in certain cases the plots formed quasilinear arcs with a very small curvature (essentially for mammary gland and fibro-adenoma), and the frequency responses of certain samples formed "composite loci" comprising two relaxation domains, presumably due to the compound structure of the tissue" (Jossinet 1998) (Fig. 16).

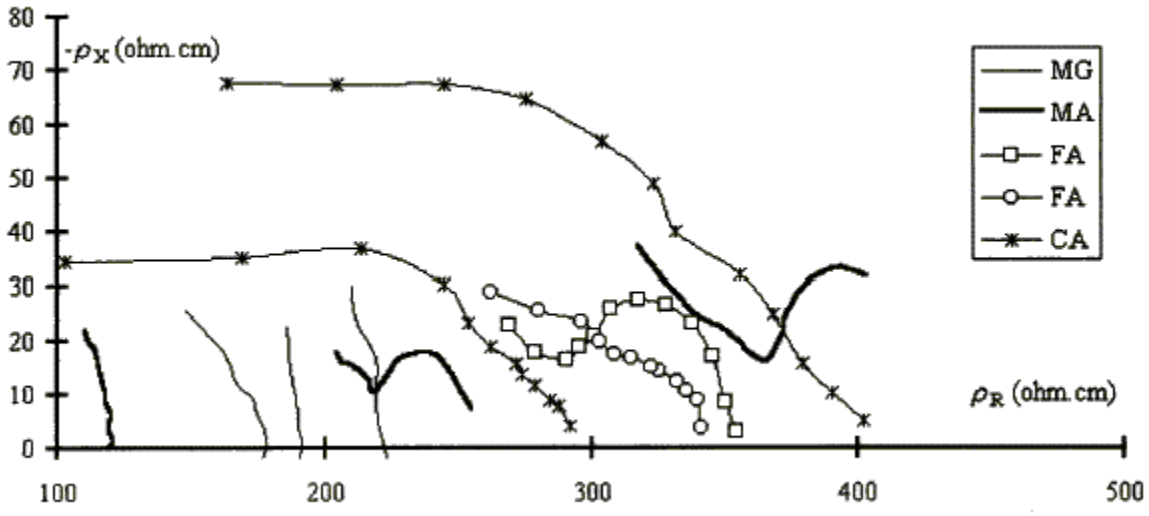

Figure 16.: Typical impedivity loci in the complex plane of non-fatty breast tissues (from Jossinet, 1998)(Jossinet 1998). Types of tissue: MG — mammary gland, MA — mastopathy, FA — fibroadenoma, and CA — carcinoma.

The analysis of experimental data showed the absence of any significant difference in impedivity, low-frequency limit resistivity, ρ_0, and fractional power, α, between normal and benign breast tissues (Table 3). The low-frequency-limit resistance of connective and adipose tissue was found to be larger than that of carcinoma.

Jossinet and Schmitt attempted in the third study to define and evaluate a set of parameters designed to characterize and differentiate breast tissues. Tissue frequency response was described as

$$\sigma^* \approx \sigma_\infty + \frac{\sigma_0 - \sigma_\infty}{1 + (j\omega\tau)^\alpha} \tag{3.24}$$

and represented on a complex plane as a circular arc (Fig 17).

Eight parameters were considered:

- low-frequency-limit admittivity, σ_0;

Table 4: Average values of low-frequency-limit resistivity for six types of tissue (calculated by Jossinet 1998).

Tissue Type	Low-Frequency-Limit Resistivity, ρ_0, (Ω·cm)	Ratio of Resistivities of Given Tissue and Carcinoma
Mammary gland	251 ± 148	0.65
Connective tissue	1263 ± 387	3.25
Adipose tissue	2390 ± 386	6.14
Carcinoma	389 ± 108	1
Fibroadenoma	254 ± 66	0.65
Mastopathy	292 ± 114	0.75

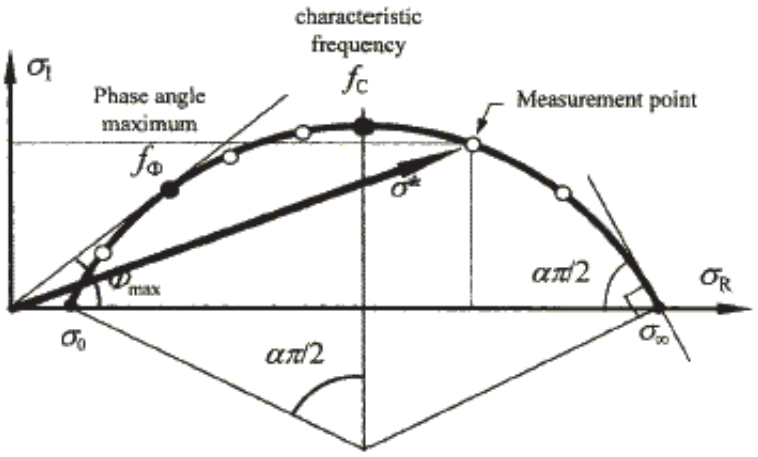

Figure 17.: Geometrical properties of conductivity arcs (from Jossinet and Schmitt 1999).

- fractional power, α;

- parameter Q_{LH}, ${}^{\sigma_0}/_{\sigma_\infty}$;

- parameter D_A, distance to the low-frequency intercept;

- parameter Φ_{500}, magnitude of phase angle at 500 Hz;

- parameter S_{HF}, high-frequency slope in phase angle;

- parameter K_Φ, integrated phase ratio.

It was concluded that none of the parameters alone was sufficient for the discrimination of any one individual group of tissue; thus, several parameters were needed for the classification of spectra. But the results of the statistical analysis of the parameter sets showed significant differences between most of the tissue groups, especially between cancerous tissue and other groups. Based on the erroneous interpretation of the Cole-Cole empirical formula (Eq. (3.8)), the measurement results from Jossinet's work should be considered with care. Taking into account the inverse relationship between conductivity and resistivity, the experimental impedivity plots by Jossinet (Fig. 16) resemble the theoretically obtained plot of Eq. (3.13) presented in Fig. 10.

Chauveau at al. (Chauveau, Hamzaoui et al. 1999) investigated ex-vivo samples of normal and pathological breast tissues at frequencies from 10 kHz to 10 MHz in the first 30 minutes following the excision. The $R-S-Z_{cpe}$ model which resembles our model shown on Fig. 11 was applied (Fig. 18).

The constant phase element was defined as: $Z_{cpe} = {}^{1}/_{(C_\delta \times \omega)^\delta}$ (Macdonald 1987), where C_δ is a pseudo-capacitance, and $\delta = 1 - \alpha$.

Breast tissue was classified into four types:

- I - normal breast tissue;

- II - Invasive Ductal Carcinoma;

- III- Invasive Ductal Carcinoma with strong stromal reaction;

- IV - fibrocystic changes.

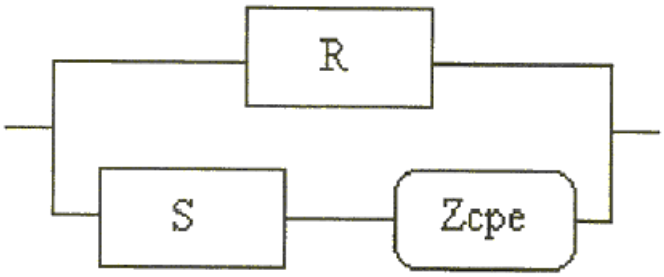

Figure 18.: $R - S - Z_{cpe}$ model (from Chauveau, Hamzaoui et al. 1999). R – extracellular resistance, S – intracellular resistance, and Z_{cpe}- membrane behavior constant phase element.

Table 5: $R - S - Z_{cpe}$ Parameters measured at f =(10 kHz–10 MHz)(from Chauveau, Hamzaoui et al. 1999). Groups II and III correspond to cancerous tissues. Only normal tissues presented intracellular resistance $S = 0$ and had lower real capacitance $C_{\delta=1}$.

Category	R, Ω	S, Ω	C_δ, $\times 10^{-13}$ F	δ	$C_{\delta-1}$, $\times 10^{-13}$ F
I	114	0	2	0.5496	1
I	114	0	2	0.5496	1
I	158	0	110	0.8797	2
II	95.9	109	114	0.555	80
II	78	66.2	32	0.4904	56
II	71.3	70.3	75	0.5188	74
III	124	41.9	45	0.4733	133
III	115	45.2	250	0.5148	299
IV	33	160	18	0.4925	40
IV	28	128	17	0.5517	10

Three ratio indices were proposed to characterize the same tissue categories:

- Index S/R
- Index $K_1 = Z'_{1MHz}/Z'_{10kHz}$ on the real part
- Index $K_2 = Z''_{1MHz}/Z''_{10kHz}$ on the imaginary part.

Basing on the indices above a two-category classification was made:

- Cancerous tissue: $0.2 < S/R < 2$ or $K_1 < 0.85$
- "Nonpathological" tissue: $S/R < 0.2$ or $K_1 > 0.85$

These differentiation parameters might not be very applicable to imaging techniques since they are based on ratios between parameters measured at different frequency ranges.

Scholz and Anderson (Scholz and Anderson 2000) in their study of Electrical Impedance Scanning, simulated the performance of the Electrical Impedance Scanner and compared the simulation results with the experimental data from the TransScan TS2000. They employed the in-vitro studies of breast tissue dielectric properties in the frequency region of 488 Hz to 1 MHz carried out by Jossinet (Jossinet 1998). The Cole-Cole parameters (Foster and Schwan 1989; Stuchly and Stuchly 1990; Morucci, Valentinuzzi et al. 1996) derived from these measurements were used to extrapolate the conductivity plots into frequency region of $1 - 10^8$ Hz (Fig 19).

The values of σ' and σ'' at $f = 200$ Hz extracted from their plots are shown in Table 6. At $f = 200$ Hz, the real part of carcinoma conductivity is 3 times higher than that of the 50/50 mix of adipose and connective tissues.

To summarize this review, cancerous tissue can be distinguished from the healthy breast tissue by its electric properties, specifically electrical conductivity, or its inverse, impedivity. The quantitative differentiation of breast tissue electric properties provides a broad range of values varying from study to study which might be due to a number of reasons: use of different theoretical models for biological tissue simulation, erroneous usage of experimental parameters as regarded to the supporting theory, experimental errors (e.g., low-frequency dielectric measurement errors due to polarization, etc.), different tissue classification (e.g.,

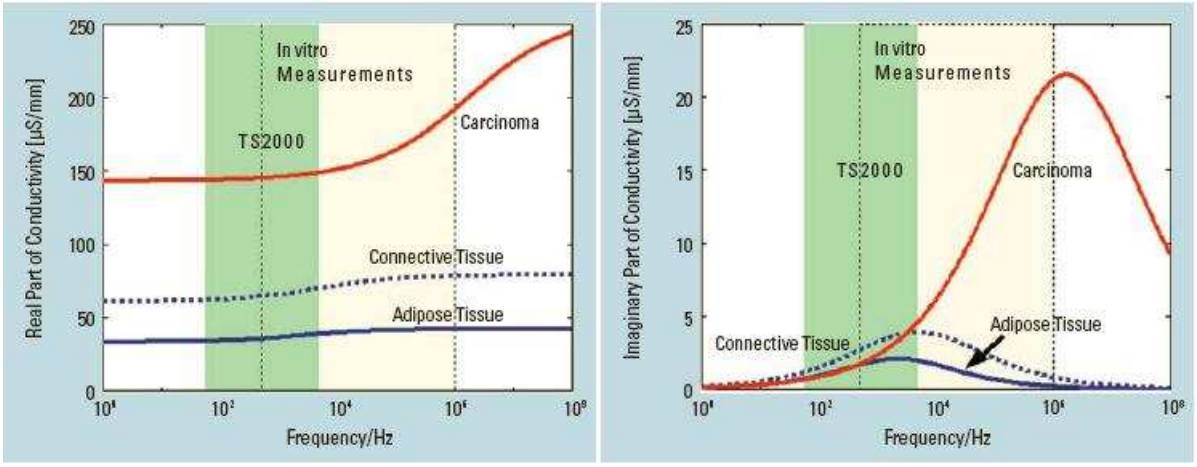

Figure 19.: Real and imaginary parts of conductivity for various types of breast tissue (calculated using parameters from Jossinet 1998). The frequency range limited by dashed lines is the range of the in-vitro measurements. The green area marks the frequency range currently accessible by the TransScan TS2000 system (from Scholz and Anderson 2000).

Table 6: Real and imaginary parts of conductivity at f= 200 Hz (extracted from Scholz and Anderson 2000)(Fig. 19).

Tissue Type	$\sigma^{'}$	$\sigma^{''}$
	μS/mm	μS/mm
Carcinoma	145	1
Connective tissue	60	2
Adipose tissue	35	1

by Morimoto (Morimoto, Kinouchi et al. 1990), or compound tissue samples. In addition, it is also shown that cycling hormones might affect the measured impedance of both healthy and malignant tissues (Perlet, Kessler et al. 2000). It has been also proven that there is a significant difference between impedance of normal living tissue and that of dead tissue. The impedance changes as a function of time after death due to the change in permeability of the cell membrane within hours of cell death (Polk and Postow 1986). This fact can be a concern when interpreting the results of in-vitro experiments.

Malich et al. in their studies of EIS (Malich, Fritsch et al. 2000; Malich, Boehm et al. 2001; Malich, Bohm et al. 2001; Malich, Bohm et al. 2003) wrote referring Fricke and Morse, Singh et al., Surowiec et al., Jossinet et al. (Fricke and Morse 1926; Singh, Smith et al. 1979; Surowiec, Stuchly et al. 1988; Jossinet 1996; Jossinet 1998) that

> "...in contrast to these observations in normal tissue, malignant tumors show substantially increased capacitance and conductivity values. In vitro studies have shown 20–40-fold higher values for both parameters in malignant as compared to normal tissue (Surowiec, Stuchly et al. 1988)."

Considering these figures and conductivity ranges above, at frequencies of interest ($f = [200–300]$ Hz) we will accept the conductivity ratio between cancerous and normal tissue to vary in the range of [3–40]. There is an acute need for the more accurate in-vivo conductivity measurements of the normal and malignant breast tissue performed in the α-relaxation region. This anticipated study should provide a realistic conductivity model and in-vivo experiments resulting in electrical parameters measured for various normal and cancerous breast tissue samples.

Chapter 4

Imaging Modalities Based on Electrical Impedance Measurements

This chapter elaborates on the current imaging modalities that are based on the electrical conductivity differences between normal and cancerous breast tissues. The techniques of Electrical Impedance Scanning (EIS), Electrical Impedance Tomography (EIT), and Magnetic Resonance Electrical Impedance Tomography (MREIT) are described below. Except for EIS, which is fully developed, tested, and FDA approved, EIT and MREIT are under development and have not been clinically accepted.

4.1 Electrical Impedance Scanning

Electrical Impedance Scanning is an imaging modality that utilizes the different dielectric properties of malignant and benign tissues. Measurements on freshly excited breast tissues conducted by Surowiec et al. (Surowiec, Stuchly et al. 1988), Jossinet et al. (Jossinet 1996; Jossinet 1998), Morimoto et al. (Morimoto, Kinouchi et al. 1990; Morimoto, Kimura et al. 1993), Chauveau et al. (Chauveau, Hamzaoui et al. 1999) showed 3–40 times higher values for conductivity in malignant as compared to normal tissues. These differences are attributed to changes in cellular water and electrolyte content, changes in cell membrane permeability, packing density, and orientation of malignant cells (Malich, Bohm et al. 2003). Electrical Impedance Scanning is an imaging technique that produces the conductance/capacitance maps of the object by means of injecting low currents and measuring voltages on the surface electrodes.

As a pioneering study, during 1980s, the Breast Center Pistoia (Italy) started Electrical Impedance breast imaging with the "Mammoscan". "Mammoscan" comprised an 8×8 matrix of square electrodes and produced 4 images for each breast. Six thousand patients were screened, of which 745 underwent biopsy. Also all patients underwent an examina-

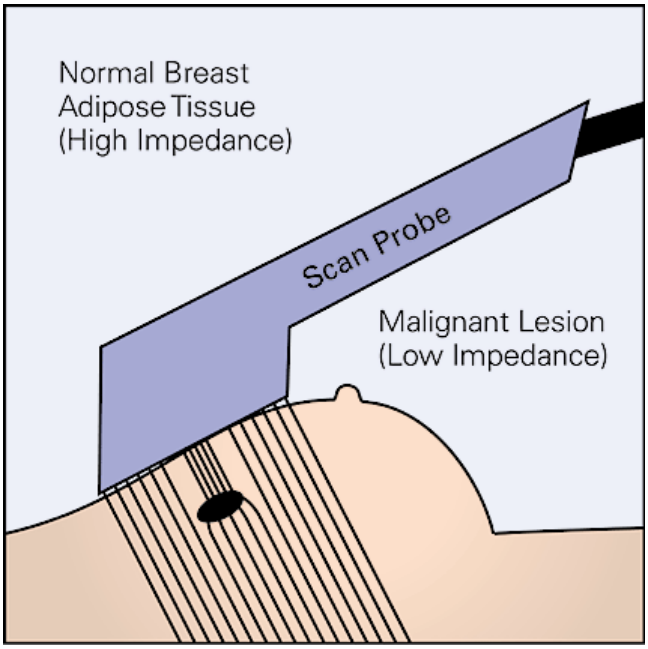

Figure 20.: Electrical Impedance Scanning Principle. Depending on the size, depth, and conductivity ratio of the lesion with respect of the surrounding tissue, the electric field distortions lead to the current signals measurable on the surface (from Diebold, Jacobi et al. 2005).

tion that included palpation, thermograthy, ultrasound, mammography, diaphanoscopy, and EIS. The initial promising results were published in 1990 by Piperno at al. (Piperno, Frei et al. 1990). Where all the tests provided negative results, "Mammoscan" identified nine cases with cancerous findings. In five more cases, "Mammoscan" elucidated ambiguities and pointed out malignancies. Although the FP issue was not specifically addressed in their study, Piperno et al. plaid the groundwork for EIS, recognizing the prospect of using the dielectric properties of breast tissues as a biomarker for cancer detection. Since then the technical equipment, application mode, and algorithms for EIS performance have undergone significant changes.

TransScan TS2000 system (TransScan Research and Development Co., Israel; distributed by Siemens, Erlangen, Germany) received clearance from the United States FDA for use as an adjunct to mammography in cases with equivocal mammograms (F-D-C Reports 1998) and became the only commercially available system for obtaining electrical impedance measurements of the breast (Fig. 21).

Figure 21.: TransScan TS2000 (TransScan Research and Development Co., Ltd, Israel; distributed by Siemens, Erlangen, Germany).

In a TransScan examination, an alternating electric field is applied between the patient's

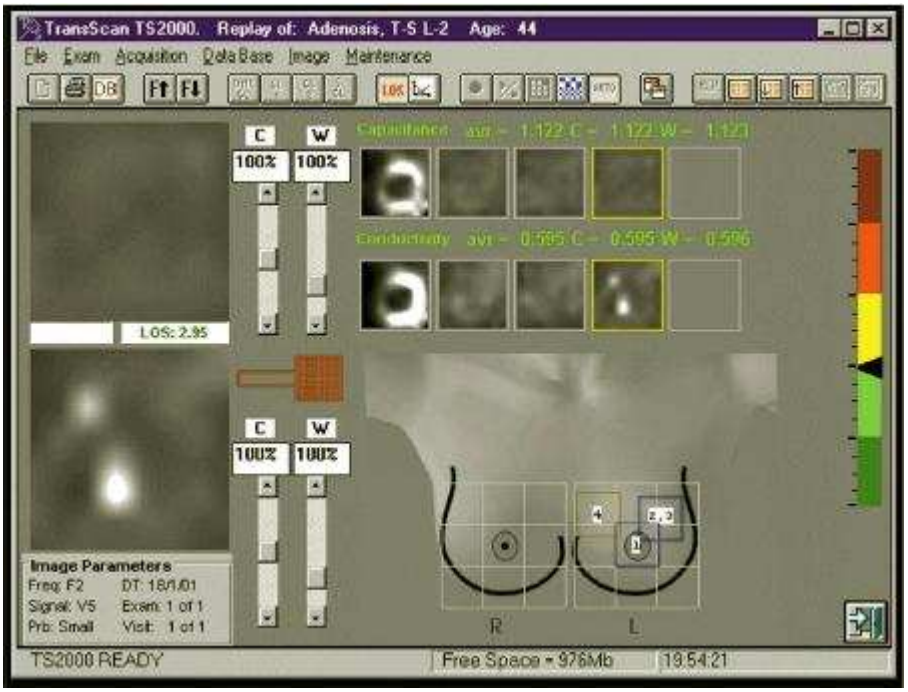

Figure 22.: TransScan examination window (from Diebold, Jacobi et al. 2005).

arm and breast. Analogous to ultrasound examinations of the breast, the patient lies supine with the arm placed above the head. Low-frequency current is applied through the metal cylinder held in the patient's hand. A scan probe (square sensor array) pressed against the breast measures the distribution of the applied current within the breast. The data received by each sensor are mapped to conductivity and capacitance values. The generated maps can either be high- (16×16) or low- (8×8) resolution. Each breast is divided into nine sectors, with two images (conductivity and capacitance) for each section. Normal breast tissues show a homogeneous distribution of the applied current, with uniform conductivity and capacitance values. Cancerous tissues cause an increase of electrical conductivity or capacitance which distorts the electrical field within the breast and appears as a focal brightness (Fig. 22). In the study presented for FDA approval, 704 biopsy-proven lesions were examined using EIS. Eighty percent sensitivity and sixty-eight percent specificity were reported (F-D-C Reports 1998).

Melloul et al. (Melloul, Paz et al. 1999) in their study in 1999 aimed to assess the efficiency of ^{99m}Tc-sestamibi scintimammography (SMM) and TransScan TS2000 as adjunct

modalities (Melloul, Paz et al. 1999). The study included 121 women evaluated by palpation, mammography, SMM, and TransScan. Seventy-nine palpable and 42 non-palpable lesions were identified. All patients underwent either biopsy or mastectomy. Only 18 out of 121 patients had breast carcinoma. It was concluded that SMM had an 88% specificity in breast cancer detection compared to 67% for TranScan TS2000. Nevertheless, five cases diagnosed as malignant by SMM, were correctly identified as benign by TransScan TS2000. The sensitivity of the TransScan (72%) was significantly lower than that of SMM (89%). But as was concluded, due to a complete noninvasiveness, large-scale applicability, and low cost, TransScan deserves further refining.

In their study in 2000, Malich et al. (Malich, Fritsch et al. 2000) aimed to evaluate the reliability of EIS (TranScan TS2000) examining 52 women with 58 sonographically and/or mammographically suspicious findings. Two modes of TranScan performance were used: targeted high-resolution (for localized lesion examination) and standard resolution mode (for a routine breast examination). Out of 58 total lesions, 29 were benign and 29 malignant. In the targeted mode, the sensitivity and specificity achieved were 93% and 65.5%, respectively, and ten FPs were observed. In the lower-resolution standard mode, the sensitivity was lower and specificity was higher, 76% and 72%, respectively, and eight FPs were reported. Malich at al. (Malich, Fritsch et al. 2000) pointed out the limitation to a successful use of Electrical Impedance Scanning such as signals from superficial skin lesions, poor contact, and air bubbles. Also, the detection of the lesions very close to the chest wall was not always possible as the maximal depth of EIS measurements was limited to 3–3.5 cm. Moreover, it was not possible to localize an EIS-positive lesion for biopsy using EIS. Malich et al. (Malich, Fritsch et al. 2000) concluded that EIS could be useful for patients with dense breasts where conventional mammography fails to accurately diagnose. But at the moment, as noted by the authors,

> "the EIS did not seem to prove a deserved existence as an independent imaging modality."

In 2001 Malich et al. (Malich, Boehm et al. 2001) published the extended investigation of the Ultrasound (US), Electrical Impedance Scanning (EIS), and Magnetic Resonance Imaging (MRI) as adjunctive technologies based on 100 mammographically suspicious lesions

examinations. Sixty-two lesions were identified as malignant, and 38 lesions were diagnosed as benign. The table below gives the comparison of system parameters for three imaging technologies in a role of adjunctive modalities. According to the definition, the sensitivity is a statistical measure of how well the test correctly identifies a condition. The specificity is is a statistical measure of how well the test correctly identifies the negative cases or those cases that do not meet the condition under study.

Table 7: Comparison of system parameters of additive breast diagnostic methods: Ultrasound (US), Electrical Impedance Scanning (EIS), and Magnetic Resonance Imaging (MRI) (adopted from Malich, Boehm et al. 2001).

	Sensitivity (%)	Specificity (%)
US	77	89
EIS	81	63
MRI	98	81

The EIS sensitivity results were not significantly improved over those for US, and the EIS specificity was substantially lower than that of US and MRI. Out of eight "border-line" cases (DCIS and hyperplasia), EIS detected five. However, this number was not sufficient to draw a conclusion. Therefore, a further extension of this study is needed to verify the above findings. In the same year, a more comprehensive study (Malich, Bohm et al. 2001) including 240 histologically proven breast lesions indicated that the addition of EIS to mammography and ultrasound increased the sensitivity from 86.4% to 95.1%, but the accuracy decreased from 82.3% to 75.7%. The study also suggested that EIS has a poor detection rate of 57.1% for DCIS.

Assenheimer et al. (Assenheimer, Laver-Moskovitz et al. 2001) in their study published in 2001 showed in their theoretical models that the currents detected at the breast surface translated into two-dimensional maps are related to the electric field distribution within the breast. The infinite medium model was extended to take into account finite depths as well as the effects of the highly resistive skin. Furthermore, a three-element model was

introduced to evaluate the admittance characterizing the underlying tissue, omitting the masking effects of the skin.

Glickman et al. (Glickman, Filo et al. 2002) developed an EIS postprocessing algorithm that automatically recognized bright focal spots in the conductivity map of the breast. In addition, this algorithm discriminated between malignant and benign tissues using two main predictors: phase at 5kHz and crossover frequency at which the imaginary part of admittance is at maximum. The algorithm was tested using the test group of 87 carcinomas, 153 benign cases, and 356 asymptotic cases. Sensitivity of 84% and specificity of 52% were obtained for the test group.

In 2002, Martin et al. (Martin, Martin et al. 2002) studied correlations between the histopathology of the breast malignancy and variations in depths, intensity, multiplicity, and simultaneous capacitance-conductance features of EIS. Data taken from 74 patients with either suspicious or dubious mammography comprised the study. No significant relationship was found between the depth and intensity of EIS signal. Discordance among mammography, EIS, and histology was observed in 15 (20%) cases, six of which were peri-menopausal women. Benign proliferating lesions were diagnosed in six of 15 (40%) controversial cases. Mammography and EIS had similar rates of false-positive findings in this study.

Piperno and Lenington (Piperno and Lenington 2002) in their study in 2002 examined the potential for using EIS as an indicator of the estrogen activity in the breast. TS2000 was used as an examining tool investigating 86 postmenopausal women. The capacitance and conductance were measured at the nipple sector of every breast at 200 Hz and 1100 Hz. The capacitance and conductance decreased with the increase of number of years since the beginning of menopause. Women who used estrogen replacement therapy had a higher nipple conductance. The study concluded that EIS can be a useful noninvasive tool in estrogen level monitoring able to identify a high cancer-risk patients.

In 2005, Stojadinovic et al. (Stojadinovic, Nissan et al. 2005) evaluated the feasibility of EIS for early detection in young women. Their study comprised 29 cancers identified among 1103 women. EIS sensitivity and specificity in women younger than 40 years were reported to be 50% and 90%, respectively. Estrogen use and menopausal status correlated significantly with EIS performance. Stojadinovic's group supported the use of EIS as a

screening modality for early detection of breast cancer and identification of young women who belong to the high cancer-risk group.

Work by Wersebe et al. (Wersebe, Siegmann et al. 2002) also aimed to evaluate the potential of targeted EIS for classifying suspicious breast lesions. One hundred and seventeen patients with 129 breast lesions (71 malignant and 58 benign) were examined with EIS followed by biopsies. The sensitivity of targeted EIS was observed to be 62%, and specificity was 69%. As concluded by Wersebe et al., "EIS showed mediocre overall diagnostic accuracy for classifying suspicious breast lesions."

Contrary results were obtained by Kneeshaw et al. (Kneeshaw, Drew et al. 2002), stating that "EIS is able to differentiate malignant from benign disease associated with clinically occult microcalcification." Only 35 women were examined resulting in nine malignant cases. From EIS imaging alone, sensitivity and specificity were 44% and 54%. The difference between the mean conductivities in malignant and normal breast tissue was significant ($P = 0.034$).

Table 8: Reported performance of EIS.

Reference	Benign	Malignant	Sensitivity(%)	Specificity(%)
(Kneeshaw, Drew et al. 2002)	20	9	44.4	53.8
(Glickman, Filo et al. 2002)	378	83	84	52
(Wersebe, Siegmann et al. 2002)	58	71	62	69
(Malich, Boehm et al. 2001)	38	62	81	63
(Malich, Bohm et al. 2001)	137	103	87.8	66.4
(Malich, Fritsch et al. 2000)	29	29	93.1	65.5
(Melloul, Paz et al. 1999)	103	18	72.2	67
(F-D-C Reports 1998)	520	184	80	68

In conclusion, as shown in Table 8, reported sensitivity varies from 44.4%–93.1%, depending on the study; reported specificity varies less, ranging from 52% to 69%. The visual interpretation of the recorded images leads to a strong interobserver diagnostic variability

revealed by the large variation in sensitivity. Furthermore, particular care is necessary to avoid false-positive readings due to interfering superficial skin lesions, bones, or muscles.

Based on the information reviewed, EIS shows promise as an adjunct modality, but still more work is required. Studies show that the specificity and the sensitivity in detection are increased when more than one modality is used.

The proposed MREIM technique can address EIS limitations. Its advantages over EIS include the following:

- MREIM can significantly reduce the number of FP by the simultaneous investigation of magnetic resonance properties and electric properties of the breast;
- MREIM sensitivity does not depend on the lesion depth inside the breast;
- MREIM does not require manual-probe manipulation; thus, avoiding operator-dependence.

4.2 Electrical Impedance Tomography

Electrical Impedance Tomography (EIT) was mathematically introduced by John B. Webster in 1978. It was developed as an imaging technique in the 1980s to reconstruct the conductivity distribution inside a conducting volume. The difference between EIS and EIT lies in the application of surface electrodes attached to the object through which alternating currents are injected. To obtain the conductance/capacitance maps electric potentials are measured at the surface. The latter condition causes poor spatial resolution of EIT due to a limited number of voltage measurements taken only from the surface. As compared to EIS, it also suffers from less sensitivity to conductivity changes deep inside the volume.

In the Institute of Radio Engineering and Electronics of the Russian Academy of Sciences, Cherepenin et al. (Cherepenin, Karpov et al. 2001; Cherepenin, Karpov et al. 2002) developed an improved EIT system with 256 electrodes (arranged in a square matrix with sides of 12 cm) pressed against the breast and a couple of reference electrodes attached to the patient wrists. This configuration is shown in Fig. 23.

The method of back-projections was used for fast 3-D image reconstruction. This device measured only the magnitude voltage values, so the phase information was ignored. Twenty-one women were examined in two positions: lying and standing. As a result, 86% of

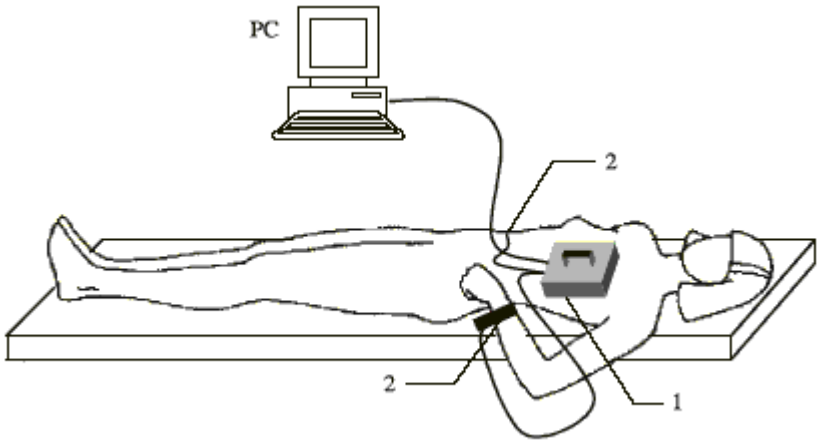

Figure 23.: Physical configuration of the system and measuring procedure: 1 - plane with 256 electrodes, 2 - remote electrodes (from Cherepenin, Karpov et al. 2001).

examinations were found to be fully or partially consistent with diagnoses made by other independent methods. The drawbacks of developed EIT:

- low resolution not allowing detection of lesions smaller than few centimeters,
- deficient electrode contact (the investigators overcame this issue developing a thresholding technique to detect such electrodes and discard information from them),
- the need for image reconstruction technique.

Due to a number of drawbacks, including a limited amount of measured data, low sensitivity of the surface voltage to conductivity changes at regions far from electrodes, and the ill-posedness of the inverse problem involved in image reconstruction, the EIT technique is far from being applied clinically.

4.3 Magnetic Resonance Electrical Impedance Tomography

Magnetic Resonance Electrical Impedance Tomography (MREIT) is another impedance based technique that combines Electrical Impedance Tomography (EIT) with MR that may be useful for diagnostic purposes (Eyübolu, Leigh et al. 2002). The combination of the two principles overcomes some of the reconstruction problems of EIT. In this approach,

a series of electrodes is attached to the sample. Currents are injected, and potentials are measured at the surface during/following the MR acquisition. The MR imaging sequence is applied synchronously with the current application. The phase of the MR data is used to determine the magnetic field due to the multi-orientation applied currents. The current density is determined by first finding the magnetic field (flux density). In some MREIT applications the sample must be rotated to acquire sufficient information to determine the magnetic field (Kwon, Woo et al. 2002; Oh and Han 2003), and other approaches do not require sample re-positioning (Birgul and Eyuboglu 2003). The internal current densities along with the surface potentials measurements are used to determine the volumetric impedivity. The electrode configuration and sample repositioning represent obstacles for clinical applications. As suggested by Oh et al. (Oh and Han 2003), although the MREIT reconstructed conductivity image has poor resolution and signal-to-noise ratio, it might provide contrast in the context of MR imaging. To date, MREIT is only in its developmental stages and has not been tested on human subjects.

Various MREIT techniques have been proposed for direct current (Scott, Joy et al. 1991), alternating current, (Ider and Muftuler 1997; Mikac, Demsar et al. 2001; Muftuler, Hamamura et al. 2004) and radio frequency currents (Scott, Joy et al. 1995). Unlike EIT, the spatial resolution in MREIT is not position-independent. Since only the component of the magnetic flux density in the direction of the bore magnetic field can be measured, a reconstruction technique must be developed to solve the inverse problem of finding the conductivity or current density from only one component of magnetic flux density. It should be emphasized that with this technique, only relative conductivity values can be reconstructed using the magnetic flux density measurements alone. To find the absolute conductivity values, at least one voltage measurement from the boundary is required. The reconstruction algorithms in this technique can also be divided into two groups depending on the data type required. The first group (type 1) uses magnetic flux density directly, whereas in the second group (type 2), the current density distribution is required for image reconstruction.

In Fig. 25, the relation between system variables is explained to illustrate the basis of this classification. For a given object with conductivity distribution, σ, as a result of applied potentials and/or injected currents on the boundary of the object, potential and electric

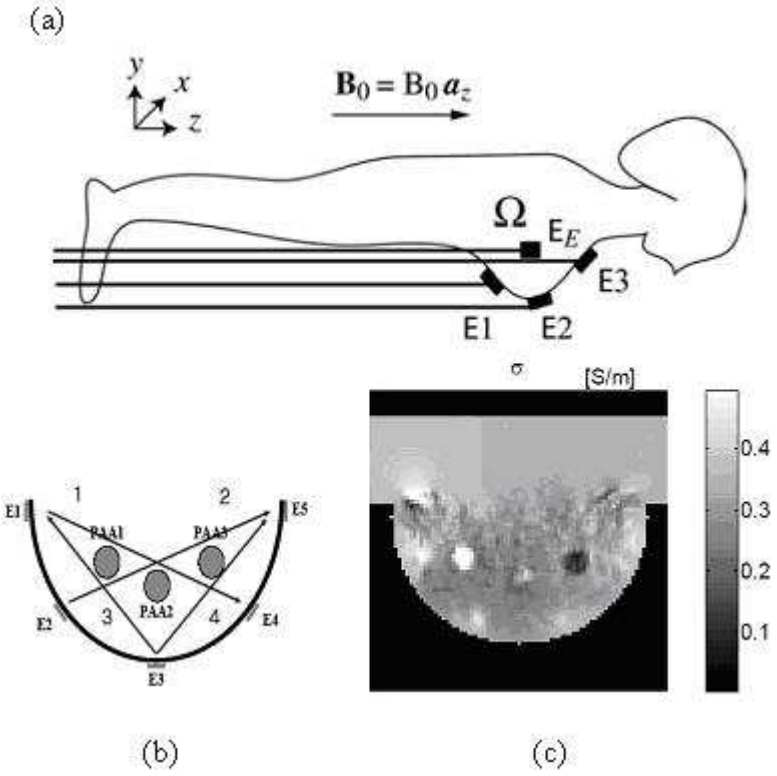

Figure 24.: Magnetic Resonance Electrical Impedance Tomography imaging setup: (a) position of the MREIT electrodes around the patient's breast, (b) projections of the current injection and position of abnormalities in the tested breast phantom, (c) reconstructed conductivity image of the breast phantom (from Oh, Lee et al. 2004).

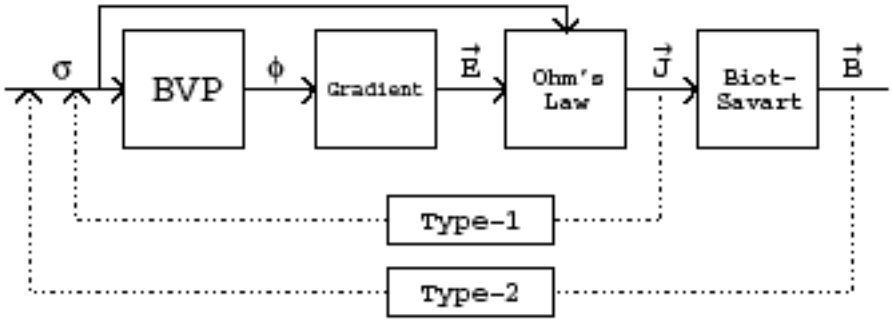

Figure 25.: System variables in the MREIT forward problem and illustration of type 1 and type 2 reconstruction algorithms: BVP represents the related boundary value problem, σ is the conductivity, ϕ is the potential field, E is the electric field, J is the current density, and B is the magnetic flux density. Solid lines show information flow in the forward problem and dotted lines show information flow in type 1 and type 2 reconstruction algorithms (adopted from Birgul and Eyuboglu 2003).

field distributions are generated in the object. The current distribution in the object is given by $\vec{j} = \sigma \cdot \vec{E}$. The internal current distribution $\vec{j}$ sets up the magnetic flux density distribution $\vec{B}$ both inside and outside the object. $\vec{B}$ inside the object can be measured using MRI. From the measured $\vec{B}$, current density can be found from $\vec{j} = (\nabla \times \vec{B})/\mu_0$. In type 1 reconstruction algorithms, $\vec{j}$ is used as data, whereas in type 2 algorithms, $\vec{B}$ is used as data. The algorithms proposed by Zhang (Zhang 1992), Birgul et al. (Birgul, Eyuboglu et al. 2001), Eyuboglu et al. (Eyuboglu, Reddy et al. 2002), and Kwon et al. (Kwon, Woo et al. 2002) are examples of type 1 reconstruction algorithm. The sensitivity matrix approach by Birgul and Ider (Birgul and Ider 1995) is an example of type 2 image reconstruction algorithm.

The major disadvantage of type 1 algorithms is that to find $\vec{j}$ from $\vec{j} = (\nabla \times \vec{B})/\mu_0$, three components of magnetic flux density should be measured using MRI. Since only the z-component of $\vec{B}$, aligned with the direction of main magnetic field, can be measured by magnetic resonance, the object must be rotated. This creates severe experimental limitations. It may also be possible to rotate the main magnetic field of the MRI magnet

by selectively exciting different coils (Birgul, Eyuboglu et al. 2003), but up-to-date MRI systems do not have this capability. In type 2 algorithms, on the other hand, there is an opportunity of using only $\vec{B}_z$ to reconstruct the conductivity.

Birgul et al. (Birgul, Eyuboglu et al. 2003) in their study in 2003 presented the experimental results for 2-D MREIT using the magnetic flux density in one direction. A saline phantom was placed between the electrodes and imaged with a 0.15 T MRI system. A reconstruction algorithm based on the sensitivity matrix between conductivity and only one component of magnetic flux distribution was applied. The relative errors in conductivity values were found to be 13%, 17%, and 14% for three conductivity distributions.

The experimental paper by Oh et al. (Oh and Han 2003) presented the results of MREIT testing using type 1 reconstruction algorithm. The MREIT experiment was conducted with a 0.3 T MRI system on a phantom comprising the two compartments with different electrical conductivities: sausage column (imitation of cancer) and electrolyte (representation of normal breast tissue). The phantom was rotated to obtain the complete information set for reconstruction of current densities. MR current density imaging (MRCDI) was used to measure the current density inside the phantom. Subsequently, the J-substitution algorithm was used for conductivity image reconstruction. The conductivity phantom images obtained with 28 mA injection current showed conductivity errors of 25%.

Due to the severe limitations in reconstruction techniques, MREIT, has not proceeded beyond research. MREIM holds a potential to overcome the drawbacks of MREIT, offering an alternative more effective approach that involves less complexity and risk.

Chapter 5

Fundamentals of MRI

Brief Historical Overview

Nuclear Magnetic Resonance (NMR) was discovered in 1945 by two independent groups: one at Stanford under the leadership of Bloch and the other at MIT under Purcell. Both discoveries were made within a few days of each other and were reported in the same issue of Physical Review (Bloch, Hansen et al. 1946; Purcell, Torrey et al. 1946). Bloch and Purcell later shared the 1952 Nobel Prize for physics in recognition of their pioneering achievements.

Nuclear Magnetism

Magnetic resonance imaging is normally based on the signals arising from the hydrogen nuclei (^{1}H). Human body is mostly fat and water, containing approximately 63% of hydrogen atoms. At the core of atoms is the nucleus consisting of neutrons and protons. Nuclei with an odd number of protons possess spin-angular momentum, postulated by Pauli in 1924. The proton is a spin $\frac{1}{2}\hbar$ particle with the maximum measurable component of the angular momentum of $\frac{\hbar}{2}$, where $\hbar$ is Planck's constant divided by 2π. The partial alignment of nuclear spins brought by the strong magnetic field $\vec{B}_0$ (usually aligned along z axis)(Fig. 26) produces "bulk" (net) magnetization. The magnetic moments or spins are constrained to adopt one of two orientations with respect to $\vec{B}_0$, denoted parallel and anti-parallel. The angles subtended by these orientations and the direction of $\vec{B}_0$ are labeled θ in Figure 27(a). The spin axes are not exactly aligned with $\vec{B}_0$, they precess around $\vec{B}_0$ with a characteristic frequency as shown in Figure 27(b). This is analogous to the motion of a spinning top precessing in the earth's gravitational field. The net magnetization $\vec{M}$ is the vector sum of the individual magnetic moments $\mu = \gamma\frac{\hbar}{2}$, where γ is a gyromagnetic ratio (for ^{1}H, $\gamma = 2\pi \times 42.58$ MHz / T). The net magnetization experiences a torque from the main

magnetic field $\vec{B}_0$, and, as a result, the magnetization precesses around the axis of the magnetic field with an angular frequency called the **Larmor frequency** :

$$\omega = \gamma B_0. \tag{5.1}$$

Equation (5.1) states that angular frequency is directly proportional to applied magnetic field.

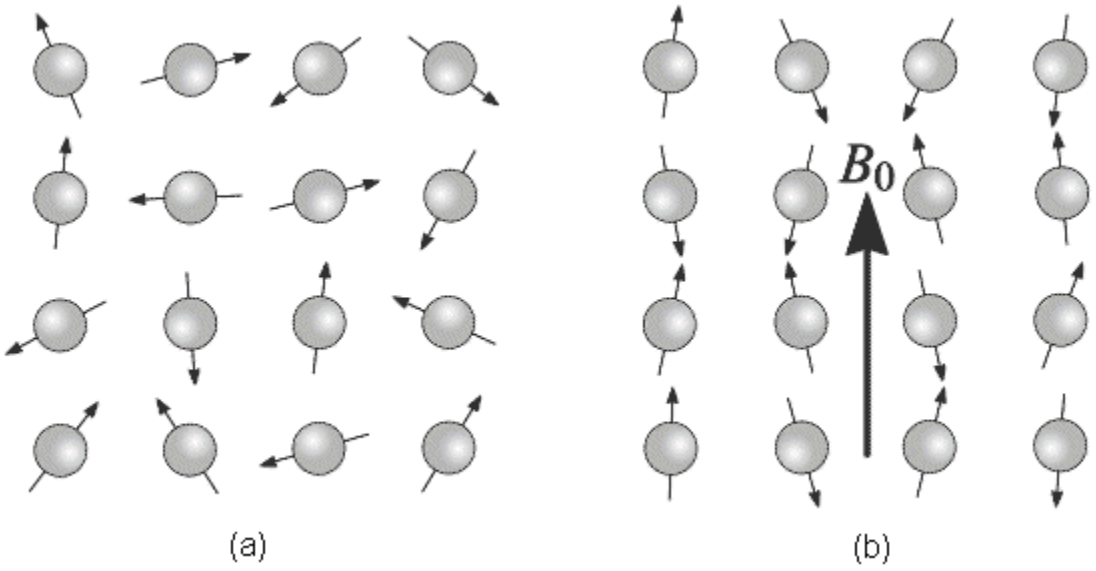

Figure 26.: (a) A collection of ^{1}H nuclei (spinning protons) in the absence of an externally applied magnetic field. The magnetic moments have random orientations. (b) An external magnetic field $\vec{B}_0$ is applied which causes the nuclei to align themselves in one of two orientations with respect to $\vec{B}_0$.

Resonance

Resonance is the induction of transitions between the parallel and antiparallel states of energies (Fig. 27). The energy required to produce this transition equals the difference in energies between the lower and upper state, which is equal to

$$\hbar\omega = \hbar\gamma B_0. \tag{5.2}$$

Resonant absorption of energy by the protons due to an external oscillating magnetic field (radio-frequency field) will occur at the Larmor frequency.

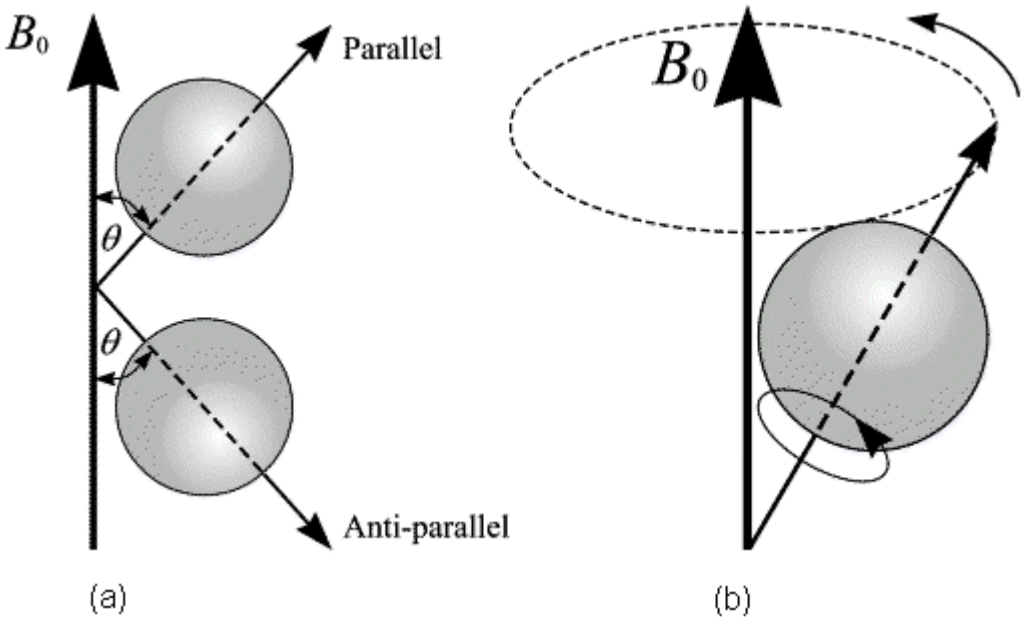

Figure 27.: (a) In the presence of an externally applied magnetic field $\vec{B}_0$, nuclei are constrained to adopt one of two orientations with respect to $\vec{B}_0$. As the nuclei possess spin, these orientations are not exactly at 0 and 180° to $\vec{B}_0$. (b) A magnetic moment precessing around $\vec{B}_0$. Its path describes the surface of a cone.

Radio-Frequency Field

For the MR signal to be detected, a transverse magnetization (orthogonal to $\vec{B}_0$) has to be produced because it is time dependent and, according to Faraday's law of induction, creates voltage in the receiver coil (Fig. 29). The longitudinal magnetization (along $\vec{B}_0$) in thermal equilibrium is static and does not meet the criteria for magnetic induction. Transverse magnetization is produced by the application of a radiofrequency (RF) field $\vec{B}_1$ applied orthogonally to $\vec{B}_0$ precessing at the Larmor frequency (called a 90° RF pulse) (Fig. 28).

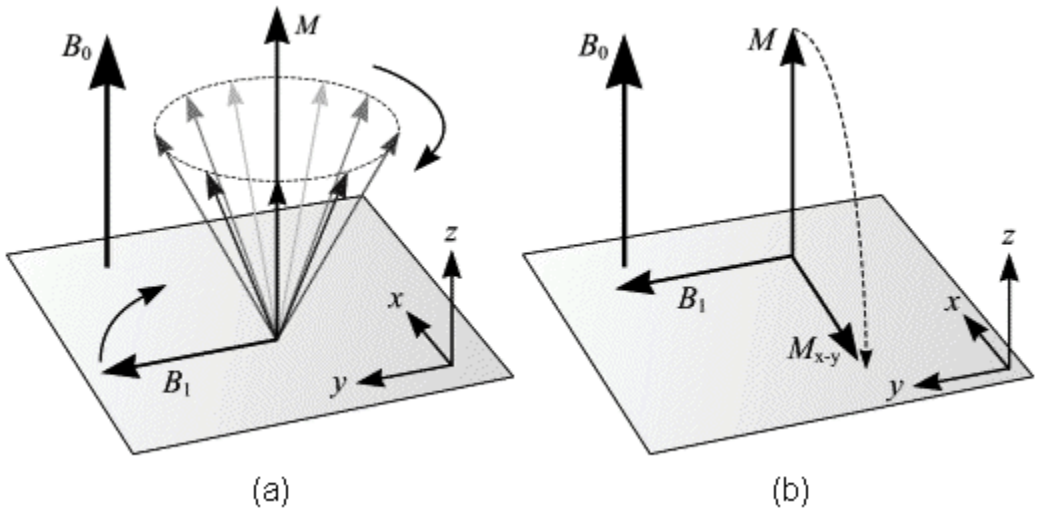

Figure 28.: Tipping of longitudinal magnetization into transverse magnetization by application of the RF field $\vec{B}_1$. The following conditions have to be met in order for all of the longitudinal magnetization to be converted to transverse magnetization: (a) $\vec{B}_1$ has to oscillate at the Larmor frequency, and (b) $\vec{B}_1$ has to be orthogonal to $\vec{B}_0$.

Free-Induction Decay (FID)

After the RF pulse is removed, the magnetization precesses in the transverse x, y plane at the Larmor frequency and can be detected as a time-varying voltage across the ends of a coil oriented as shown in Fig. 29. This transverse magnetization decays exponentially with a time constant $T2$. The generated voltage in a coil is proportional to (Stark and Bradley

1999)

$$V \propto M_0 e^{j\omega t} e^{-t/T2} \tag{5.3}$$

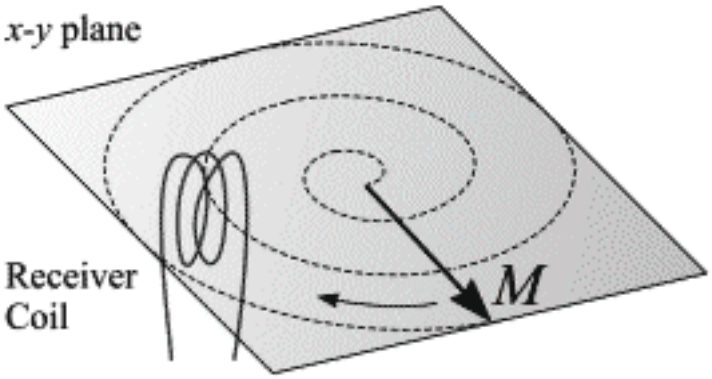

Figure 29.: After 90° RF pulse, $\vec{M}$ oscillates at the Larmor frequency in x, y plane decaying with time constant $T2$. To simplify the description of its motion, a rotating frame of reference is used, where the x and y axes rotate synchronously with $\vec{B}_1$.

$T1$ Relaxation

The RF pulse causes the nuclei to absorb energy bringing them to an excited state. The nuclei can come to the ground state by dissipating this energy to their surroundings, which is called spin-lattice relaxation and describes the longitudinal magnetization recovery towards equilibrium. The time taken for a nucleus to relax back to its equilibrium state depends on the rate that excess energy is dissipated to the lattice. Let M_0 be the amount of magnetization parallel with $\vec{B}_0$ before an RF pulse is applied. The equation governing $T1$ relaxation is

$$M_z = M_0(1 - e^{-t/T1}), \tag{5.4}$$

where M_z and M_0 are the longitudinal and equilibrium magnetizations, respectively.

$T2$ Relaxation

A process called $T2$ relaxation (spin-spin relaxation) denotes the loss of phase coherence caused by interactions between neighboring magnetic moments. Large molecules which orient more slowly than small molecules promote $T2$ relaxation and have shorter $T2$ times (Stark and Bradley 1999). The equation governing $T2$ relaxation is

$$M_{xy} = M_{xy0}e^{-t/T2}, \tag{5.5}$$

where M_{xy} and M_{xy0} are the transverse magnetization and transverse equilibrium magnetization, respectively (Stark and Bradley 1999).

Spin Echo

The transverse magnetization in Free Induction Decay shrinks more rapidly due to the inhomogeneities of the magnetic fields. The corresponding transverse relaxation time constant is thus $T2^*$, which is usually much smaller than T2 and is expressed by the equation below (Stark and Bradley 1999):

$$\frac{1}{T2^*} = \frac{1}{T2} + \frac{1}{T2_{inhom}}. \tag{5.6}$$

A 180° pulse applied at time τ after the 90° pulse can reestablish some of the phase coherence another time τ later in a spin-echo. Spin echo formalism is depicted in Fig. 30 . At $t = 0$, all the spins are in phase. After some time, they start dephasing due to the spin-spin interaction and inhomogenous fields. At time $t = \tau$, the 180° RF pulse reverses the spins into mirror-image position. Finally, at time $t = 2\tau$, the spins synchronize (Stark and Bradley 1999).

Spin Echo Sequence

Most MR techniques use a train of RF pulses comprising the imaging pulse sequence. The Spin Echo (SE) pulse sequence devised by Hahn for NMR spectroscopy in 1950 (Stark and Bradley 1999) was one of the most commonly used pulse sequence in clinical MRI. The SE sequence is shown in Fig. 31. The 90° RF pulse tips the longitudinal magnetization into the transverse plane, where it can be measured. The spins start to dephase in the transverse plane, and the 180° RF pulse is applied at time $t = TE/2$, where ***TE*** is called an **Echo**

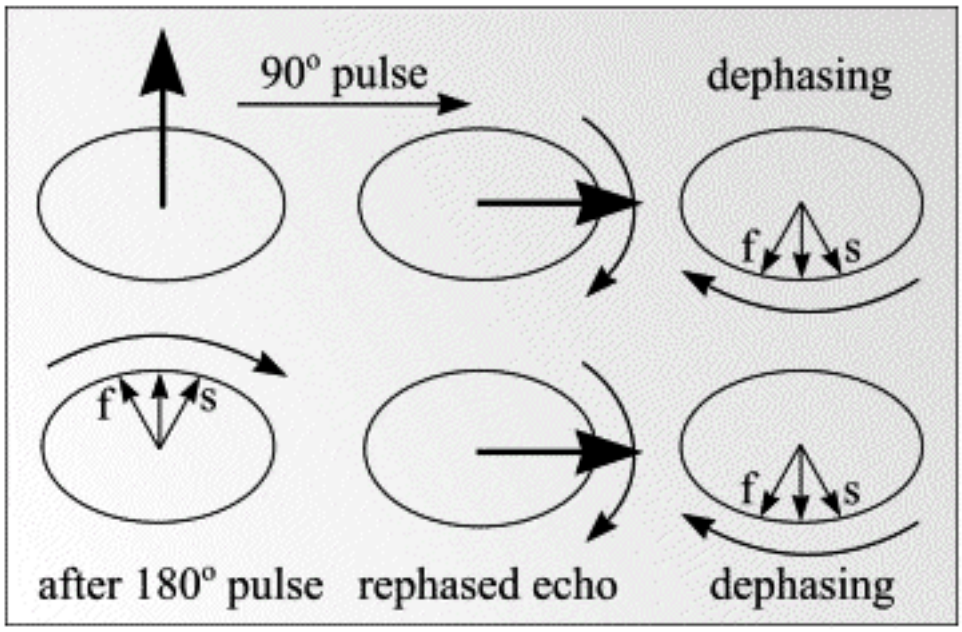

Figure 30.: Transverse magnetization refocusing into a spin echo. Immediately after a 90° pulse, the spins are in phase at time $t = 0$; they start dephasing due to the spin-spin interaction and inhomogeneous magnetic fields; at time $t = \tau$, the 180° RF pulse turns the magnetization into mirror-image position; at time $t = 2\tau$, the fastest precessing spins f, synchronize with slowest spins s, which leads to refocusing of magnetization (Stark and Bradley 1999).

Time, to reorient each component of magnetization. In a singe instant, a maximum number of spins are rephrased forming an echo at time $t = TE/2$ from 180° pulse and $t = TE$ from 90° pulse. The signal is measured for time period of ***TS*** (**Sampling Time**). As time progresses, the transverse magnetization continues to rapidly dephase to zero, and the longitudinal magnetization slowly regrows ($T2 \ll T1$). The remaining time until the next repetition of the sequence permits a sufficient recovery of longitudinal magnetization, which occurs at time ***TR*** (**Repetition Time**), the time from one 90° RF pulse to the next.

The expression for a signal in SE imaging from a voxel with tissue parameters $T1$, $T2$, and effective number of ^1H nuclei per unit volume, ρ_H, will be

$$S_{SE}(TE, TR) = \rho_H \left(1 - 2e^{-(TR-TE/2)/T2} + e^{-TR/T1}\right) e^{-TE/T2}, \tag{5.7}$$

where ρ_H is the spin-density factor, $\left(1 - 2e^{-(TR-TE/2)/T2} + e^{-TR/T1}\right)$ is the $T1$ factor, and $e^{-TE/T2}$ is the $T2$ factor (Stark and Bradley 1999). By varying TR and TE, the Spin Echo can be used to highlight $T1$, $T2$, or spin-density effects (Table 9).

Table 9: Effect of TE and TR on image contrast in Spin Echo Imaging.

Contrast Source	TE	TR
$T1$	As short as possible, limited by bandwidth and noise	Comparable to $T1$s of the two tissues (better toward the shorter $T1$)
$T2$	Comparable to $T2$s of the two tissues (better toward the longer $T2$)	Long compared to $T1$s of the two tissues ($\geq$2000 ms)
ρ_H	As short as possible ($\leq$ 15 ms)	Long compared to $T1$s of the two tissues ($\geq$2000 ms)

Slice Selection

Slice selection is achieved by applying a magnetic gradient in addition to the external magnetic field during the RF pulse. Only one slice within the object will have protons that

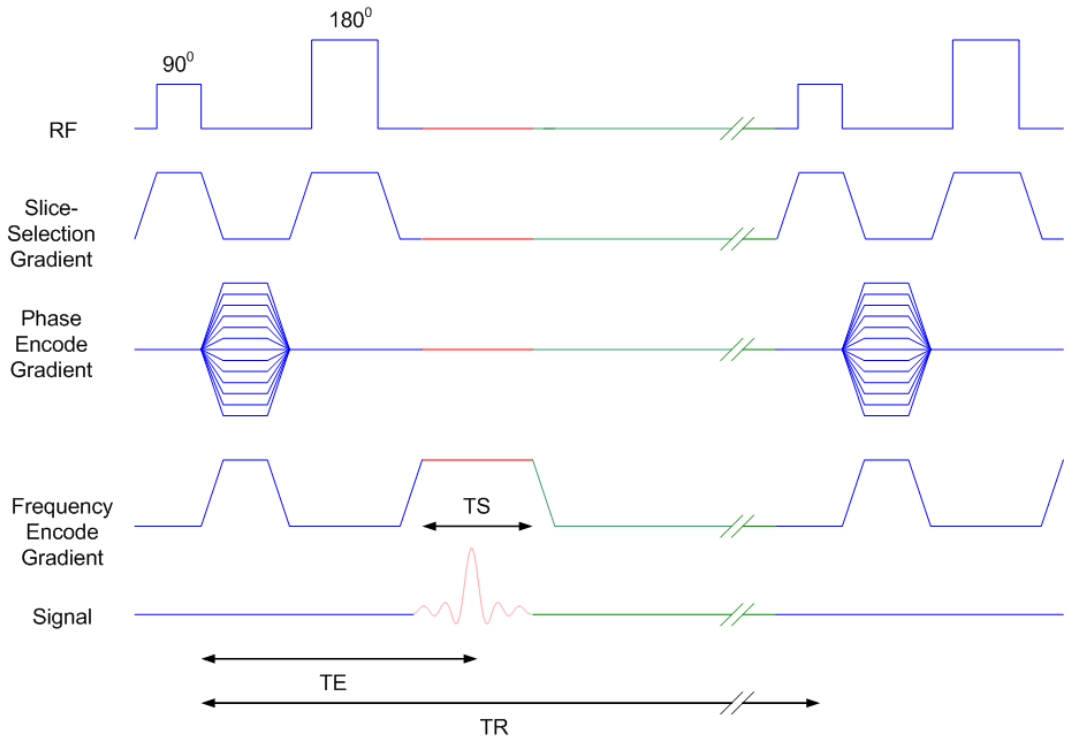

Figure 31.: Pulse timing diagram for Spin Echo sequence. Here, the horizontal axis tracks the time from 0 to Repetition Time (TR), after which the pulse sequence is repeated; the vertical axis represents the strength and polarity of each pulse. The diagram is divided into three following sections: (blue) preparation of transverse magnetization, (red) sampling of echo, and (green) recovery for the next repetition.

are in resonance and contribute to the signal.

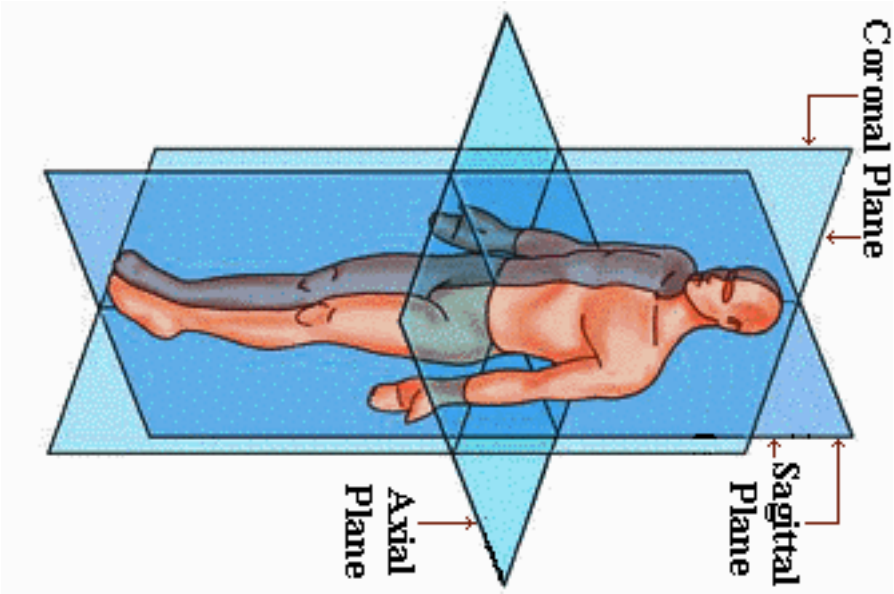

Figure 32.: Slice orientation in MRI (adopted from training.seer.cancer.gov).

If a patient is positioned head first and supine in magnet, an RF pulse in the presence of z gradient creates a transverse slice, and x and y gradients create coronal and sagittal slices, respectively. The slice can be oriented in any plane by combination of gradient strengths.

RF pulses perturb the magnetization within a bandwidth of Larmor frequencies matching the frequencies contained within the RF pulse, which is called its **bandwidth** ($\boldsymbol{BW}$). Longer RF pulses, which have a lower BW, produce thinner slices.

Spatial Encoding

Images can be decomposed mathematically into sine and cosine waves of different frequency and orientation. Frequency and Phase Encode gradients are used to encode the frequency and phase information according to a spatial location.

The **Frequency Encode (FE) gradient** typically consists of two portions with opposite polarity: a prephasing gradient lobe and read out gradient lobe. The purpose of a prephasing lobe is to prepare the transverse magnetization to create an echo signal; the polarity change between the prephasing lobe and read out lobe reverses the directions of phase accumulation of the spins (Bernstein, King et al. 2004) (Fig. 30). Upon frequency gradient G_x application

during the read out, the Larmor frequency is spread out over the range wide enough to distinguish n different locations $x_1, x_2, ..., x_n$ in the rotating reference frame:

$$\omega_{x_i} = \gamma G_x x_i. \tag{5.8}$$

The phase accumulated by spin i due to the read out gradient is

$$\varphi_{x_i} = \int \omega_{x_i} dt = \gamma x_i G_x t. \tag{5.9}$$

Then the frequency encoded signal weighted by spin density $\rho(x)$ is given by (Heine 1993)

$$S(t) = \int \rho(x) e^{j\varphi_x} dx = \int \rho(x) e^{j\gamma G_x x t} dx, \tag{5.10}$$

which indicates that the frequency distribution is proportional to distance, and the signal's amplitude is given by spin density at this location.

Phase Encode (PE) is applied in the orthogonal plane to the slice section and FE gradients. Phase is encoded into MR signals by pulsing magnetic field gradient briefly (1 ms to 5 ms) before each echo is sampled (Stark and Bradley 1999). Phase encoding uses the same principle as frequency encoding, except that the strength of a gradient is changed incrementally before each 180° RF pulse. For a PE gradient G_y, the angular frequency distribution in a B_0 rotating reference frame is

$$\omega_y = \gamma G_y y. \tag{5.11}$$

The phase of the transverse magnetization at the end of PE pulse applied for time τ will be

$$\varphi_y = \int \omega_y dt = \gamma y G_y \tau. \tag{5.12}$$

The PE gradient step is found from (Bernstein, King et al. 2004)

$$\Delta G_y = \frac{G_y(0) - G_y(N_p - 1)}{N_p - 1}, \tag{5.13}$$

where N_p is a number of PE steps.

The MR signal in the transverse plane for a given PE gradient value $G_{y_p} = G_{y_{\min}} + p\Delta G_{y_p}$, assuming a uniform slice selection and neglecting relaxation, will be proportional to (Heine 1993)

$$S(t, G_{y_p}) \propto \iint_{x,y} \rho(x, y) e^{j2\pi\gamma(G_x x t + G_{y_p} y \tau)} dx dy. \tag{5.14}$$

MR Image Reconstruction

MR images are created from digitized MR signals by Fourier transforming the sampled signals. MR signals are digitized in a process called sampling. The total time needed for sampling is called the sampling time TS (described above). The time between consecutive samples is called the sampling interval Δt. The sampling follows the Nyquist theorem which specifies that at least two data samples are acquired between each cycle (Brigham 1988):

$$\frac{1}{\Delta t} = 2BW, \tag{5.15}$$

where BW is the bandwidth. The number of samples from MR signals usually ranges from 128 to 1024 (Stark and Bradley 1999).

Equation (5.14) represents the MR signal in time domain, with the x axis containing the frequency encoded MR signal and y axis containing the phase encoded values. Using continuous approximations, the spatial information of the object being imaged can be obtained through 2-D Fourier Transform:

$$\rho(x,y) \approx \int_{G_{yp}} \int_{t} S(t, G_{y_p}) e^{-j\gamma(G_x x t + G_{y_p} y \tau)} dt dG_{y_p}, \tag{5.16}$$

where G_{y_p} is assumed to be continuous.

The reconstructed spin density is a matrix of complex values split into real and imaginary images. Usually, neither the real nor imaginary images are displayed because the image intensity is distributed indiscriminately between them (Stark and Bradley 1999). Instead, the real and imaginary images are combined into a magnitude image.

Most MR images are presented as 2D planes partitioned into a grid of pixels. The intensity of each pixel represents the strength of the MR signal. Pixels are also referred as voxels to acknowledge that MR image is a slice rather than a plane. Each voxel usually occupies two bytes (16 bits) of memory, allowing 2^{16} possible intensity values. **Field of view (**FOV) is the horizontal or vertical size of an image. It is chosen to match the size of the anatomic area of interest. Its minimum value is determined by the maximum magnetic field gradient strength of the MR system.

Chapter 6

Theoretical Development

In this Chapter, theoretical development for MREIM techniques is presented. First, the aberrational magnetic fields are calculated for a simple geometry (spherical higher conducting tumor embedded in a lower conducting electrically homogenous medium). The flow diagram below (Fig. 33) was followed to derive the analytical expression for aberrational magnetic field (Wollin 2004, Heine, Kovalchuk et al. 2008b).

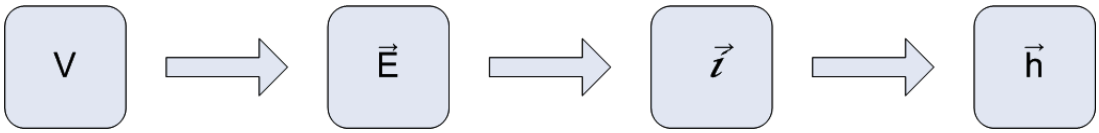

Figure 33.: A diagram followed to derive the analytical expression for aberrational magnetic field created inside and outside of a higher conductive sphere embedded in a lower conducting medium and subjected to a steady-state electric field. The electric potential distribution V inside and outside the sphere is found solving the Boundary Value Problem (Laplace's equation with Dirichlet's and Newman's boundary conditions). Then the electric field strength $\vec{E}$ can be found applying the gradient operator to electric potential. Current density distribution $\vec{i}$ is found using the differential form of Ohm's Law, and magnetic field strength $\vec{h}$ is found from the Maxwell's equation (Ampere's Law).

The numerical solution for the aberrational magnetic field is provided to expand an MREIM study based on a simple geometry/isotropic conductivity model to a more complex irregular shape/anisotropic conductivity distribution model. Numerical solution of the MREIM fields for a simple geometry case is validated against the derived analytical expressions for MREIM fields. This Chapter also provides the theoretical explanation of induced magnetic field effect on formation of Magnetic Resonance image. The initial development

of MREIM effect derivation is provided (Heine, Kovalchuk et al. 2008b). An extension to the previously developed theory is given to further understanding the MREIM effects.

6.1 Analytical Solution for MREIM Fields

According to the BI-RADS mass descriptors (Breast Imaging Reporting and Data System (BI-RADS) Atlas 2007), a sphere is the most common shape for a breast lesion. We will consider a simple tumor model of a sphere of radius R with isotropic electrical conductivity σ_2 embedded in a medium of normal breast tissue of isotropic conductivity σ_1 (Fig. 34). As stated earlier (Chapter 3), the conductivity ratio is in the range $\frac{\sigma_2}{\sigma_1} \cong 3 - 40$. Both the sphere and the surrounding medium are subjected to a uniform electrostatic field of strength E_0 directed along $\vec{z}$ at infinity.

6.1.1 Electric Potential Equations

First, the electric field inside and outside the sphere is found. Electric field relates to the electric potential by the gradient operator:

$$\vec{E} = -\nabla V. \tag{6.1}$$

Since there are no free charges in a conducting medium, Poisson's equation $\nabla^2 V = -\rho/\varepsilon$ (where ε is a permittivity of the medium) reduces to Laplace's equation:

$$\nabla^2 V = 0. \tag{6.2}$$

In spherical coordinates,

$$\nabla^2 V = \frac{1}{r^2}\frac{\partial^2}{\partial r^2}(rV) + \frac{1}{r^2 \sin\theta}\frac{\partial}{\partial\theta}\left(\sin\theta\frac{\partial V}{\partial\theta}\right) + \frac{1}{r^2\sin^2\theta}\frac{\partial^2 V}{\partial\varphi^2}. \tag{6.3}$$

The solution is of the form $V = V(r,\theta)$ due to the symmetry in φ.

Since the solutions to Laplace's equation are unique, a solution which satisfies all the boundary conditions will suffice. Eq. (6.3) becomes

$$\frac{1}{r^2}\frac{\partial^2}{\partial r^2}(rV) + \frac{1}{r^2 \sin\theta}\frac{\partial}{\partial\theta}\left(\sin\theta\frac{\partial V}{\partial\theta}\right) = 0. \tag{6.4}$$

Separation of the variables yields

$$V(r,\theta) = \sum_{l=0}^{\infty}\left(A_l r^l + B_l r^{-(l+1)}\right)P_l(\cos\theta), \tag{6.5}$$

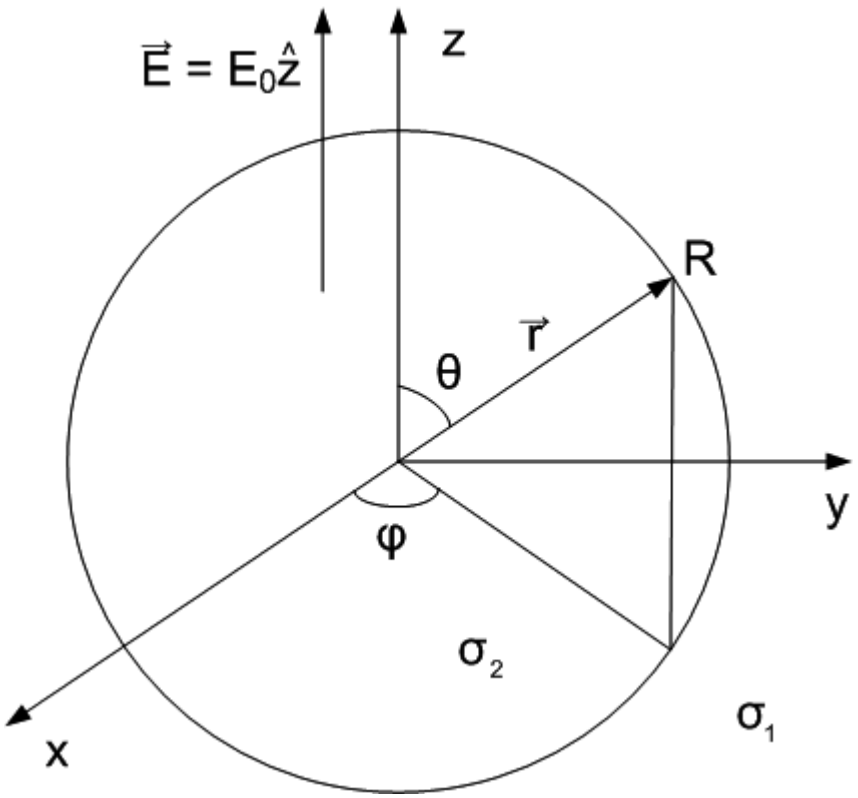

Figure 34.: A simple tumor model used for analytical MREIM developments. A sphere with radius R represents a higher conducting tumor with isotropic conductivity σ_2 embedded in a lower-conducting medium with isotropic conductivity σ_1 and subjected to a quasi-steady-state electric field E_0 along $\vec{z}$ axis.

where l is a positive integer, A_l and B_l are arbitrary constants, and $P_l(\cos\theta)$ is a solution to Legendre's equation (Fitzpatrick 1996)

$$\frac{d}{d(\cos\theta)}\left[\left(1-\cos^2\theta\right)\frac{dP_l}{d(\cos\theta)}\right]+l(l+1)P_l=0, \tag{6.6}$$

which is single-valued and continuous in the interval [-1;1]. $P_l(\cos\theta)$ are known as Legendre polynomials and specified by Rodrigues' formula

$$P_l(\cos\theta)=\frac{1}{2^l l!}\frac{d^l}{d(\cos\theta)^l}\left(\cos^2\theta-1\right)^l. \tag{6.7}$$

For $l=1$, $P_1(\cos\theta)=\frac{1}{2^1!}\frac{d}{d(\cos\theta)}\left(\cos^2\theta-1\right)=\frac{1}{2}(2\cos\theta)=\cos\theta$.

The Legendre polynomials are orthogonal functions that form a complete set of angular functions. The orthogonality relation can be written as

$$\int_{-1}^{1}P_{l'}(\cos\theta)P_l(\cos\theta)\,d(\cos\theta)=\frac{2}{2l+1}\delta_{ll'}. \tag{6.8}$$

It follows that Eq. (6.5) represents a completely general axisymmetric solution for Eq. (6.2). Within the sphere, where $r\le R$,

$$V_2(r,\theta)=\sum_{l=0}^{\infty}A_l r^l P_l(\cos\theta), \tag{6.9}$$

where the term with $r^{-(l+1)}$ is rejected because of divergence as $r\to 0$.

Outside the sphere, $r>R$,

$$V_1(r,\theta)=\sum_{l=0}^{\infty}\left(B_l r^l+C_l r^{-(l+1)}\right)P_l(\cos\theta). \tag{6.10}$$

From the Dirichlet and Neumann boundary conditions

$$\begin{cases}\sigma_1\left.\frac{\partial V_1}{\partial r}\right|_{r=R}=\sigma_2\left.\frac{\partial V_2}{\partial r}\right|_{r=R,} & \vec{i}_{1_N}=\vec{i}_{2_N}\text{ since }\nabla\cdot\vec{i}=0\\ \left.\frac{\partial V_1}{\partial\theta}\right|_{r=R}=\left.\frac{\partial V_2}{\partial\theta}\right|_{r=R,} & \vec{E}_{1_T}=\vec{E}_{2_T}\text{ since }\nabla\times\vec{E}=0\end{cases}, \tag{6.11}$$

where N and T denote a normal and tangential components for current density, $\vec{i}$, and electric field strength, $\vec{E}$. Since $P_1(\cos\theta)=\cos\theta$, the only non-vanishing B_l^* is $B_1^*=-E_0$.

Condition $\left.\frac{\partial V_1}{\partial\theta}\right|_{r=R}=\left.\frac{\partial V_2}{\partial\theta}\right|_{r=R}$ simplifies to

$$V_1|_{r=R}=V_2|_{r=R}.$$

For $l = 1$,

$$\begin{cases} V_1 = \left(-E_0 r + C_1 r^{-2}\right)\cos\theta & r > R \\ V_2 = A_1 r \cos\theta & r \le R \end{cases}. \tag{6.12}$$

Boundary conditions:

$$\begin{cases} \sigma_1 \left.\frac{\partial V_1}{\partial r}\right|_{r=R} = \sigma_2 \left.\frac{\partial V_2}{\partial r}\right|_{r=R} \\ \left.V_1\right|_{r=R} = \left.V_2\right|_{r=R} \end{cases};$$

$$\begin{cases} \sigma_1\left(-E_0 - 2C_1 R^{-3}\right)\cos\theta = \sigma_2 A_1 \cos\theta \\ \left(-E_0 R + C_1 R^{-2}\right)\cos\theta = A_1 R \cos\theta \end{cases}; \quad \begin{cases} -2\sigma_1 C_1 R^{-3} - \sigma_2 A_1 = \sigma_1 E_0 \\ C_1 R^{-2} - A_1 R = E_0 R \end{cases};$$

$$\begin{cases} -2C_1 R^{-3} - \frac{\sigma_2}{\sigma_1} A_1 = E_0 \\ C_1 R^{-3} - A_1 = E_0 \end{cases}. \tag{6.13}$$

This system of equations can be solved by means of the determinants: $\begin{vmatrix} -2R^{-3} & -\frac{\sigma_2}{\sigma_1} \\ R^{-3} & -1 \end{vmatrix} \times \begin{vmatrix} C_1 \\ A_1 \end{vmatrix} = \begin{vmatrix} E_0 \\ E_0 \end{vmatrix}$.

$$C_1 = \frac{\begin{vmatrix} E_0 & -\frac{\sigma_2}{\sigma_1} \\ E_0 & -1 \end{vmatrix}}{\begin{vmatrix} -2R^{-3} & -\frac{\sigma_2}{\sigma_1} \\ R^{-3} & -1 \end{vmatrix}}; \quad A_1 = \frac{\begin{vmatrix} -2R^{-3} & E_0 \\ R^{-3} & E_0 \end{vmatrix}}{\begin{vmatrix} -2R^{-3} & -\frac{\sigma_2}{\sigma_1} \\ R^{-3} & -1 \end{vmatrix}};$$

$$C_1 = \frac{-E_0 + E_0\frac{\sigma_2}{\sigma_1}}{2R^{-3} + \frac{\sigma_2}{\sigma_1}R^{-3}} = \frac{E_0\left(\frac{\sigma_2}{\sigma_1} - 1\right)}{R^{-3}\left(\frac{\sigma_2}{\sigma_1} + 2\right)}; \quad A_1 = \frac{-2R^{-3}E_0 - E_0 R^{-3}}{2R^{-3} + \frac{\sigma_2}{\sigma_1}R^{-3}} = -\frac{3E_0 R^{-3}}{R^{-3}\left(2 + \frac{\sigma_2}{\sigma_1}\right)}.$$

We will denote $\sigma_2/\sigma_1 = \sigma_{ratio}$ as a ratio of conductivity inside and outside the sphere.

$$A_1 = -3E_0(2 + \sigma_{ratio}); \quad C_1 = \frac{(\sigma_{ratio} - 1)}{(\sigma_{ratio} + 2)} E_0 R^3. \tag{6.14}$$

Therefore, the final solution for the potentials is as follows:

$$\begin{cases} V_1 = \left(-E_0 r + \frac{(\sigma_{ratio}-1)}{(\sigma_{ratio}+2)} E_0 R^3 r^{-2}\right)\cos\theta & r > R \\ V_2 = -\frac{3E_0}{(2+\sigma_{ratio})} r\cos\theta & r \le R \end{cases}. \tag{6.15}$$

The solutions to electric potential can be broken down to three parts, inside the tumor, outside in close proximity to tumor, and outside far from tumor

$$\begin{cases} V_a = -E_0 r\cos\theta & r \gg R \\ V_b = \frac{\sigma_{ratio}-1}{\sigma_{ratio}+2} E_0 R^3 r^{-2}\cos\theta & r > R \\ V_c = -\frac{3E_0}{2+\sigma_{ratio}} r\cos\theta & r \leq R \end{cases} . \tag{6.16}$$

6.1.2 Electric Current Density Equations

To find the current density $\vec{i}$ through a tumor and its surroundings, we will use the definition of electric field strength, $\vec{E} = -\vec{\nabla}V$, and differential form of Ohm's law, $\vec{i} = \sigma\vec{E}$.

In spherical coordinates,

$$\vec{\nabla}V = \frac{\partial V}{\partial r}\hat{r} + \frac{1}{r}\frac{\partial V}{\partial\theta}\hat{\theta} + \frac{1}{r\sin\theta}\frac{\partial V}{\partial\varphi}\hat{\varphi}. \tag{6.17}$$

Since there is no dependence on $\hat{\varphi}$, we will neglect the last term in Eq. (6.1).

Thus,

$$\begin{cases} \vec{E}_a = -\frac{\partial V_a}{\partial r}\hat{r} - \frac{1}{r}\frac{\partial V_a}{\partial\theta}\hat{\theta} = E_0\cos\theta\hat{r} - E_0\sin\theta\hat{\theta} = E_0\left(\cos\theta\hat{r} - \sin\theta\hat{\theta}\right) \\ \vec{E}_b = -\frac{\partial V_b}{\partial r}\hat{r} - \frac{1}{r}\frac{\partial V_b}{\partial\theta}\hat{\theta} = \frac{\sigma_{ratio}-1}{\sigma_{ratio}+2}E_0\left(\frac{R}{r}\right)^3\left(2\cos\theta\hat{r} + \sin\theta\hat{\theta}\right) \\ \vec{E}_c = -\frac{\partial V_c}{\partial r}\hat{r} - \frac{1}{r}\frac{\partial V_c}{\partial\theta}\hat{\theta} = \frac{3E_0}{\sigma_{ratio}+2}\left(\cos\theta\hat{r} - \sin\theta\hat{\theta}\right) \end{cases} . \tag{6.18}$$

The electric field strength within the tumor is $\frac{3}{2+\sigma_{ratio}}$ larger than that far from the tumor boundary.

The current density created by the electric fields $\vec{E}_a$, $\vec{E}_b$, and $\vec{E}_c$ is

$$\begin{cases} \vec{i}_a = \sigma_1 E_0\left(\cos\theta\hat{r} - \sin\theta\hat{\theta}\right) & r \gg R \\ \vec{i}_b = \sigma_1\frac{\sigma_{ratio}-1}{\sigma_{ratio}+2}E_0\left(\frac{R}{r}\right)^3\left(2\cos\theta\hat{r} + \sin\theta\hat{\theta}\right) & r > R \\ \vec{i}_c = \frac{3E_0\sigma_2}{\sigma_{ratio}+2}\left(\cos\theta\hat{r} - \sin\theta\hat{\theta}\right) & r \leq R \end{cases} . \tag{6.19}$$

Current density $\vec{i}_a$ is a boundary junction current density. When $\sigma_{ratio} = 1$, two regions (outside and inside the sphere) become one region with the same current density, and current densities inside and outside the sphere will be the same and equal to $\vec{i}_a$.

The difference between the current densities in higher and lower conductivity regions is as follows:

$$\frac{i_c}{i_a} = \frac{3\sigma_{ratio}}{\sigma_{ratio}+2}. \tag{6.20}$$

Thus, the current density inside the tumor is $\frac{3\sigma_{ratio}}{\sigma_{ratio}+2}$ times higher than that of the normal tissue, it does not depend on the size of a tumor and is directed parallel to $\vec{E}_0$, the applied electric field. If $\sigma_{ratio} \gg 1$, the ratio in Eq. (6.20) approaches 3. Using the conductivity minimum and maximum values from a ratio range [3–40] concluded from the review in Chapter 3,

$$\left(\frac{i_c}{i_a}\right)_{\max} = 3 \cdot \frac{40}{42} = 2.86; \quad \left(\frac{i_c}{i_a}\right)_{\min} = 3 \cdot \frac{3}{5} = 1.80. \tag{6.21}$$

Considering $i = \sigma_1 E_0$ as a far field current density, the final expression for the generated current densities inside and outside the tumor is given by

$$\begin{cases} \vec{i}_a = i\left(\cos\theta\hat{r} - \sin\theta\hat{\theta}\right) & r \gg R \\ \vec{i}_b = i\frac{\sigma_{ratio}-1}{\sigma_{ratio}+2}\left(\frac{R}{r}\right)^3\left(2\cos\theta\hat{r} + \sin\theta\hat{\theta}\right) & r > R \\ \vec{i}_c = \frac{3i\sigma_{ratio}}{\sigma_{ratio}+2}\left(\cos\theta\hat{r} - \sin\theta\hat{\theta}\right) & r \leq R \end{cases} . \tag{6.22}$$

6.1.3 Aberrational Magnetic Field Equations

Ampere's law and Stoke's theorem are used to find the magnetic field induced by the currents:

$$\oint \vec{H}d\vec{l} = \iint \vec{i}_{enc}d\vec{a}, \tag{6.23}$$

where $d\vec{l}$ is a differential displacement vector and, in spherical coordinates, is represented by $d\vec{l} = dr\hat{r} + rd\theta\hat{\theta} + r\sin\theta d\varphi\hat{\varphi}$, and $d\vec{a}$ is a differential area vector represented by $d\vec{a} = r\sin\theta dr d\varphi\hat{\theta} + r dr d\theta\hat{\varphi}$.

The surface of the cone with the apex at the origin is chosen as an area of integration. The non-zero $d\vec{l}$ term is $d\vec{l} = r\sin\theta d\varphi\hat{\varphi}$, and

$$\oint \vec{H}d\vec{l} = \oint \vec{H}r\sin\theta d\varphi\hat{\varphi} = \int_0^{2\pi} h_\varphi r\sin\theta d\varphi = 2\pi r h_\varphi \sin\theta, \tag{6.24}$$

where h_φ is a magnetic field in the direction of $\hat{\varphi}$. For the surface of the cone, the non-zero term is as follows:

$$d\vec{a} = r\sin\theta dr d\varphi\hat{\theta}.$$

The current enclosed in the cone is

$$\iint \vec{i}_{enc}d\vec{a} = \iint \vec{i}_c r\sin\theta dr d\varphi\hat{\theta}. \tag{6.25}$$

Magnetic Field Inside the Sphere

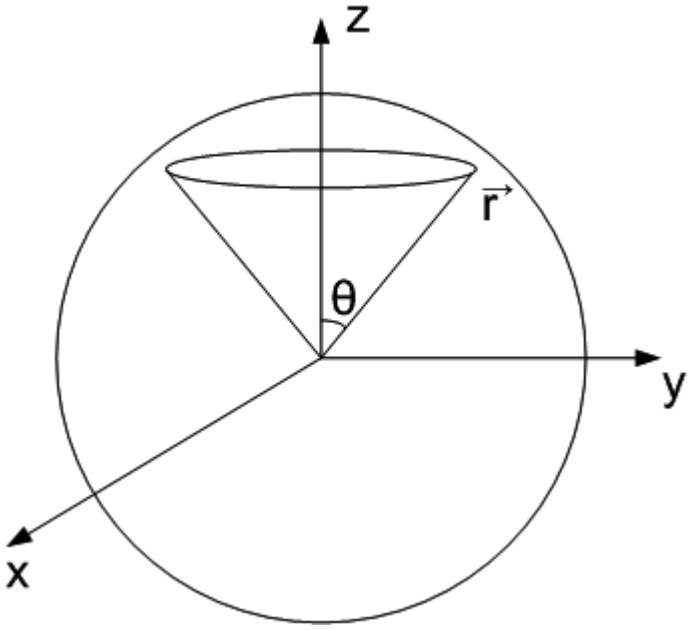

Figure 35.: A closed surface and bounding curve defined as the surface of the cone and mouth of the cone for $r \leq R$, which was used for calculations of magnetic field inside the sphere.

The magnetic field inside the sphere (Fig. 35) can be found using Eq. (6.25)

$$2\pi r \left(h_{\varphi}\right)_2 \sin\theta = -\frac{3i\sigma_{ratio}}{\sigma_{ratio}+2}\int_0^r\int_0^{2\pi} r\sin^2\theta dr d\varphi = -\frac{3i\sigma_{ratio}}{\sigma_{ratio}+2}2\pi\frac{r^2}{2}\sin^2\theta. \tag{6.26}$$

Solving Eq. (6.26) gives

$$\vec{h}_2 = -\frac{3i}{2}\frac{\sigma_{ratio}}{\sigma_{ratio}+2} r\sin\theta\hat{\varphi}, r \leq R. \tag{6.27}$$

Magnetic Field Outside the Sphere

For the field outside the sphere (Fig. 36), the currents within the surface of integration will include the current inside the sphere, $\vec{i}_c$, $(r \leq R)$ and currents outside the sphere, $\vec{i}_a$ and $\vec{i}_b$ $(r > R)$

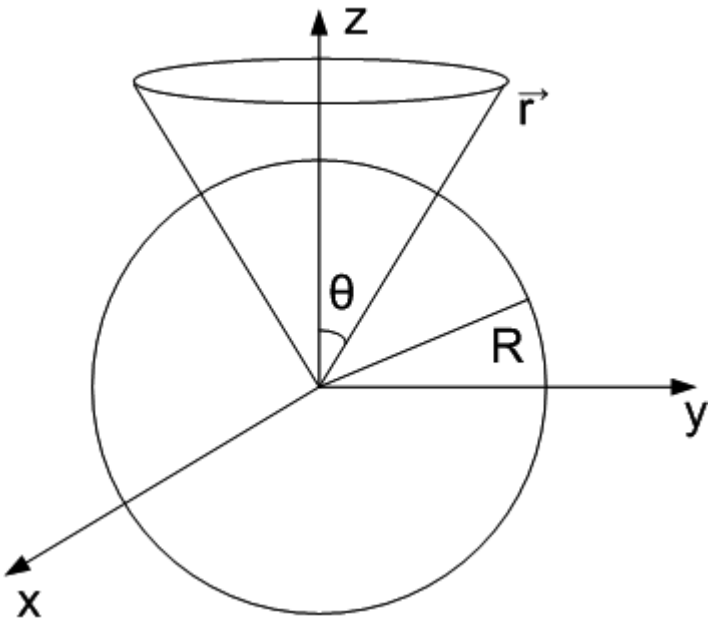

Figure 36.: A closed surface and bounding curve defined as the surface of the cone and mouth of the cone, respectively, for $r > R$, which was used for calculations of magnetic field outside the sphere.

Current density inside the sphere is calculated with the upper limit for $r = R$

$$\iint \vec{i}_{enc} d\vec{a} = \iint \vec{i}_c d\vec{a} = -\frac{3i\sigma_{ratio}}{\sigma_{ratio}+2} \int_0^R \int_0^{2\pi} r \sin^2\theta d\varphi dr = -\frac{3i\sigma_{ratio} 2\pi}{2(\sigma_{ratio}+2)} \sin^2\theta. \tag{6.28}$$

For outside

$$\begin{aligned} &\iint \vec{i}_{enc} d\vec{a} = \iint \left(\vec{i}_a + \vec{i}_b\right) d\vec{a} = -i \int_R^r \int_0^{2\pi} r \sin^2\theta d\varphi dr - \tfrac{\sigma_{ratio}-1}{\sigma_{ratio}+2} R^3 \int_R^r \int_0^{2\pi} r^{-2} \sin^2\theta d\varphi dr \\ &= -i\tfrac{r^2-R^2}{2} 2\pi \sin^2\theta - \tfrac{\sigma_{ratio}-1}{\sigma_{ratio}+2} R^3 2\pi \sin^2\theta \left[\tfrac{1}{r} - \tfrac{1}{R}\right]. \end{aligned} \tag{6.29}$$

The magnetic field outside is

$$\vec{h}_1 = \left(\frac{i}{2}\frac{\sin\theta}{r}\left[-3R^2\frac{\sigma_{ratio}}{\sigma_{ratio}+2} - \left[r^2 - R^2\right] - 2\frac{\sigma_{ratio}-1}{\sigma_{ratio}+2} R^3 \left[\frac{1}{r} - \frac{1}{R}\right]\right]\right)\hat{\varphi}. \tag{6.30}$$

After simplification:

$$\vec{h}_1 = -i\sin\theta\left[\frac{r}{2} - \frac{\sigma_{ratio}-1}{r^2(\sigma_{ratio}+2)} R^3\right]\hat{\varphi},\ \text{r} > \text{R}. \tag{6.31}$$

The slope of aberrational field is [2–3] times greater within the higher conductivity tumor than far outside the tumor taking into consideration [3–40] conductivity ratios.

6.1.4 Aberrational Magnetic Fields in MRI

Only that component of $\vec{h}_1$ and $\vec{h}_2$ aligned with the main magnetic field is effective in producing phase incrementation of the spins (Slichter 1978). In standard MR practice, the main bore time-independent $\vec{B}_0$ field is normally directed along $\hat{z}$. A non-conventional MR coordinate system is used with the main magnetic field directed along $\hat{y}$ (Fig. 37).

The unit vector $\hat{\varphi}$ can be expressed through the Cartesian coordinates as

$$\hat{\varphi} = -\sin\varphi\hat{x} + \cos\varphi\hat{y},$$

which is used to determine the y component of the fields in the Cartesian coordinates.

Inside the sphere, the aberrational magnetic field along the $\hat{y}$ axis is

$$\vec{h}_2 = -\frac{3i}{2}\frac{\sigma_{ratio}}{\sigma_{ratio}+2} r\sin\theta\cos\varphi\hat{y} = -\frac{3i}{2}\frac{\sigma_{ratio}}{\sigma_{ratio}+2} r\sin\theta\frac{x}{r\sin\theta}\hat{y} = -\frac{3i}{2}\frac{\sigma_{ratio}}{\sigma_{ratio}+2} x\hat{y},\ \text{r} \le \text{R}. \tag{6.32}$$

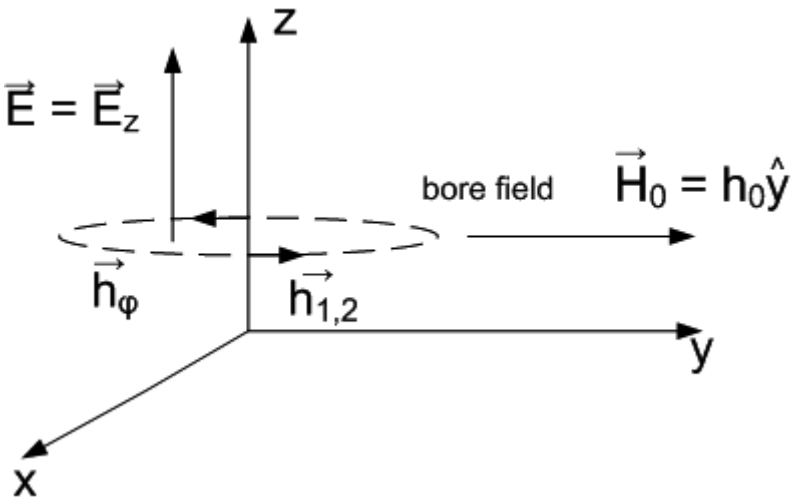

Figure 37.: A non-standard magnetic reference frame with the Bore magnetic field along the $\hat{y}$ direction rather $\hat{z}$ direction (the usual convention). Only those components of the aberrational magnetic field circulating in $\hat{\varphi}$ direction (Eqs. (6.27), (6.31)) and oriented along the main magnetic field are vital.

Outside the sphere,

$$\begin{aligned}\vec{h}_1 &= -i\sin\theta\left[\frac{r}{2} - \frac{\sigma_{ratio}-1}{r^2(\sigma_{ratio}+2)}R^3\right]\cos\varphi\hat{y} = -i\frac{r}{2}\sin\theta\frac{x}{r\sin\theta}\hat{y} + \frac{\sigma_{ratio}-1}{r^2(\sigma_{ratio}+2)}R^3\sin\theta\frac{x}{r\sin\theta}\hat{y} \\ &= -\frac{i}{2}x\hat{y} - \frac{\sigma_{ratio}-1}{(\sigma_{ratio}+2)}R^3 i\left(\frac{x}{r^3}\right)\hat{y} = -\frac{i}{2}x\hat{y} - \frac{\sigma_{ratio}-1}{(\sigma_{ratio}+2)}R^3 i\left(\frac{x}{(x^2+y^2+z^2)^{3/2}}\right)\hat{y},\ \text{r} > \text{R}.\end{aligned} \tag{6.33}$$

Final expressions for induced magnetic fields inside and outside the sphere are

$$\begin{cases} \vec{h}_1 = -\frac{i}{2}x\hat{y} - i\frac{\sigma_{ratio}-1}{(\sigma_{ratio}+2)}R^3\left(\frac{x}{(x^2+y^2+z^2)^{3/2}}\right)\hat{y} & r > R \\ \vec{h}_2 = -\frac{3i}{2}\frac{\sigma_{ratio}}{\sigma_{ratio}+2}x\hat{y} & r \le R \end{cases}. \tag{6.34}$$

6.2 Numerical Solution for MREIM Fields

In a more realistic case of complex tumor geometries and anisotropic conductivities, the analytical solution is no longer obtainable. For periodic quasi-steady-state current flow in a sample with anisotropic conductivity, the continuity equation $\nabla\vec{i} = 0$ can be written as

$$\nabla \cdot \sigma\nabla V = 0, \tag{6.35}$$

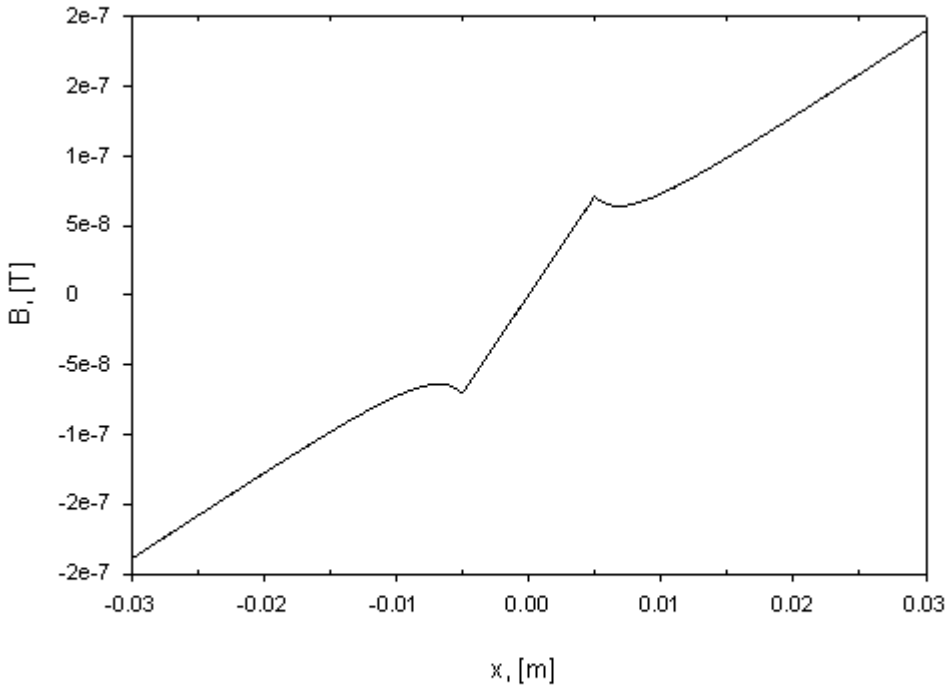

Figure 38.: Aberrational magnetic field (Eq. (6.34)) plotted for $y = z = 0$, conductivity ratio $\sigma_{ratio} = 6$, radius of a tumor $R = 5$ mm, and current density $i = 10$ A/m^2.

where $\vec{i} = \sigma\vec{E}$ and $\vec{E} = -\nabla V$, and σ is a function of space.

From Maxwell's equations $\nabla \times \vec{h} = \vec{i}$ and $\nabla\vec{h} = 0$, the vector identity $\nabla \times (\nabla \times \vec{h}) = \nabla(\nabla \cdot \vec{h}) - \nabla^2\vec{h}$ can be written as

$$\nabla^2\vec{h} = -\nabla \times \vec{i}. \tag{6.36}$$

Using the property of the curl operator and $\nabla \times \nabla V = 0$, Eq. (6.36) becomes

$$\nabla^2\vec{h} = \nabla \times (\sigma\nabla V) = \sigma(\nabla \times \nabla V) + (\nabla\sigma \times \nabla V) = \nabla\sigma \times \nabla V. \tag{6.37}$$

Equation (6.37) can be written in matrix form as follows:

$$\left(\begin{array}{ccc} \nabla^2 h_x\hat{i} & \nabla^2 h_y\hat{j} & \nabla^2 h_z\hat{k} \end{array} \right) = \left| \begin{array}{ccc} \hat{i} & \hat{j} & \hat{k} \\ \frac{\partial\sigma}{\partial x} & \frac{\partial\sigma}{\partial y} & \frac{\partial\sigma}{\partial z} \\ \frac{\partial V}{\partial x} & \frac{\partial V}{\partial y} & \frac{\partial V}{\partial z} \end{array} \right|. \tag{6.38}$$

We are interested only in y-component of magnetic field aligned with the bore field

$$\nabla^2 h_y = \frac{\partial^2 h_y}{\partial x^2} + \frac{\partial^2 h_y}{\partial y^2} + \frac{\partial^2 h_y}{\partial z^2} = -\frac{\partial\sigma}{\partial x}\frac{\partial V}{\partial z} + \frac{\partial\sigma}{\partial z}\frac{\partial V}{\partial x}. \tag{6.39}$$

Two sets of equations, Eqs. (6.35) and (6.39), are solved to find the values for aberrational magnetic field.

The above equations can be solved numerically using the finite difference method (FDM). The finite difference method consists in overlaying the problem with a mesh of lines parallel to the coordinate system and finding an approximate solution to the defining equation at the intersection points on a mesh (Binns, Lowrenson, et al. 1992). The approximation consists of replacing each derivative of the equation by a finite difference expression relating the value of unknown variable at a point with its value at neighboring points.

For the mesh point labeled i, j, k and its immediate neighbors, using Taylor's theorem for two variables, the value of V at a point can be expressed in terms of its neighboring values and separation distance, e.g., in x direction, Δx, as follows:

$$\begin{aligned} V(x + \Delta x) &= V(x) + \Delta x V'(x) + \tfrac{1}{2}\Delta x^2 V''(x) + ...; \\ V(x - \Delta x) &= V(x) - \Delta x V'(x) + \tfrac{1}{2}\Delta x^2 V''(x) + ... \end{aligned} \tag{6.40}$$

Adding and subtracting the above equations gives

$$\begin{aligned} V(x + \Delta x) + V(x - \Delta x) &= 2V(x) + \Delta x^2 V''(x) + ...; \\ V(x + \Delta x) - V(x - \Delta x) &= 2\Delta x V'(x) + ... \end{aligned} \tag{6.41}$$

Changing the notation to the mesh points gives

$$\begin{aligned} V_{i+1,j,k} + V_{i-1,j,k} &= 2V_{i,j,k} + \Delta x^2 V''_{i,j,k}(x) + ...; \\ V_{i+1,j,k} - V_{i-1,j,k} &= 2\Delta x V'_{i,j,k}(x) + ..., \end{aligned} \tag{6.42}$$

which results in

$$\begin{aligned} V''_{i,j,k}(x) &= \frac{\left(V_{i+1,j,k} - 2V_{i,j,k} + V_{i-1,j,k}\right)}{\Delta x^2}; \\ V'_{i,j,k}(x) &= \frac{\left(V_{i+1,j,k} - V_{i-1,j,k}\right)}{2\Delta x}. \end{aligned} \tag{6.43}$$

Approximations to the derivatives in the $\hat{y}$ and $\hat{z}$ directions can be obtained in terms of Δy and Δz in a similar way.

Equation (6.35) can be simplified as follows:

$$\nabla \cdot \sigma \nabla V = \sigma \nabla^2 V + \nabla V \cdot \nabla \sigma = 0. \tag{6.44}$$

Transforming Eq. (6.44) to the FDM notation gives

$$\begin{aligned} &\sigma_{i,j,k} \left(\frac{V_{i+1,j,k} - 2V_{i,j,k} + V_{i-1,j,k}}{\Delta x^2} + \frac{V_{i,j+1,k} - 2V_{i,j,k} + V_{i,j-1,k}}{\Delta y^2} + \frac{V_{i,j,k+1} - 2V_{i,j,k} + V_{i,j,k-1}}{\Delta z^2} \right) \\ &+ \left(\frac{V_{i+1,j,k} - V_{i-1,j,k}}{2\Delta x} + \frac{V_{i,j+1,k} - V_{i,j-1,k}}{2\Delta y} + \frac{V_{i,j,k+1} - V_{i,j,k-1}}{2\Delta z} \right) \\ &\cdot \left(\frac{\sigma_{i+1,j,k} - \sigma_{i-1,j,k}}{2\Delta x} + \frac{\sigma_{i,j+1,k} - \sigma_{i,j-1,k}}{2\Delta y} + \frac{\sigma_{i,j,k+1} - \sigma_{i,j,k-1}}{2\Delta z} \right) = 0. \end{aligned} \tag{6.45}$$

Equation (6.39) becomes

$$\begin{aligned} &\frac{h^y_{i+1,j,k} - 2h^y_{i,j,k} + h^y_{i-1,j,k}}{\Delta x^2} + \frac{h^y_{i,j+1,k} - 2h^y_{i,j,k} + h^y_{i,j-1,k}}{\Delta y^2} + \frac{h^y_{i,j,k+1} - 2h^y_{i,j,k} + h^y_{i,j,k-1}}{\Delta z^2} \\ &= -\left(\frac{\sigma_{i+1,j,k} - \sigma_{i-1,j,k}}{2\Delta x} \right) \left(\frac{V_{i,j,k+1} - V_{i,j,k-1}}{2\Delta z} \right) + \left(\frac{\sigma_{i,j,k+1} - \sigma_{i,j,k-1}}{2\Delta z} \right) \left(\frac{V_{i+1,j,k} - V_{i-1,j,k}}{2\Delta x} \right). \end{aligned} \tag{6.46}$$

Considering the grid with the same step in three directions, $\Delta x = \Delta y = \Delta z$, Eq. (6.45) can be simplified as follows:

$$\begin{aligned} &\frac{\sigma_{i,j,k}}{\Delta x^2} \left(V_{i+1,j,k} + V_{i-1,j,k} + V_{i,j+1,k} + V_{i,j-1,k} + V_{i,j,k+1} + V_{i,j,k-1} - 6V_{i,j,k} \right) \\ &+ \frac{1}{4\Delta x^2} \left(V_{i+1,j,k} - V_{i-1,j,k} + V_{i,j+1,k} - V_{i,j-1,k} + V_{i,j,k+1} - V_{i,j,k-1} \right) \\ &\cdot \left(\sigma_{i+1,j,k} - \sigma_{i-1,j,k} + \sigma_{i,j+1,k} - \sigma_{i,j-1,k} + \sigma_{i,j,k+1} - \sigma_{i,j,k-1} \right) = 0. \end{aligned} \tag{6.47}$$

The solution for $V_{i,j,k}$ can be found as

$$\begin{aligned} V_{i,j,k} &= \frac{1}{6} \left(V_{i+1,j,k} + V_{i-1,j,k} + V_{i,j+1,k} + V_{i,j-1,k} + V_{i,j,k+1} + V_{i,j,k-1} \right) \\ &+ \frac{1}{24\sigma_{i,j,k}} \left(V_{i+1,j,k} - V_{i-1,j,k} + V_{i,j+1,k} - V_{i,j-1,k} + V_{i,j,k+1} - V_{i,j,k-1} \right) \\ &\cdot \left(\sigma_{i+1,j,k} - \sigma_{i-1,j,k} + \sigma_{i,j+1,k} - \sigma_{i,j-1,k} + \sigma_{i,j,k+1} - \sigma_{i,j,k-1} \right). \end{aligned} \tag{6.48}$$

Equation (6.46) will become

$$h^y_{i,j,k} = \frac{1}{6}\left(h^y_{i+1,j,k} + h^y_{i-1,j,k} + h^y_{i,j+1,k} + h^y_{i,j-1,k} + h^y_{i,j,k+1} + h^y_{i,j,k-1}\right) \\ -\frac{1}{24}\left[(\sigma_{i,j,k+1} - \sigma_{i,j,k-1})\,(V_{i+1,j,k} - V_{i-1,j,k}) - (\sigma_{i+1,j,k} - \sigma_{i-1,j,k})\,(V_{i,j,k+1} - V_{i,j,k-1})\right]. \tag{6.49}$$

The mesh point numerical solutions for the electric and magnetic fields can be obtained by averaging neighboring values and correcting this average with the factor containing the differences of neighboring values.

Figure 39 compares the H images at $z = N/2$ obtained from numerical computation and analytical solution for $i = 10$ A/m^2, $\sigma_{ratio} = 20$, and $R = 5$ mm. The paired t-statistic value is $t = 1.70$ with significance of 0.96 which gives 96% probability that the images have the same means (Adams, Orton et al. 2001). Figure 40 shows magnetic-field-strength plots for $z = N/2$ and $y = N/2$ obtained from (a) numerical and (b) analytical solution. Discrepancies between numerically and analytically obtained solutions are caused by the FDM truncation errors (Eqs. (6.40)–(6.42)), tolerance in iterations (accepted precision), etc. Further comparisons for both solutions are provided in terms of the H images for planes $z = N/2 \pm R_{pix}$ and $z = N/2 \pm 2R_{pix}$ (Fig. 41), where $R_{pix} = 5$ pix is the radius of tumor in pixels. The t-statistic values and their significance for images in Fig. 41 were found to be: (a) 0.69 with 0.96 significance, (b) 0.70 with 0.98 significance, (c) 0.70 with 0.96 significance, (d) 0.71 with 0.96 significance, and (e) 0.70 with 0.96 significance.

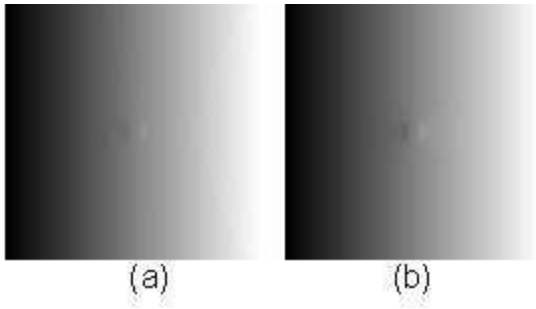

Figure 39.: Comparison of aberrational magnetic field images between (a) numerical solution and (b) analytical solution. The fields are computed for the following parameters: $i = 10$ A/m^2, $\sigma_{ratio} = 20$, and $R = 5$ mm.

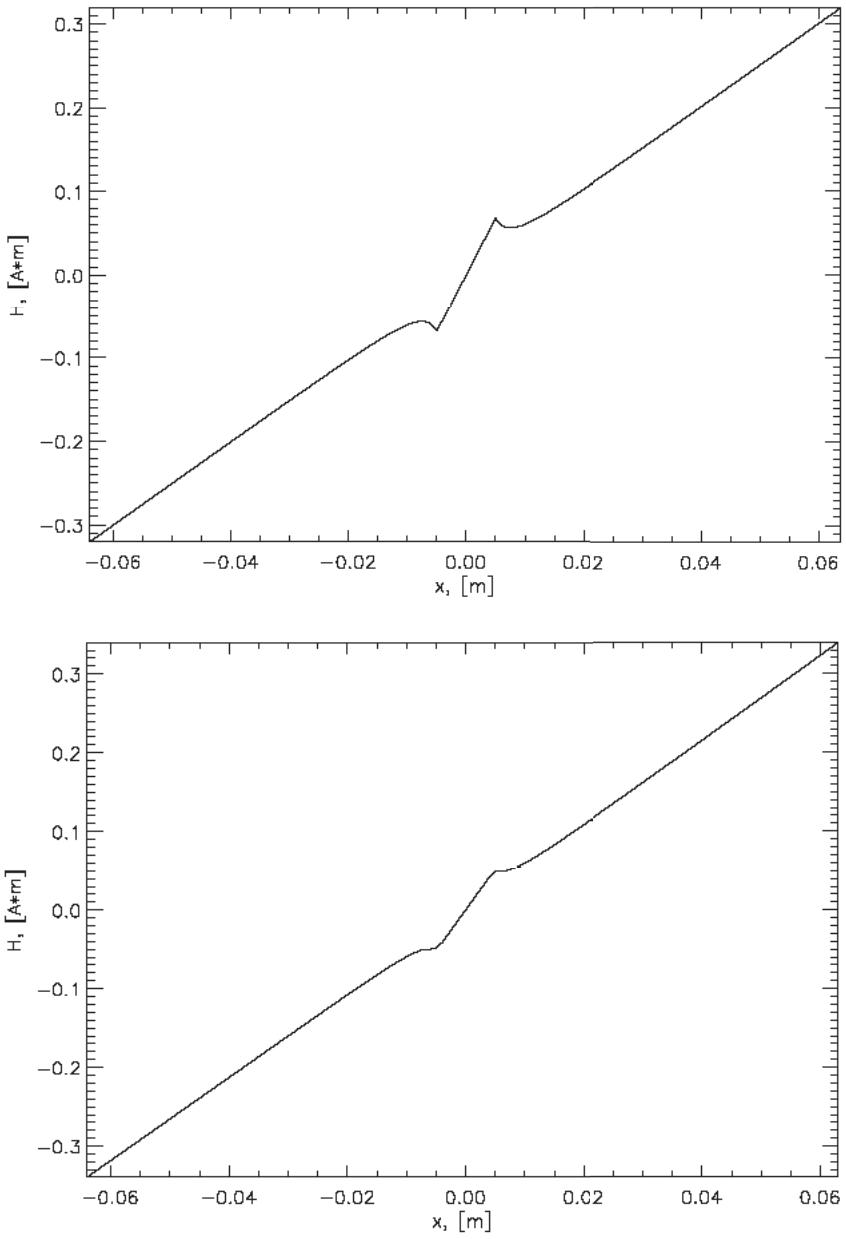

Figure 40.: Comparison of magnetic field plots through $y = N/2$ between (top) analytical solution and (bottom) numerical solution ($i = 10$ A/m^2, $\sigma_{ratio} = 20$, and $R = 5$ mm).

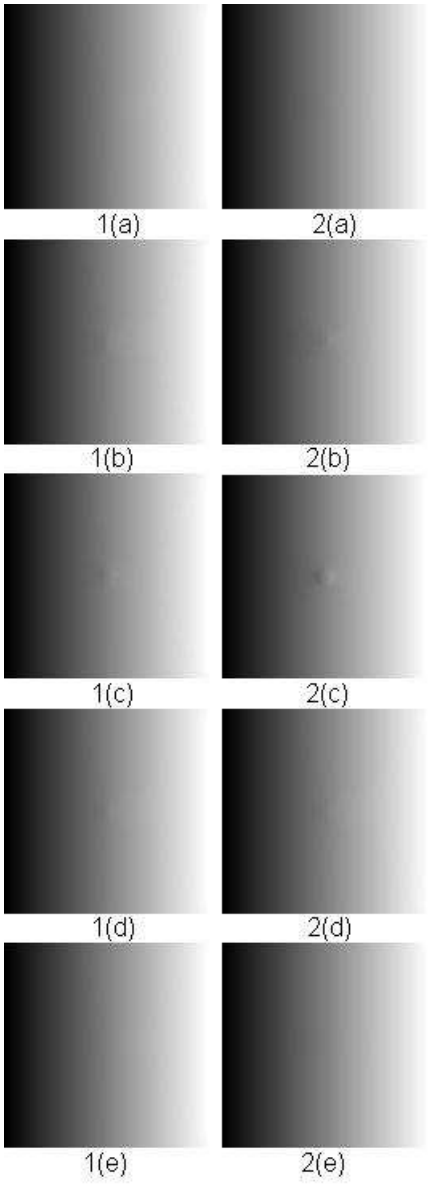

Figure 41.: Comparison of magnetic field strength obtained from numerical (column 1) and analytical solution (column 2) for the following z-planes: (a) $z = N/2 - 2R_{pix}$, (b) $z = N/2 - R_{pix}$, (c) $z = N/2$, (d) $z = N/2 + R_{pix}$, and (e) $z = N/2 + 2R_{pix}$. Magnetic field images were generated for $i = 10$ A/m^2, $R_{pix} = 5$ pix, and $\sigma_{ratio} = 20$.

6.3 Calculation of MR Image Perturbation due to Aberrational Magnetic Field

This Section investigates a native MR image perturbation due to the aberrational magnetic field. The developments below for the FE and PE effects parallel and expand our previous work in this area (Heine, Kovalchuk et al. 2008b).

For spins subjected to a bore magnetic field H_0, constant gradient fields $\vec{G}$, and the aberrational field aligned with the bore field h (derived in the previous sections), the total field H can be found as

$$H = H_0 + \vec{G} \cdot \vec{r} + h\cos(\Omega t + \varphi_0), \tag{6.50}$$

where Ω is the driving angular frequency, and φ_0 is the initial phase angle.

From the nuclear magnetic resonance condition (Eq. 5.2), the spin will have an instantaneous angular velocity

$$\omega = \gamma\mu_0 H = \omega_0 + \gamma\mu_0 \vec{G} \cdot \vec{r} + \gamma\mu_0 h\cos(\Omega t + \varphi_0), \tag{6.51}$$

where $\omega_0 = \gamma\mu_0 H_0$ and $\mu_0 = 4\pi \times 10^{-7}$ is permeability of free space (since the materials imaged by MR generally have low magnetic permeability ($< 10^{-5}$), μ can be replaced by μ_0). The spin will undergo a phase incrementation φ in time in transverse plane such that

$$\varphi = \int_0^t \omega dt = \omega_0 t + \gamma\mu_0 G_x x t + \gamma\mu_0 G_{y_p} y\tau + \frac{\gamma\mu_0 h}{\Omega}\sin(\Omega t + \varphi_0), \tag{6.52}$$

where τ is the time the PE gradient is on. The transverse signal is given by

$$S = \iint \rho^*(x,y) e^{j\varphi_{x,y}} dxdy, \tag{6.53}$$

where $\rho^*(x,y)$ is the proton spin density. Then,

$$S = \iint \rho(x,y) e^{j\gamma(G_x x t + G_{y_p} y\tau)} e^{j\frac{\gamma\mu_0 h(x,y)}{\Omega}\sin(\Omega t+\varphi_0)} dxdy, \tag{6.54}$$

where $\rho(x,y)$ is the effective spin density (including $T1$ and $T2$ effects (Haacke, Brown et al. 1999)). The aberrational term

$$e^{j\frac{\gamma\mu_0 h}{\Omega}\sin(\Omega t+\varphi_0)} = \cos\left[\frac{\gamma\mu_0 h}{\Omega}\sin(\Omega t+\varphi_0)\right] + j\sin\left[\frac{\gamma\mu_0 h}{\Omega}\sin(\Omega t+\varphi_0)\right] \tag{6.55}$$

is considered small (according to the estimation of the aberrational magnetic field (Fig. 38)) in comparison with the main bore field . Taking into account this approximation, $\frac{\gamma\mu_0 h}{\Omega} \ll 1$, $\cos[\frac{\gamma\mu_0 h}{\Omega}\sin(\Omega t+\varphi_0)] \approx 1$, and $\sin[\frac{\gamma\mu_0 h}{\Omega}\sin(\Omega t+\varphi_0)] \approx \frac{\gamma\mu_0 h}{\Omega}\sin(\Omega t+\varphi_0)$, Eq. (6.54) becomes

$$S = \iint \rho(x,y) e^{j\gamma(G_x x t + G_{y_p} y\tau)} \left[1 + j\frac{\gamma\mu_0 h}{\Omega}\sin(\Omega t + \varphi_0)\right] dxdy$$
$$= \iint \rho(x,y) e^{j\gamma(G_x x t + G_{y_p} y\tau)} dxdy + j\iint \rho(x,y) e^{j\gamma(G_x x t + G_{y_p} y\tau)} \frac{\gamma\mu_0 h}{\Omega}\sin(\Omega t + \varphi_0) dxdy. \tag{6.56}$$

Using $\sin(\Omega t + \varphi_0) = \frac{e^{j(\Omega t+\varphi_0)} - e^{-j(\Omega t+\varphi_0)}}{2j}$, the second term of Eq. (6.56) becomes

$$\begin{aligned} &\tfrac{1}{2}\iint \rho(x,y) e^{j\gamma(G_x x t + G_{y_p} y\tau)} \tfrac{\gamma\mu_0 h(x,y)}{\Omega}\left[e^{j(\Omega t+\varphi_0)} - e^{-j(\Omega t+\varphi_0)}\right] dxdy = \\ &= \tfrac{\gamma\mu_0}{2\Omega}\iint \rho(x,y) h(x,y) e^{j\gamma(G_x x t + G_{y_p} y\tau)} \left[e^{j(\Omega t+\varphi_0)} - e^{-j(\Omega t+\varphi_0)}\right] dxdy. \end{aligned} \tag{6.57}$$

6.3.1 MREIM Effect Influencing Frequency Encode Gradient (FE Effect)

The MREIM effect in FE direction was first postulated by Wollin (Wollin 2004; Heine, Kovalchuk et al. 2008b). The frequency encoded signal is

$$S(t) = \int \rho(x) e^{j\gamma G_x x t} e^{j\frac{\gamma\mu_0 h(x)}{\Omega}\sin(\Omega t+\varphi_0)} dx. \tag{6.58}$$

Taking into consideration Eq. (6.57),

$$S(t) = \int_x \rho(x) e^{j\gamma G_x x t} dx + \frac{\gamma\mu_0}{2\Omega}\int_x \rho(x) h(x) e^{j\gamma G_x x t}\left[e^{j(\Omega t+\varphi_0)} - e^{-j(\Omega t+\varphi_0)}\right] dx. \tag{6.59}$$

The second term of Eq. (6.59) gives

$$\frac{\gamma\mu_0}{2\Omega} e^{j\varphi_0}\int_x \rho(x) h(x) e^{j(\gamma G_x x + \Omega)t} dx - \frac{\gamma\mu_0}{2\Omega} e^{-j\varphi_0}\int_x \rho(x) h(x) e^{j(\gamma G_x x - \Omega)t} dx. \tag{6.60}$$

Denoting $2\pi k_x = \gamma G_x t$ and $\frac{\Omega}{\gamma G_x} = \Delta x$, Eq. (6.60) gives

$$\frac{\gamma\mu_0}{2\Omega} e^{j\varphi_0}\int_x \rho(x) h(x) e^{j2\pi k_x(x+\Delta x)} dx - \frac{\gamma\mu_0}{2\Omega} e^{-j\varphi_0}\int_x \rho(x) h(x) e^{j2\pi k_x(x-\Delta x)} dx. \tag{6.61}$$

Taking into consideration the integral from the second term and applying convolution theorem gives

$$\int_x \rho(x) h(x) e^{j2\pi k_x(x-\Delta x)} dx = e^{-j2\pi k_x \Delta x}\int_x \rho(x) h(x) e^{j2\pi k_x x} dx = e^{-j2\pi k_x \Delta x} P(k_x) \otimes H(k_x), \tag{6.62}$$

where $P(k_x)$ and $H(k_x)$ are Fourier transforms of $\rho(x)$ and $h(x)$, respectively. To obtain the spin density function, the inverse Fourier transform is applied

$$\begin{aligned} &\mathscr{F}^{-1}\left[e^{-j2\pi k_x \Delta x} P(k_x) \otimes H(k_x)\right] = \int P(k_x) \otimes H(k_x) e^{-j2\pi k_x \Delta x} e^{-j2\pi k_x x} dk_x \\ &= \int P(k_x) \otimes H(k_x) e^{-j2\pi k_x (x+\Delta x)} dk_x \\ &= \rho(x+\Delta x) \cdot h(x+\Delta x). \end{aligned} \tag{6.63}$$

The final image with the aberration influencing only FE gradient (at t $\rightarrow \infty$) can be expressed as an algebraic sum of three terms:

$$\rho(x) - \frac{\gamma\mu_0}{2\Omega}\rho(x+\Delta x)h(x+\Delta x) + \frac{\gamma\mu_0}{2\Omega}\rho(x-\Delta x)h(x-\Delta x). \tag{6.64}$$

The perturbation produces original image and two filtered replicas of the original image scaled by factor inversely proportional to generator frequency and directly proportional to aberrational magnetic field and shifted by Δx.

The shift is determined by $\Delta x = \frac{f}{df}dx$ (dx is the pixel width) or $\Delta x_{pix} = \frac{f}{df}$ pixels. E.g., for $f = 300$ Hz and $df = 60$ Hz/pix, the shift is 5 pixels.

Figure 42 shows FE in the simulated images (Eq. (6.58)) for a higher conducting disk ($\sigma_{ratio} = 20$) with radius of $R = 5$ mm, current density $i = 10$ A/m^2. Here frequency resolution is $df = 60$ Hz/pix, and generator frequency was varied to produce the shift $\Delta x_{pix} = \frac{f}{df} = 1, 2, ..., 10$ pixels. These results are checked and verified against the images generated using Eq. (6.64).

From Fig. 42 it follows that FE effect is the most conspicuous and allows for tumor shape differentiation if the shift is minimal, e.g. $\Delta x = [1, R]$. After the shift value crosses the radius limit, the shape of tumor can no longer be outlined. This assertion is further supported in Section 8.2.2. Frequency Encode effect is dependent on $\frac{f}{df}dx$ factor and radius combination, aberrational magnetic field strength h (thus, applied current and conductivity ratio), and initial contrast of higher conducting region and its surroundings. These parameters will be further tested in Section 8.2.2.

6.3.2 MREIM Effect Influencing Phase Encode Gradient (PE Effect)

For a particular value of PE gradient G_{y_p}, the signal is

$$S(G_{y_p}) = \int \rho(y) e^{j\gamma G_{y_p} y\tau} e^{j\gamma\mu_0 h(y)\int_t \cos(\Omega t+\varphi_0)dt} dy. \tag{6.65}$$

For a specific value of phase encode, the aberrational term will go through two stages in the spin echo sequence:

- accumulation of the phase before the 180° refocusing pulse, $t \in \left[0; \frac{TE}{2}\right]$;

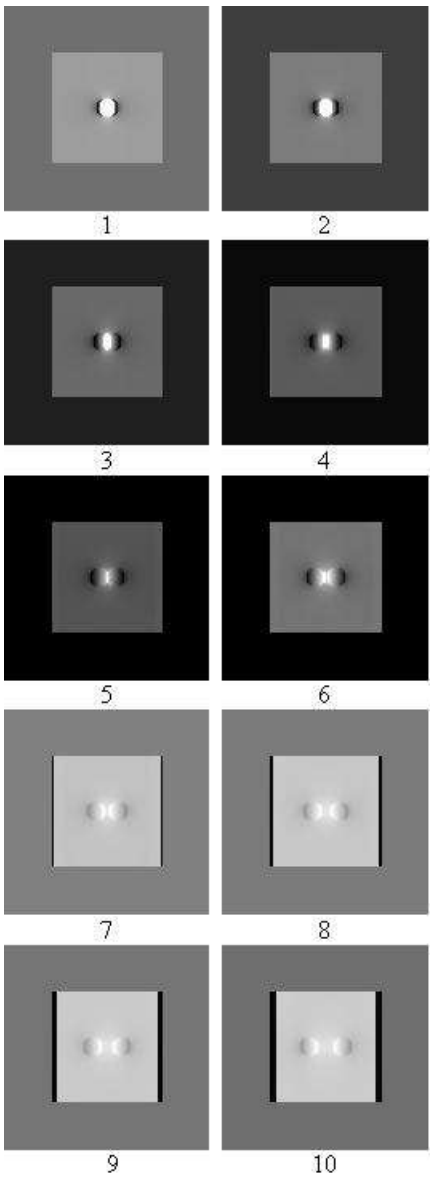

Figure 42.: FE effect in simulated difference images acquired with current on and off for the higher conducting disk ($\sigma_{ratio} = 20$) with radius of $R = 5$ mm, current density $i = 10$ A/m^2, and frequency resolution $df = 60$ Hz/pix. The generator frequency was varied to produce the shift $\Delta x_{pix} = \frac{f}{df} = 1, 2, ..., 10$ pixels (Δx_{pix} is given below the image).

- accumulation of phase after refocusing pulse but before the FE ("read") gradient, $t \in \left[\frac{TE}{2}; TE - \frac{TS}{2}\right]$.

For the maximum PE gradient value, accumulation of phase before the 180° pulse gives

$$\int_0^{TE/2} \cos(\Omega t + \varphi_0) dt = \frac{1}{\Omega}\left[\sin\left(\Omega\frac{TE}{2} + \varphi_0\right) - \sin\left(\varphi_0\right)\right]. \tag{6.66}$$

The second part will cover the phase accumulation from the 180° pulse to the beginning of echo

$$-\int_{TE/2}^{TE-TS/2} \cos(\Omega t + \varphi_0) dt = -\frac{1}{\Omega}\left[\sin\left(\Omega(TE - \frac{TS}{2}) + \varphi_0\right) - \sin\left(\Omega\frac{TE}{2} + \varphi_0\right)\right]. \tag{6.67}$$

For the consequent PE gradient value, the lower time limit starts with TR

$$\int_{TR}^{TR+TE/2} \cos(\Omega t + \varphi_0) dt = \frac{1}{\Omega}\left[\sin\left(\Omega(TR + \frac{TE}{2}) + \varphi_0\right) - \sin\left(\Omega \cdot TR + \varphi_0\right)\right]; \tag{6.68}$$

$$\begin{aligned} &-\int_{TR+TE/2}^{TR+TE-TS/2} \cos(\Omega t + \varphi_0) dt \\ &= -\tfrac{1}{\Omega}\left[\sin\left(\Omega(TR + TE - \tfrac{TS}{2}) + \varphi_0\right) - \sin\left(\Omega(TR + \tfrac{TE}{2}) + \varphi_0\right)\right]. \end{aligned} \tag{6.69}$$

Using the induction method, the generalized formula for the p-th encode line can be obtained:

$$\int_{TR\cdot p}^{TR\cdot p+TE/2} \cos(\Omega t + \varphi_0) dt = \frac{1}{\Omega}\left[\sin\left(\Omega(TR \cdot p + \frac{TE}{2}) + \varphi_0\right) - \sin\left(\Omega \cdot TR \cdot p + \varphi_0\right)\right]; \tag{6.70}$$

$$\begin{aligned} &-\int_{TR\cdot p+TE/2}^{TR\cdot p+TE-TS/2} \cos(\Omega t + \varphi_0) dt \\ &= -\tfrac{1}{\Omega}\left[\sin\left(\Omega(TR \cdot p + TE - \tfrac{TS}{2}) + \varphi_0\right) - \sin\left(\Omega(TR \cdot p + \tfrac{TE}{2}) + \varphi_0\right)\right]. \end{aligned} \tag{6.71}$$

Adding these two terms together gives

$$\frac{1}{\Omega}\left[2\sin(\Omega(TR \cdot p + \frac{TE}{2}) + \varphi_0) - \sin(\Omega \cdot TR \cdot p + \varphi_0) - \sin(\Omega(TR \cdot p + TE - \frac{TS}{2}) + \varphi_0)\right]. \tag{6.72}$$

To simplify Eq. (6.72), the following notation is used $\theta = \Omega \cdot TR \cdot p + \varphi_0$. Then using the trigonometric identities for sine of the sum of angles gives

$$\begin{aligned}
&\tfrac{1}{\Omega}\left[2\sin(\theta + \Omega\tfrac{TE}{2}) - \sin\theta - \sin(\theta + \Omega \cdot TE - \Omega \cdot \tfrac{TS}{2})\right] \\
&= \tfrac{1}{\Omega}\left[\begin{array}{l} 2\left(\sin\theta\cos(\Omega\tfrac{TE}{2}) + \cos\theta\sin(\Omega\tfrac{TE}{2})\right) - \sin\theta \\ -\left(\sin\theta\cos(\Omega \cdot TE - \Omega \cdot \tfrac{TS}{2}) + \cos\theta\sin(\Omega \cdot TE - \Omega \cdot \tfrac{TS}{2})\right) \end{array}\right] \\
&= \tfrac{1}{\Omega}\left[\begin{array}{l} \sin\theta\left(2\cos(\Omega\tfrac{TE}{2}) - 1 - \cos(\Omega \cdot TE - \Omega \cdot \tfrac{TS}{2})\right) \\ +\cos\theta\left(\sin(\Omega\tfrac{TE}{2}) + \sin(\Omega \cdot TE - \Omega \cdot \tfrac{TS}{2})\right) \end{array}\right].
\end{aligned} \tag{6.73}$$

Equation (6.73) can be expressed as the sinusoidal function with the following parameters:

$$\frac{1}{\Omega}A\sin(\theta + \alpha) = \frac{1}{\Omega}A\sin(\Omega \cdot TR \cdot p + \varphi_0 + \alpha), \tag{6.74}$$

where $A = \sqrt{C_1^2 + C_2^2}$ and $\left\{\begin{array}{l} \alpha = \arccos\left(\frac{C_1}{\sqrt{C_1^2+C_2^2}}\right) \\ \alpha = \arcsin\left(\frac{C_2}{\sqrt{C_1^2+C_2^2}}\right) \end{array}\right.$,

$$\left\{\begin{array}{l} C_1 = 2\cos(\Omega\tfrac{TE}{2}) - 1 - \cos(\Omega \cdot TE - \Omega \cdot \tfrac{TS}{2}) \\ C_2 = \sin(\Omega\tfrac{TE}{2}) + \sin(\Omega \cdot TE - \Omega \cdot \tfrac{TS}{2}) \end{array}\right. .$$

Taking into consideration

$$\int_0^t \cos(\Omega t + \varphi_0)dt = \frac{1}{\Omega}A\sin(\Omega \cdot TR \cdot p + \varphi_0 + \alpha),$$

Equation (6.54) becomes

$$\begin{aligned}
&S(t, G_{y_p}) = \textstyle\int \rho(y) e^{j\gamma G_{y_p} y\tau} e^{j\frac{\gamma\mu_0 h(y) A}{\Omega}\sin(\Omega \cdot TR \cdot p + \varphi_0 + \alpha)} dy \\
&\approx \textstyle\int \rho(y) e^{j\gamma G_{y_p} y\tau} dy + \frac{\gamma\mu_0 A}{2\Omega}\int \rho(y)h(y) e^{j\gamma G_{y_p} y\tau}\left[e^{j(\Omega \cdot TR \cdot p + \varphi_0 + \alpha)} - e^{-j(\Omega \cdot TR \cdot p + \varphi_0 + \alpha)}\right] dy.
\end{aligned} \tag{6.75}$$

According to periodicity of sine, $sin(\Omega \cdot TR \cdot p + \varphi_0 + \alpha) = sin(2\pi[f \cdot TR] \cdot p + 2\pi\{f \cdot TR\} \cdot p + \varphi_0 + \alpha) = sin(2\pi\{f \cdot TR\} \cdot p + \varphi_0 + \alpha)$, where $[f \cdot TR]$ and $\{f \cdot TR\}$ denote integer and fractional parts of $f \cdot TR$, correspondingly. The phase difference angles φ_0 and α are constants and do not depend on y or p, they can be factored out of the integration because they have no effect on magnitude image.

Denoting $2\pi k_y = \gamma G_{y_p}\tau$ and $\frac{2\pi \cdot \{f \cdot TR\} \cdot p}{\gamma G_{y_p}\tau} = \Delta y$, applying the Fourier shift theorem and convolution theorem gives

$$\rho(y) + \frac{\gamma\mu_0 A}{2\Omega}\rho(y - \Delta y)h(y - \Delta y) - \frac{\gamma\mu_0 A}{2\Omega}\rho(y + \Delta y)h(y + \Delta y). \tag{6.76}$$

In case of sequential PE mode, FE effect is analogous to PE effect which consists in producing the original image and two aberrational images shifted along $\hat{y}$ direction. The shift is proportional to generator frequency and inversely proportional to PE gradient. Thus, the perturbation caused by the applied current is the strongest for the weakest PE gradients. The shift is expressed as $\Delta y = \{f \cdot TR\} \cdot fov_y = \{f \cdot TR\} \cdot N_p \cdot dy$ or in pixels, $\Delta y_{pix} = \{f \cdot TR\} \cdot N_p$. In case of $TR = 2$ s, PE effect is observed only when the generator frequency is fractional, e.g., for number of PE steps $N_p = 128$, $TR = 2.0$ s for $f = n + 0.004$, where $n \in \mathbb{N}$, the shift is $\Delta y = 1$ pixel.

Figure 43 shows the simulated 128×128 images (Eq. (6.65)) for a higher conducting disk ($\sigma_{ratio} = 20$) with radius of $R = 5$ mm at current density $i = 10$ A/m^2. If $TR = 2$ s, the shift Δy is produced by fractional generator frequencies $\Delta y = \{f\} \cdot TR \cdot N_p \cdot dy$. These images were compared and validated using the simulation images resulting from Eq. (6.76).

The PE effect is particular for selected sequence. For each PE line, the phase accumulation occurs, which in turn misregisters the spatial frequencies in $\hat{y}$ direction. For a SE sequence, the phase accumulation starts from 90° RF pulse to the beginning of frequency encoding. If the PE mode is sequential, e.i., the PE gradient strength discretely changes as $G_{y_p} = G_{y_{max}} - \Delta G_y \cdot p$ with step $\Delta G_y = \frac{2G_{y_{max}}}{N-1}$ and $p \in \mathbb{N}$, then the aberrational term influencing PE will contain the periodic function $\frac{1}{\Omega} A \sin(\Omega \cdot TR \cdot p + \varphi_0 + \alpha)$. The PE effect is similar to FE effect producing the shift, but in $\hat{y}$ direction. For the specific case of integer $TR = 2$ s, only fractional frequencies produce PE effect, since any integer f will eliminate aberrational term dependence on PE index ($\frac{1}{2\pi \cdot n} A \sin(2\pi \cdot n \cdot TR \cdot p + \varphi_0 + \alpha) = \frac{1}{2\pi \cdot n} A \sin(\varphi_0 + \alpha)$) and will not influence the magnitude image. Phase Encode effect depends on the fractional part of generator frequency, the aberrational field strength (at the tumor boundaries), applied current, conductivity ratio, and initial contrast.

Phase Encode effect for other than sequential phase encode modes and image acquisition modes is considered in Section 9.1.

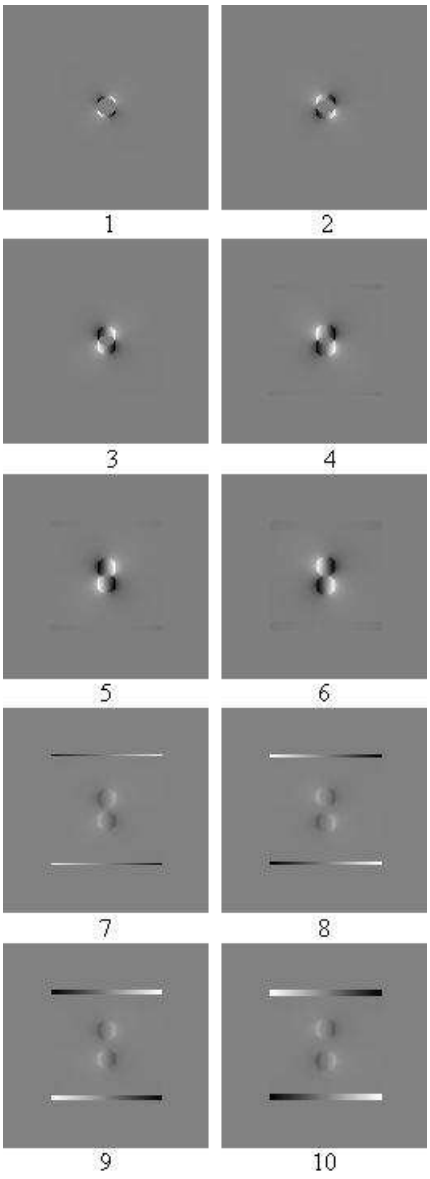

Figure 43.: Phase Encode effect in simulated difference images acquired with current on and off for the higher conducting disk ($\sigma_{ratio} = 20$) with radius of $R = 5$ mm, current density $i = 10$ A/m^2, frequency resolution $df = 60$ Hz/pix, $N_p = 128$, and $TR = 2$ s. The fractional part generator frequency $\{f\}$ was varied to produce the shift $\Delta y_{pix} = \{f\} \cdot TR \cdot N_p = 1, 2, ..., 10$ pixels (Δy_{pix} is given below each image).

Chapter 7
Experiment: Development and Results

This Chapter describes the experimental developments and testing aimed to validate the MREIM theory. A novel breast phantom suitable for measuring both magnetic resonance and electrical impedance properties of the breast was designed and developed. Several other issues were addressed: Faraday Shields (FSs) design, FSs-phantom coupling, as well as the choice of MR suitable sequence. Although based on off-the-shelf equipment, we were able to show that MREIM is capable of producing a detectable signal differentiating materials with higher conductivity (Heine, Kovalchuk et al. 2008b).

7.1 Breast Phantom Development

The most common materials used in MRI phantom construction to date have included paramagnetic solutions, agar gels, and oils (Madsen and Fullerton 1982; Kraft, Fatouros et al. 1987; Liney, Tozer et al. 1999). Different types of conduction phantoms were developed using materials with magnetic resonance and conductivity properties equivalent to normal breast tissues and tumors. Specifically, materials simulating healthy breast fatty tissue should have $T1$ and $T2$ relaxation times around 372 ms and 53 ms, respectively (Rakow-Penner, Daniel et al. 2006) and electrical conductivity in the range of 0.02–0.07 S/m at frequency of 1 kHz (Gabriel 1996; Jossinet 1998; Scholz and Anderson 2000). Materials simulating breast tumors or glandular tissue should have $T1$ and $T2$ relaxation times around 1136 ms and 58 ms, respectively, with breast tumors having electrical conductivity 3–40 times higher than that of healthy breast tissue (Chapter 3).

Initially, fragrance free Neutrogena soap was selected as the material equivalent to healthy breast tissue. The soap electrical conductivity was measured to be 0.03 S/m at 1 kHz. Two types of phantoms were constructed with the soap: (a) soap phantom that contained a

spherical cavity in the center of 1 cm in diameter filled with a soap/salt solution ($\sigma = 1.2$ S/m) and (b) soap phantom with the spherical cavity filled with a piece of fat-free hot dog (Oscar Mayer, Fat Free Wieners) ($\sigma = 2.17$ S/m). A photograph of phantom (b) is shown in Fig. 44.

Figure 44.: Sliced MREIM phantom constructed of fragrance free Neutrogena soap showing the spherical piece of fat-free hotdog of 1 cm in diameter (cancer surrogate).

The imaging results showed that the soap phantom with the soap and salt spherical insert was unstable and prone to diffusion (Fig. 45). The phantoms were made a few hours before the imaging to eliminate the diffusion of the salt into the surrounding soap.

The third type of phantom was constructed using agar gel as a pliable material equivalent to healthy breast tissue and a piece of fat-free hotdog as a cancer surrogate. The agar solution (1.4 g/100 mL) was placed in an electrically conductive (2000 Ω measured for 0.1 thickness and area of 1 cm^2) 6×10 in^2 flat poly bag (Associated Bag Co.) that represented a skin surrogate. The calculated resistivity for this carbon plastic was $\rho_c = 2 \times 10^5$ Ω·cm. The bag had the similar resistive properties and thickness to human skin (Lee, Kim et al. 2002). A photograph of the agar phantom placed in the carbon poly bag is shown in Fig. 46.

The conductivity cell was constructed from PVC pipe ($D = 1$ in and $l = 1$ in) and 2 stainless steel sheets to measure the conductivity of the agar solution. Hot agar solution was

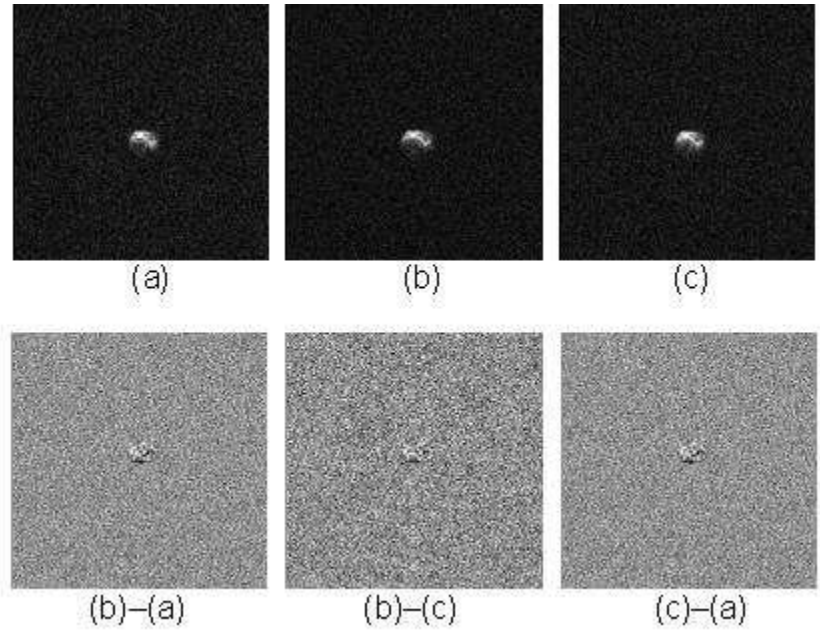

Figure 45.: Echo Planar Imaging Sequence images (transversal view) of a soap phantom with a soap and salt solution as a cancer surrogate. The images were acquired with (a) current off, (b) current on, and (c) current off. Subtraction image of two controls, (c)-(a), showed the presence of difference signal, which was probably due to diffusion of the soap and salt insert into surrounding soap medium.

Figure 46.: MREIM phantom made of agar gel in a conductive carbon bag.

poured into the cell ensuring that no air bubbles were left inside. When the solution cooled and solidified, the voltage and applied current passing through the cell were measured. From the definition, the electrical conductivity, $\sigma = \frac{l}{A} \cdot \frac{1}{R}$. Implying that $A = \frac{\pi \cdot D^2}{4}$ and $l = D = 1$ in, the conductivity was calculated from the formula $\sigma = \frac{4}{\pi \cdot D \cdot R} = \frac{50}{R}$, where the resistance R was found from the Ohm's law. The conductivity of the agar solution was measured to be 0.095 S/m, and the conductivity of the hotdog was 2.17 S/m. The circuit diagram for conductivity measurements is displayed in Fig. 47.

Furthermore, conductivity dependence on the frequency was investigated (Fig. 48) showing a steady behavior of conductivity with frequency change.

The agar phantom proved to be more stable and showed consistency in the imaging results. It simulated the magnetic resonance and electric properties of normal and malignant breast tissue and was cost effective and easy to replicate. It was made fresh before each imaging experiment.

Various sequences were tested for three phantoms, e.g., SDSE, EPI SE, T2flash, etc. A choice of SDSE sequence was motivated by its simplicity in terms of MREIM theoretical and simulation developments. Due to the problems with soap phantom designs (Fig. 45) the agar phantom was used for further MREIM testing.

7.2 MREIM Apparatus

The experimental set-up included the following: (1) Magnetic Resonance System, (2) Faraday Shields, and (3) MREIM components to supply electric current to the breast phantom.

7.2.1 Magnetic Resonance System

A Siemens Magnetom Symphony Maestro Class 1.5 T system (Siemens Medical Solutions USA, Inc., Malvern, PA) was used for all experiments in this study (Fig. 49). The system was equipped with a Siemens 1.5 T Symphony 7 Channel Biopsy Breast Array provided by Invivo Corp. (Orlando, FL). Figure 50 shows the Breast Array with a breast phantom placed within stabilization paddles.

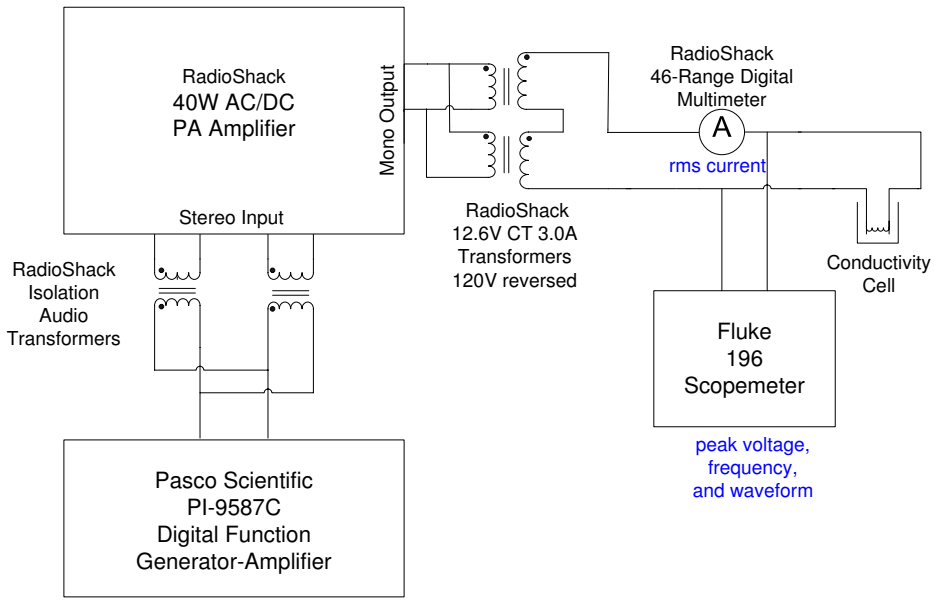

Figure 47.: A circuit diagram employing a custom made conductivity cell used for conductivity measurements.

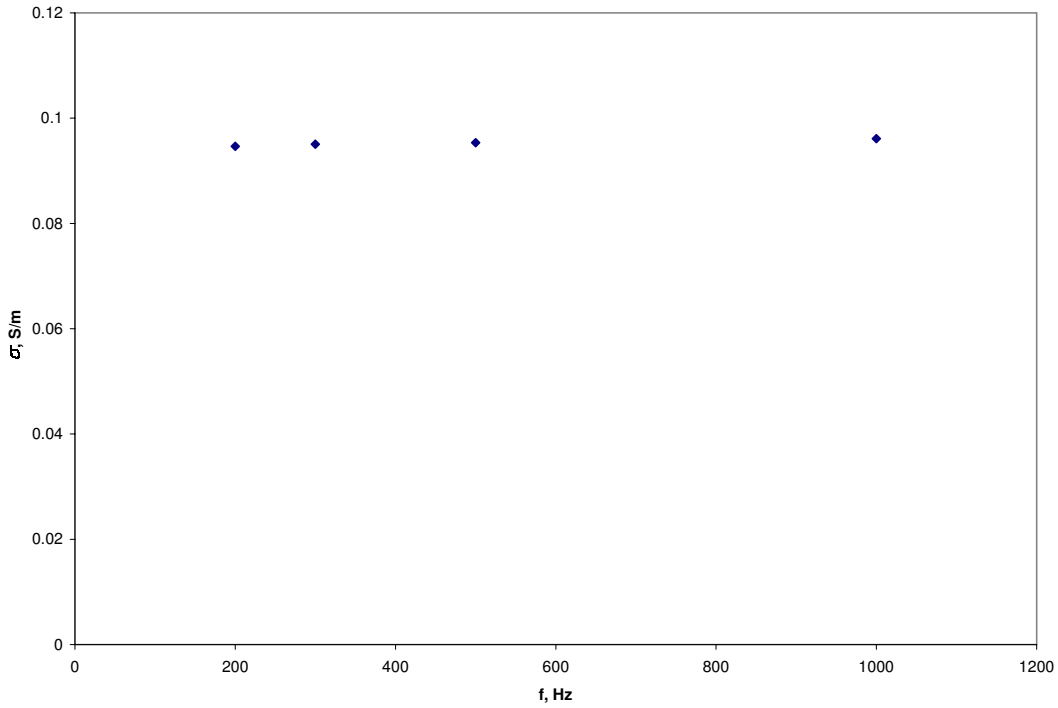

Figure 48.: Agar solution conductivity dependence on generator frequency.

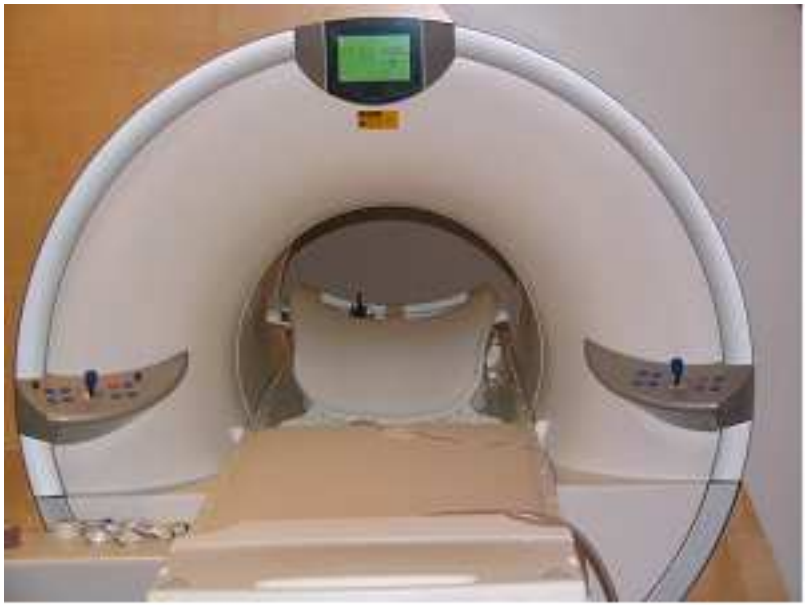

Figure 49.: A Siemens Magnetom Symphony Maestro Class 1.5 T system (Siemens Medical Solutions USA, Inc., Malvern, PA) used for the imaging experiments.

7.2.2 Faraday Shields

The Faraday-shield electrodes were attached to the breast array stabilization/compression paddles to produce a current flux in the breast orthogonal to the main H_0 magnetic field (Fig. 51). The Faraday shields were constructed of a pair of copper sheets that were machined to form a comb-like array of parallel slots. Two different sizes of copper foil sheets were tested for a soap phantom and agar phantom, respectively: (a) with dimensions of 5 cm $\times$ 7.5 cm consisting of comb fingers that were 0.32 cm in width with 0.016 cm spacing between them and (b) one with dimensions of 14 cm $\times$ 15 cm consisting of bars that were 0.2 cm in width with 0.1 cm spacing between them (Electron Machine Corp., Umatilla, FL).

Although the MREIM apparatus was designed for phantom testing, it was also important to explore the problem of the patient-FSs coupling that would separate the skin from the metal electrodes to satisfy requirements of clinical use and regulatory agency approval. From Eq. (6.54), lower frequencies will produce a more observable effect. To chose the frequency range for experimental testing, frequencies used for impedance-based imaging techniques were considered. The TransScan 2000's operational frequency is 200 Hz. At this frequency

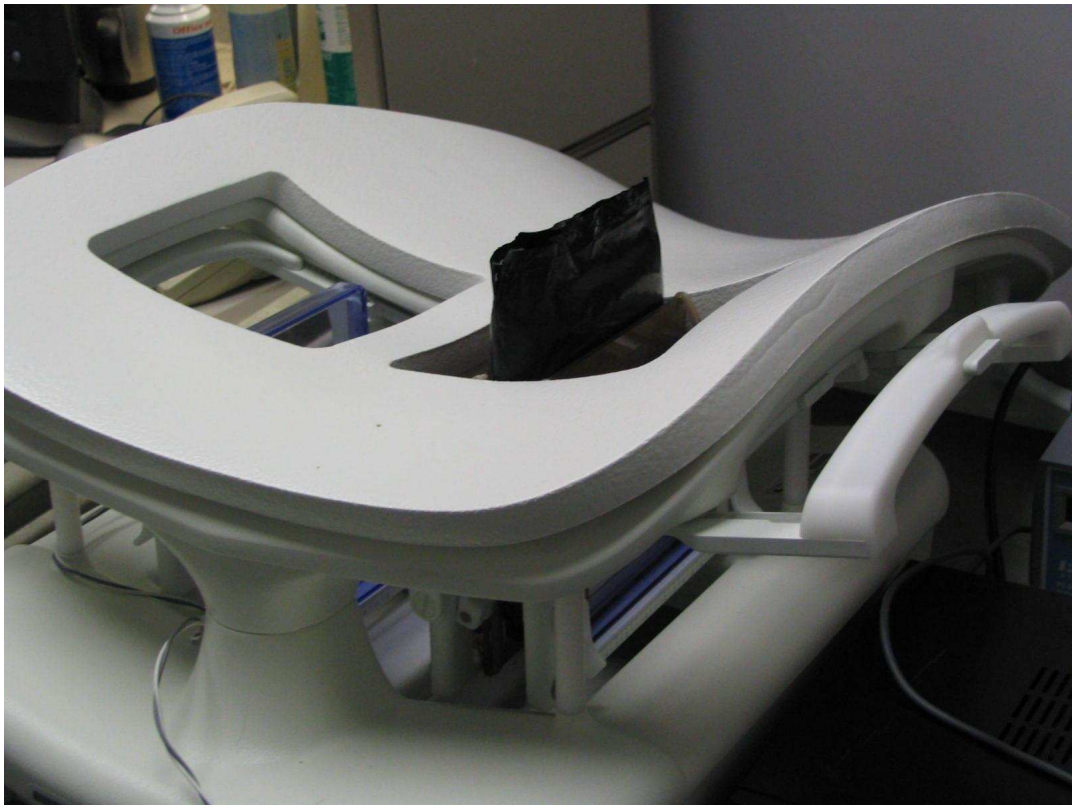

Figure 50.: A Siemens 1.5 T Symphony 7 Channel Biopsy Breast Array provided by Invivo Corp. (Orlando, FL) with the stabilization paddles modified to include the Faraday shield electrodes.

Figure 51.: Stabilization/compression paddles of the MR breast coil. The left paddle of the coil was modified to include a Faraday shield made of a pair of copper sheets consisting of rectangular parallel bars. The copper sheets shown here had dimensions of 14×15 cm^2. The phantoms were positioned between the two plates for imaging.

range, a capacitive coupling method would not be feasible. Likewise, the required inductive impedance matching and the cost to develop the capacitive coupling elements would present problems. Conductive coupling was considered instead. A search for a conductive coupling elements resulted in the choice of conductive vinyl (Desco Statfree CV$^{\text{TM}}$) sized to the stabilization paddles with the dimensions of $15 \times 14 \times 0.3$ cm^3. The resistance of a 3 mm thick piece of the vinyl plastic with area of 1 cm^2 was measured as 10,000 Ω, which resulted in the resistivity $\rho_v = 3.33 \times 10^4$ Ω·cm. It should be emphasized that this represents a "low-tech" inexpensive solution to an important aspect of the study. The vinyl plates also serve another purpose by offering significant resistance in series with the breast load. The voltage drop across the vinyl plates limits the short circuit current across the breast (or in this case, the agar-hotdog phantom), which is an important consideration (Heine, Kovalchuk et al. 2008b).

The resistance of each component in Fig. 122 (b) can be estimated by making an approximation for the FSs-phantom contact area and geometry of the phantom. The contact area was estimated as 100 cm^2 with a variation of ± 1 cm in both length and height, which

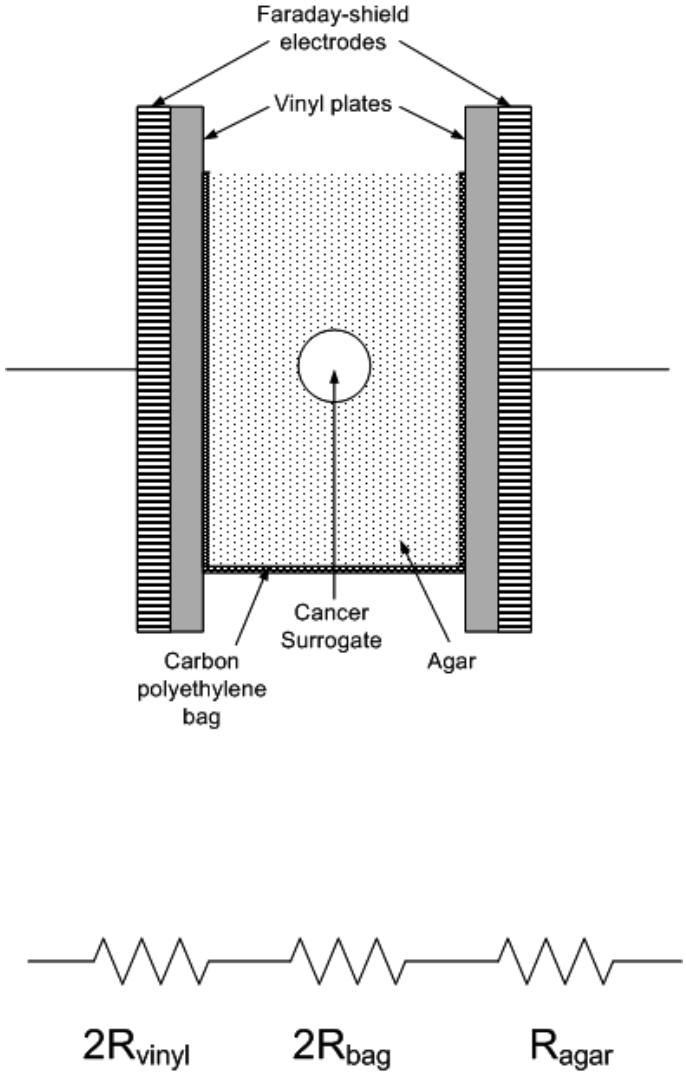

Figure 52.: (a) A diagram of of the loaded FSs and (b) its equivalent series circuit.

gives a contact range of (81–121) cm^2, and the phantom width was approximately 5 cm. Thus, the resistance of one vinyl plate is $R_v = 3.33 \times 10^4 \times (0.3/100) = 100\ \Omega$. Since the resistivity is much higher for the carbon-plastic in relation to the vinyl, we make an approximation that the conduction through the carbon-plastic takes place along the contact area and is orthogonal to the vinyl/carbon-plastic contact region, which treats the carbon bag as a sheet similar to the vinyl plate. Thus, the resistance for one carbon sheet is $R_c = 2 \times 10^5 \times (0.01/100) = 20\ \Omega$. Making the approximation that the tumor surrogate occupies a small volume relative to the agar gel volume, the resistance due to the breast phantom is $R_{agar} = 1.05 \times 10^3 \times (5/100) = 52.5\ \Omega$. Thus, the total resistance of the loaded FSs is given by $R_T = 2R_v + 2R_c + R_{agar} = 292.5\ \Omega$. The voltage drop across the actual phantom was approximately 20 volts, which creates an electric field of about 4 V/cm. The electric field strength is on the order of field strengths used in other experimental clinical trials research for disrupting cancer cell differentiation (Miller 2007).

7.2.3 Current Providing MREIM Components

The circuitry designed to supply electric current to the phantom included the following: Pasco Scientific PI-9587C Digital Function Generator-Amplifier, RadioShack 40W AC/DC PA Amplifier, 46-Range Digital Multi-meter, Fluke 196 Scope-meter, coaxial MR compatible cables and RF trap (InVivo Corp.), a set of RadioShack transformers, chokes, and attenuators (Fig. 123). Pasco Scientific PI-9587C Digital Function Generator-Amplifier resolves to 0.001 Hz, and its accuracy is $0.01\% \pm 1$ digit. This consideration is important since generator frequency is required to be fractional (at $TR = 2$ s) to produce PE effect. The total current density through the agar phantom was in the range of [10–17] A/m^2 at frequencies in the range of [200–350] Hz. The scope-meter was turned off before each imaging acquisition. Three images were acquired for each experiment with: current off, current on, and current off.

Figure 53 shows a diagram of the electric circuit used to supply the electric current to the phantom through the conductively coupled FSs.

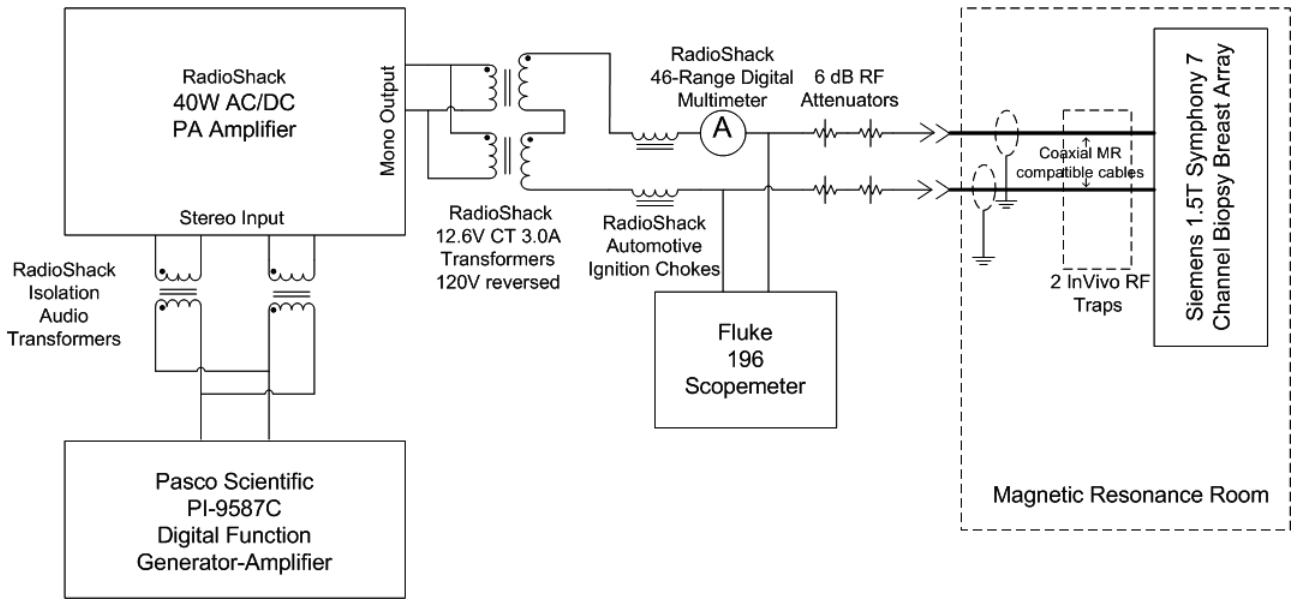

Figure 53.: A diagram of the experimental set up used to supply the electric field to the phantom which was placed between the modified stabilization plates of the breast coil.

7.3 Imaging Sequence and Slice Orientation

Spin Density Spin Echo Sequence was chosen as a basic sequence to prove MREIM feasibility. The SDSE parameters for imaging agar phantom were set to $TR = 2000$ ms, $TE = 50$ ms, frequency resolution $df = 60$ Hz/pix, slice thickness $= 4$ mm, and $FOV = 128$ mm. Long TR choice was motivated by the SDSE requirements to suppress native contrast by minimizing $T1$ effect (see Table 9). In sagittal slices, 128×128 image matrix pixels with 1.0×1.0 mm pixel dimension were used. All slices were acquired parallel to x, y-plane (Fig. 54). With a number of averages set to 1, the scan time for each image was approximately 5 min.

7.4 Experimental Results and Discussion

The agar phantom demonstrated qualitative similarity to breast tissue in MRI appearance, realistically reproducing malignancy and normal breast tissue in terms of relative signal intensity. The experiments discussed below were performed on different dates with different replicas (same recipe) of the breast phantom. The comparisons and differential signals were

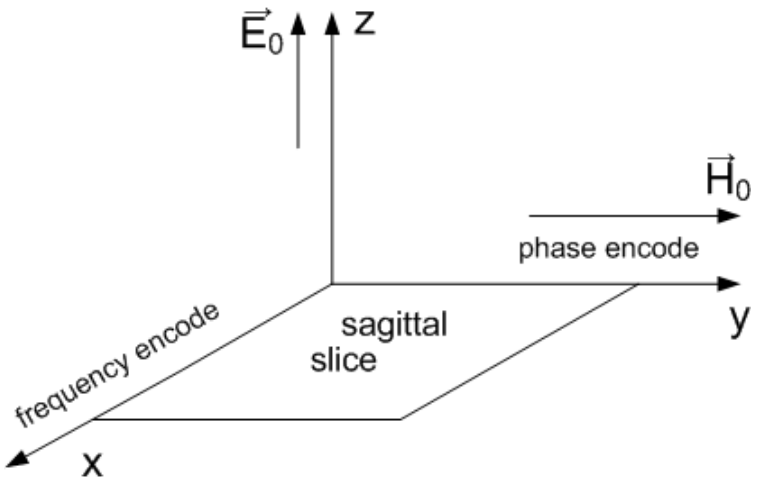

Figure 54.: The images were acquired in sagittal, x, y-plane, with the main magnetic field and PE gradient directed along the y axis and FE gradient directed along the x axis. Note, axis are non-standard for MRI.

determined using the magnitude data because the complex phase data is proprietary and was not accessible during the course of this feasibility study.

The $T1$ and $T2$ relaxation parameters were not measured explicitly but were deemed appropriate by visual observation. The strong background signal from the agar on $T1$ weighted FLASH localizer images (scout images - not shown) and moderate signal on the SDSE images (see Figs. 55–58) simulated a fatty breast, and the low signal from the cancer surrogate on $T1$ weighted FLASH and higher signal on SDSE simulated a malignancy. Likewise, the $T2$ of the background may be estimated because of the long TR used in the experimental sequences (as described below). Therefore, the MRI relaxation parameters were visually within the range of the expected.

With *df* set to 60 Hz/pix, current density ranging from 10 to 17 A/m^2, and frequencies varying from 300 to 350 Hz, the difference images with current off and on (Figs. 55–57) (b)-(a) and (b)-(c), show the effect of the perturbation around the cancer surrogate. The expected signal was not observed when *df* was set to 22 Hz/pix and f was set to 200 Hz (Fig. 58).

The top row images in Fig. 55 show that the cancer surrogate has acceptable contrast relative to the background, and the shields are not perceptible and do not degrade the MR image acquisition. This is an indication that the FSs are compatible with the MR coil, and that the phantom and MREIM equipment are compatible with MR system.

Slight interference patterns are apparent in the images in Fig. 56, which were probably due to radio frequency leakage into to the FSs electrical leads due to poor shielding. The RF leakage is not present in other experiments where the current density is lower. Also, the MREIM effect is less apparent than in Fig. 55, even though the current density is higher here. This can possibly explained by the influence of noise.

Figure 57 shows the images acquired with the following parameters: $i = 10$ A/m^2 at $f \approx 350$ Hz, $df = 60Hz/pix$. Noise is greater than in Fig. 55.

The missing effect in Fig. 58 is predicted by the supporting theory due to the interplay of the frequency resolution *df*, signal generator frequency f, and radius ($\Delta x = \frac{f}{df} dx \approx 2R$) influenced by noise.

In conclusion, a custom designed and developed MREIM apparatus was able to validate

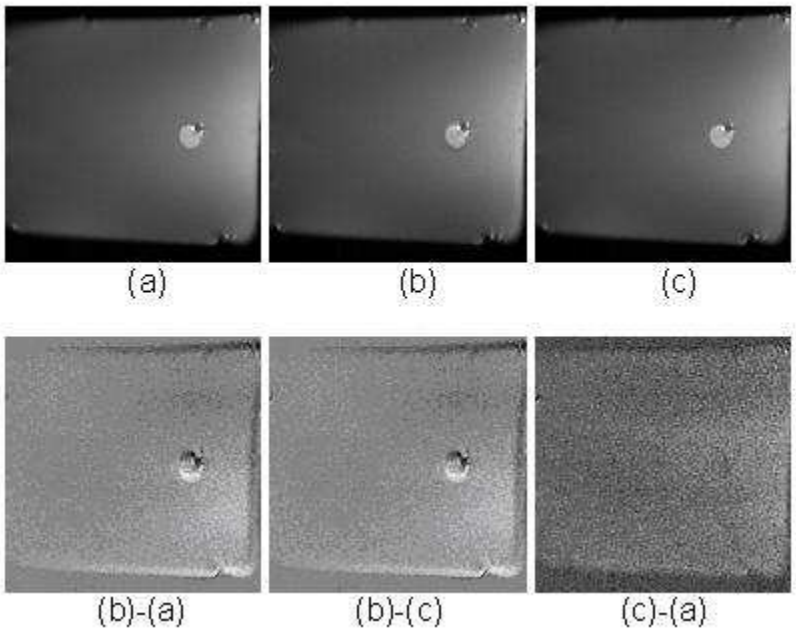

Figure 55.: Agar phantom images (sagittal view) acquired with an SDSE sequence with the generator frequency set to $df = 60$ Hz/pix. Images of the phantom with (a) current off, (b) current on ($i = 10$ A/m^2 at $f \approx 300$ Hz), and (c) current off. The first two difference images in each set, i.e., (b)-(a) and (b)-(c), show the effect of the perturbation around the cancer surrogate. This effect is not observed when the two "current off" images are subtracted, (c)-(a).

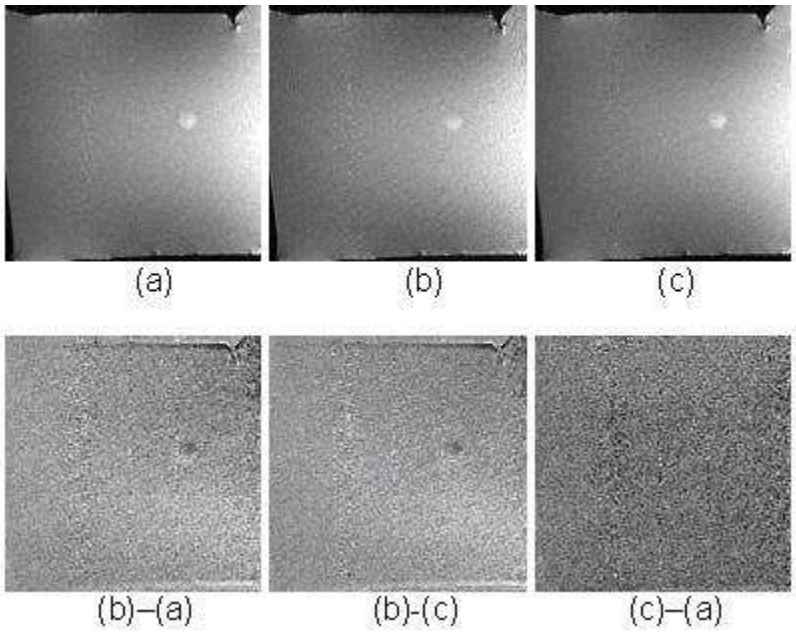

Figure 56.: Identical image setup as in Fig. 55. The MREIM parameters were changed to $i = 17$ A/m^2 at $f \approx 300$ Hz, $df = 60$ Hz/pix.

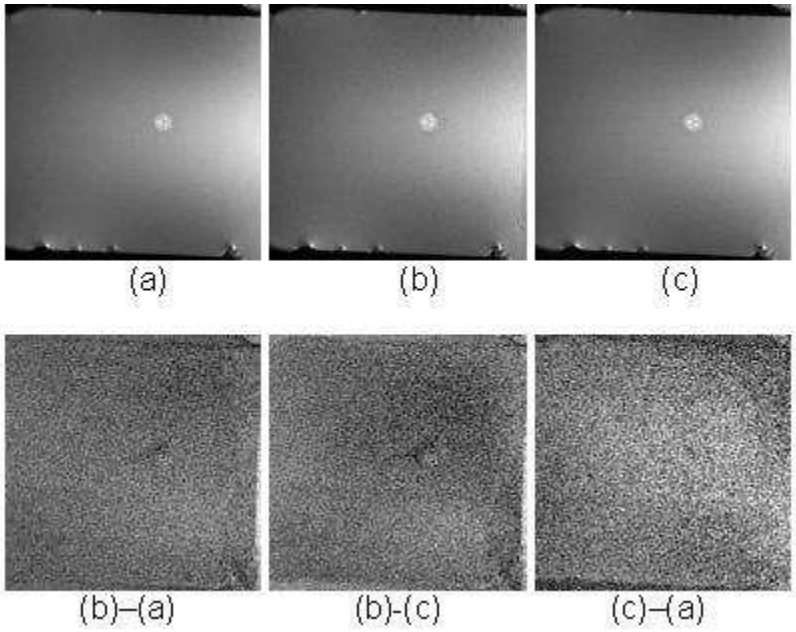

Figure 57.: Identical image setup as in Fig. 55. The MREIM parameters were changed to $i = 10$ A/m^2 at $f \approx 350$ Hz, $df = 60$ Hz/pix.

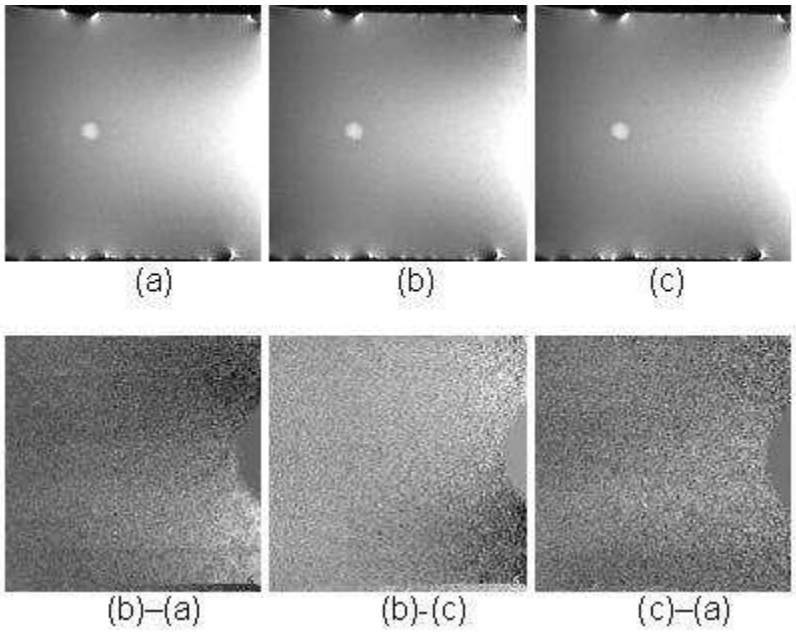

Figure 58.: Identical image setup as in Fig. 55. The MREIM parameters were changed to $i = 10$ A/m^2 at $f \approx 200$ Hz, $df = 22$ Hz/pix. No effect is observed in the subtraction images.

the MREIM theory producing the images with a differential signature of a higher conducting region. It must be noted that although the developed experimental set-up was sufficient to show the validity of MREIM theoretical development, a more thorough design and government approved vendor manufacturing are required for MREIM to be clinically tested in future. The experimental findings are replicated and further explained by simulations (Section 8.2.1).

Chapter 8

Simulation: Development and Results

This Chapter provides the simulation study aimed to investigate the effects of the applied electric field on the native MREIM image formation. The MREIM simulation is based on a simple SDSE sequence, and Heine's Master's Thesis "Computer Simulations of Magnetic Resonance Imaging and Spectroscopy" (Heine 1993) served as a basis for simulation development. Simulations are performed in the Interface Description Language (IDL) for both an idealized model of a spherical higher conductive lesion embedded in a lower conducting region using the analytical expression for aberrational magnetic fields (Eq. (6.34)) and for a model of more realistic breast tumors with irregular boundaries and anisotropic conductivity using the numerical solutions for aberrational magnetic fields (Eq. (6.49)). MREIM utilizes Eqs. (6.58) and (6.65) to implement the aberration to the native MR image acquisition process. Simulations were performed in part to understand the experimental results. A method of measuring contrast-to-noise ratio (CNR) and detectability is developed to quantitatively describe the MREIM effect observability. Based on detectability measurements, the two effects are investigated in terms of their dependence on MREIM parameters.

8.1 Simulation Development

This Section provides the MREIM simulation algorithm, the algorithm for calculation of electric potential and aberrational magnetic fields for irregular tumor shapes and anisotropic conductivities, and the method developed to quantitatively analyze the MREIM effect in terms of its physical perception.

8.1.1 MREIM Simulation Algorithm

Figure 59 shows a block diagram representing the MREIM simulation algorithm. The algorithm of the simulation consisted of the following steps:

Step 1: Input of Parameters. The following parameters were constant in MREIM simulation:

- N - number of PE and FE steps:

- phase encode gradient strength incrementation p and time incrementation t, $N = N_p = N_t = 128$;

- spatial x and y incrementation k, $L = 4 \cdot N = 512$;

- FOV - Field of View and dx - pixel resolution:

- $dx = 1$ mm, which for 128 pixels has fixed the field of view, $FOV = N \cdot dx = 12.8$ cm;

- $TR = 2000$ ms - repetition time;

- $TE = 50$ ms - echo time;

- $G_{x_{max}} = 22$ mT/m – maximum PE gradient strength.

- Phase Encode step can be found as $\Delta G_y = \frac{2G_{x_{max}}}{N_p - 1}$. Time of PE gradient application is linked to the PE gradient strength as $\tau = \frac{1}{\gamma \cdot \Delta G_y \cdot fov}$.

Variable parameters:

- f - signal generator driving frequency. Generator driving frequency was varied over the range of 20–1000 Hz considering the following constraints:

- suggested frequency from the TransScan TS-2000 performance (200 Hz),

- low frequency range due to the use of real component of conductivity (α region),

- use of conductive coupling for the phantom-FSs system,

- from Eqs. (6.58) and (6.65), it follows that the aberrational term is larger at lower generator frequencies.

  To observe the shift due to PE effect at $TR = 2$ s, the generator frequency is required to be fractional, $\Delta y_{pix} = \{f\} \cdot TR \cdot N_p$ (see Section 6.2.2). Generator frequency was linked to frequency resolution *df* to obtain the shift due to FE effect, $\Delta x_{pix} = \frac{f}{df}$;

- **objective:** to investigate generator frequency influence on producing the most conspicuous MREIM effect for SDSE sequence for the parameters specified above;

• *df* - frequency resolution (bandwidth per pixel):

- *df* was varied to optimize the FE and PE effects. Frequency resolution is proportional to frequency gradient strength, $df = \gamma G_x dx$, and inversely proportional to signal-to-noise ratio (SNR). Since we are interested in both stronger perturbation of native MR image (at weaker encode gradients) and high signal-to-noise ratio, *df* is preferred to be in a lower range.

- **objective:** to determine the frequency resolution at which the MREIM is the most conspicuous for the specified parameters;

• i - applied current density:

- experimental values: 100–170 mA for the contact area of 10×10 cm^2, which is equivalent to 10–17 A/m^2;

- **objective:** to determine the minimum value of applied current for the minimum MRM detectable tumor ($R = 1.5$ mm) with the borderline conductivity ratio ($\sigma_{ratio} = 3$);

• R - radius of spherical tumor:

- radius of a cancer surrogate in the breast phantom was $R = 5$ mm, which was used as default for MREIM effect study;

- $R = 2.5$ mm and $R = 1.5$ mm were used to find the minimum applied currents for MREIM effect detectability;

- *contrast* - initial contrast between the higher conducting and lower conducting medium: $contrast = \frac{S_{in}-S_{out}}{S_{out}} \cdot 100\%$, where S_{in} and S_{out} are the pixel intensities inside and outside the higher conducting region, respectively:

- based on experimental images, *contrast* between the tumor surrogate and surrounding agar medium was approximately 10%.

- **objective:** to investigate MREIM signal detectability dependence on initial tumor *contrast*.

Step 2: Template Image Generation.

The template image for a simple tumor model of a higher conducting sphere embedded in a lower conducting homogenous medium was generated for the 2-D slice at $z = 0$, with the higher conductive disk (assuming slice thickness) in the center. The values for pixel intensities inside and outside the sphere, S_{in} and S_{out}, were assigned based on the experimental results to produce $contrast = 10\%$. Random Gaussian noise with zero mean and standard deviation $\sigma_{SD} = 2$ (by default) was added to the template image intensity image to make the simulation realistic.

Step 3: Three Loops.

The realization of Eq. (6.54) is performed through the iteration over three variables: p - phase incrementation, t - time incrementation, and k - space incrementation. For each discrete value of PE gradient and time, the signal in x, y plane is presented as the sum over the spatial incremented x and y.

Step 4: Calculation of Aberrational Magnetic Field.

For a simple tumor model of a higher conducting spherical tumor embedded into lower conducting medium, the aberrational magnetic field is calculated according to analytical expressions in Eq. (6.34) for each coordinate x and y, with $z = 0$. The image mask is used to distinguish the regions inside and outside the disk.

For a realistic model of a breast with various tumor shapes and anisotropic conductivity, the numerical solution to aberrational magnetic field (Eq. (6.49)) were incorporated. An algorithm for the numerical field solutions is provided in the following Section.

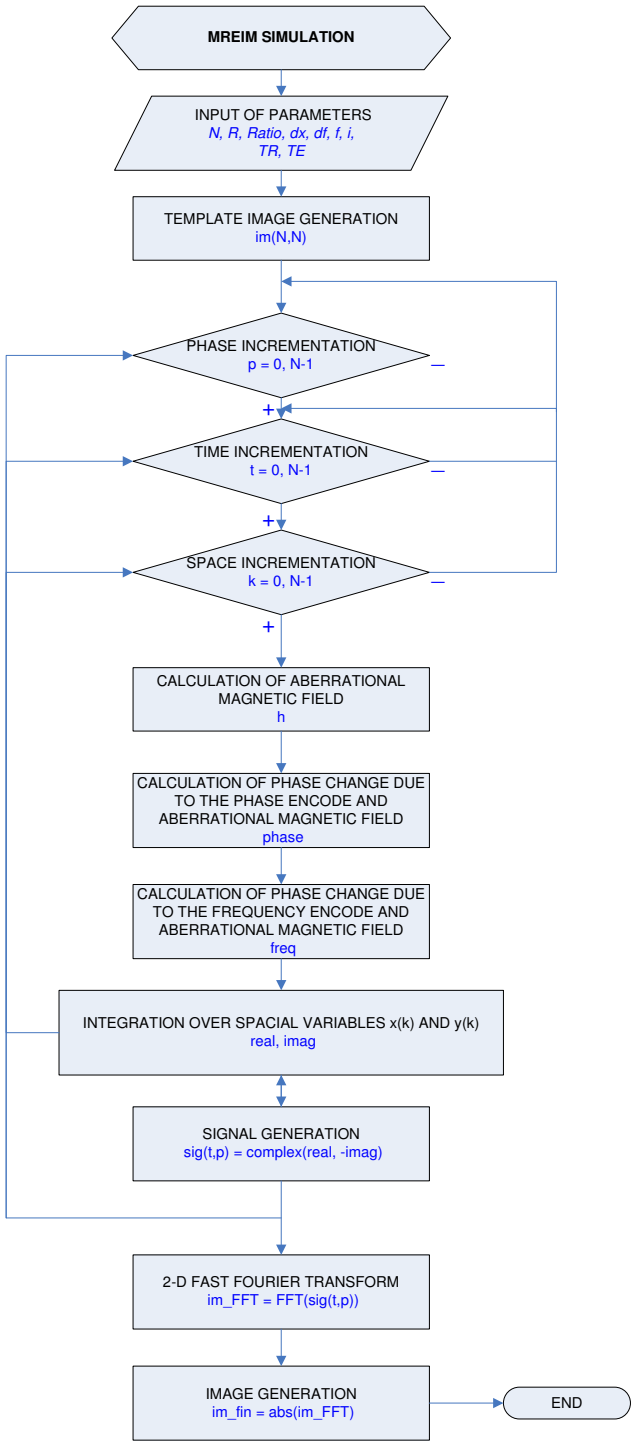

Figure 59.: A block diagram for MREIM simulation.

Step 5: Calculation of the Phase Change due to the PE Gradient and Aberrational Magnetic Field Perturbation in PE.

The phase change consists of three terms: the unperturbed image and two aberrational terms from Eqs. (6.70) and (6.71) scaled by the factor containing the aberrational magnetic field.

Step 6: Calculation of the Phase Change due to the FE Gradient and Aberrational Magnetic Field Perturbation in FE.

The phase change consists of three terms (Eq. (6.58): the native image and the perturbational terms proportional to the aberrational magnetic field.

Step 7: Calculation of the Signal's Real and Imaginary Parts for Every p and t Value.

Formation of the matrix $sig(t, p)$ based on the summation over the spatial x and y components. The phase is separated into real and imaginary components. The real and imaginary parts are multiplied by the template image.

Step 8: Application of 2-D Fast Fourier Transform to the Signal.

Step 9: Taking the Magnitude of the Raw Image to Obtain the Final Result.

8.1.2 Numerical Calculation of MREIM Fields

The algorithm for numerical solution for electrical potential from Eq. (6.48) is shown in Fig. 60. The magnetic field was computed from Eq. (6.49) following the same procedure with specific boundary conditions:

$$\begin{aligned} V(x, y, 0) &= -E_0 z(0) \\ V(x, y, N-1) &= -E_0 z(N-1) \\ V(0, y, k) &= -E_0 z(k) \\ V(N-1, y, k) &= -E_0 z(k) \\ V(x, 0, k) &= -E_0 z(k) \\ V(x, N-1, k) &= -E_0 z(k), \end{aligned} \tag{8.1}$$

where $E_0 = i/\sigma_{normal}$ is a steady-state electric field strength. With an assumption that conductivity is homogenous on the periphery of the cuboid, the boundary conditions for

y-component of magnetic field were set according to the far field term in Eq. (6.34)

$$\begin{aligned} H(0,y,z) &= \tfrac{1}{2}\sigma_{normal}E_0x(0) \\ H(N-1,y,z) &= \tfrac{1}{2}\sigma_{normal}E_0x(N-1) \\ H(i,0,z) &= \tfrac{1}{2}\sigma_{normal}E_0x(i) \\ H(i,N-1,z) &= \tfrac{1}{2}\sigma_{normal}E_0x(i) \\ H(i,y,0) &= \tfrac{1}{2}\sigma_{normal}E_0x(i) \\ H(i,y,N-1) &= \tfrac{1}{2}\sigma_{normal}E_0x(i), \end{aligned} \tag{8.2}$$

where σ_{normal} is the conductivity of healthy breast tissue.

For a given conductivity profile, the solution was divided into two part: (1) electric potential distribution (Eq. (6.48)) and (2) the y-component of magnetic field strength (Eq. (6.49)). The tolerance (accepted precision) was 10^{-4} and 10^{-6} for electric potential and magnetic field strength with the maximum iteration number of 10^3. Equation (8.3) displays the format used for iterations:

$$V_{i,j,k} = (1-\omega)\, V_{i,j,k}^{old} + \omega V_{i,j,k}, \tag{8.3}$$

where ω is a convergence factor. Equation (8.3) denotes the Successive Over-Relaxation (SOR) method if $\omega > 1$. In accordance to Kahan theorem (Kahan 1958), the system of equations is convergent when ω is in the open range of $(0;2)$. When $\omega = 1$, the SOR method simplifies to the Gauss-Seidel iteration method, where for a given iteration the elements that have already been computed for this iteration are used. For each iteration in i,j,k, the difference between the old and new value of $V_{i,j,k}$ is checked; the maximum difference for a given iteration is called the error. If the error is less than pre-assigned tolerance value, the iteration is stopped and the converged solution for V is considered as the solution to the first part of the problem. The "price" for the given solution is represented by the number of iterations performed.

Plots of maximum iteration error versus the number of iterations for V are shown in Figs. 61 and 62, and for H shown in Fig. 63.

To decrease the "price" for a converged solution, the choice of ω was estimated by the formula (Mitra 2007):

$$\omega = \frac{4}{2+\sqrt{9-\left(3\cos\left(\frac{\pi}{N-1}\right)\right)^2}}, \tag{8.4}$$

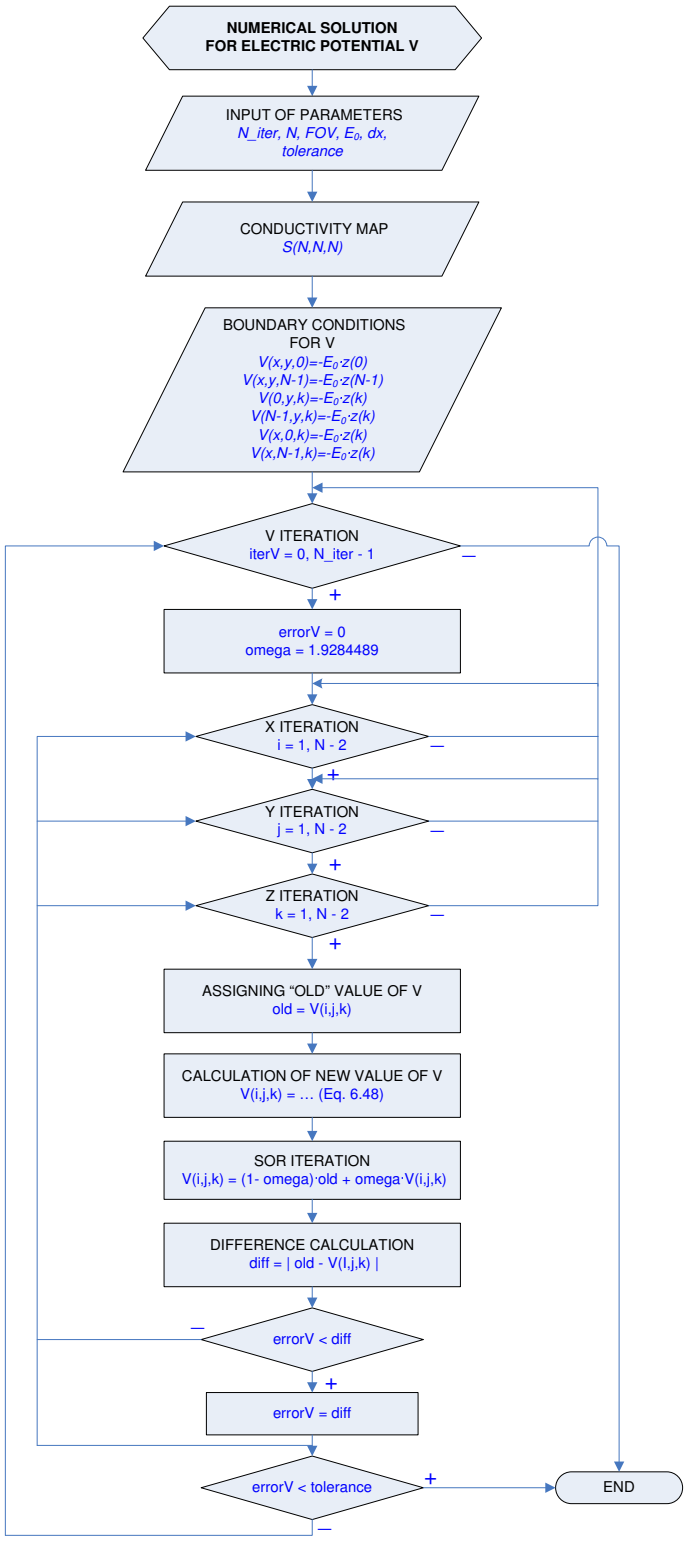

Figure 60.: An algorithm for numerical solution for electric potential using FDM.

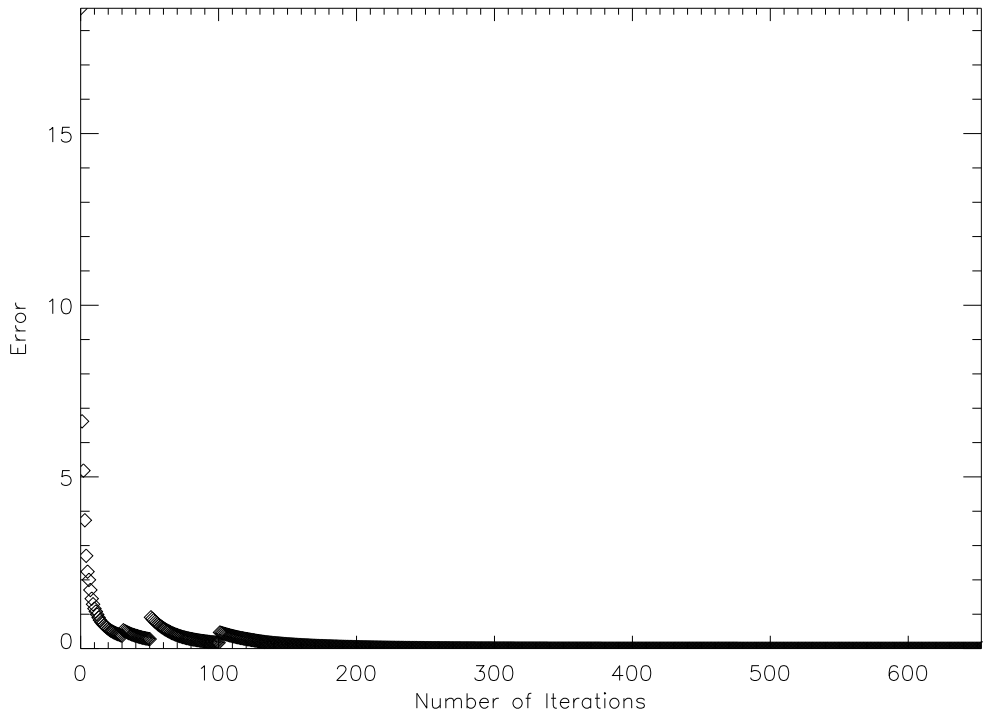

Figure 61.: Maximum error in V for each iteration versus number of iterations for SOR scheme: if $iter > 30$ then $\omega = 1.2$ if $iter > 50$ then $\omega = 1.7$ if $iter > 100$ then $\omega = 1.9$. The total number of iterations to reach tolerance 10^{-4} was 653.

which in case of $N = 128$ is equal to 1.9284489. The error plot for $\omega = 1.9284489$ is shown in Fig. 62.

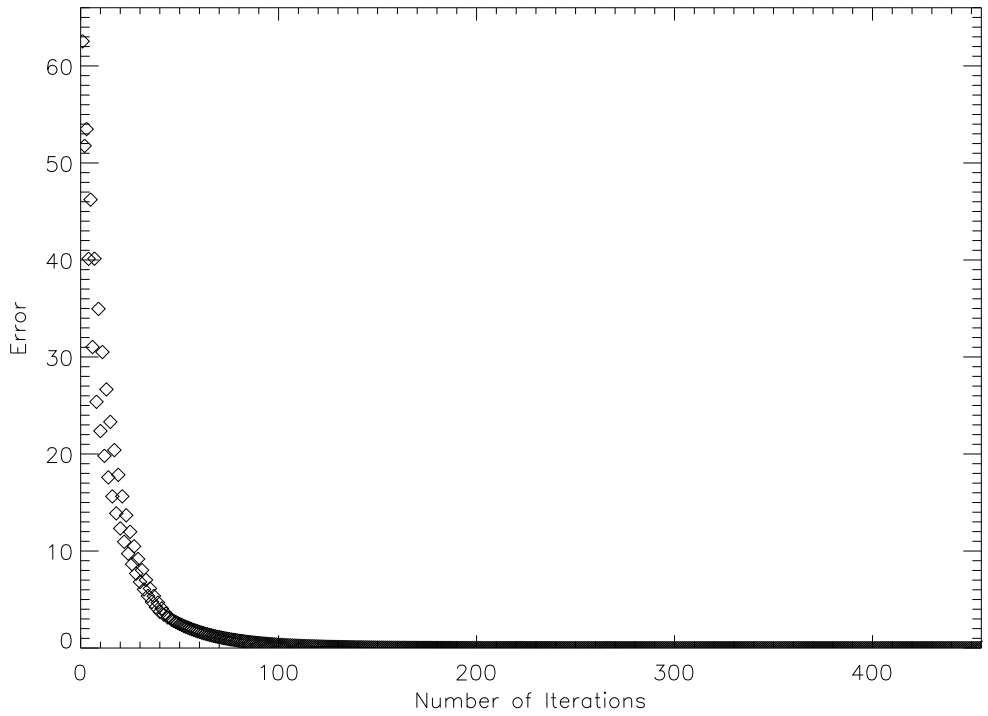

Figure 62.: Maximum error in $\omega = 1.9284489$ for each iteration versus number of iterations for $\omega = 1.9284489$. The total number of iterations to reach tolerance 10^{-4} was 455.

8.1.3 Contrast Measurements

Contrast-to-noise ratio and detectability d were chosen as figures of merit. Contrast-to-noise ratio was calculated with Eq. (8.5) (Beutel, Kundel et al. 2000):

$$CNR = \frac{\left|\bar{S}_{sig} - \bar{S}_{bg}\right|}{\sqrt{\frac{1}{2}\sigma_{sig}^2 + \frac{1}{2}\sigma_{bg}^2}}, \tag{8.5}$$

where $\bar{S}_{sig}$, $\bar{S}_{bg}$ and σ_{sig}, σ_{bg} are the mean pixel intensities and their standard deviations for object and background, respectively. Detectability was computed with Rose's formula (Rose 1948):

$$d = CNR \cdot \sqrt{N_{pix}}, \tag{8.6}$$

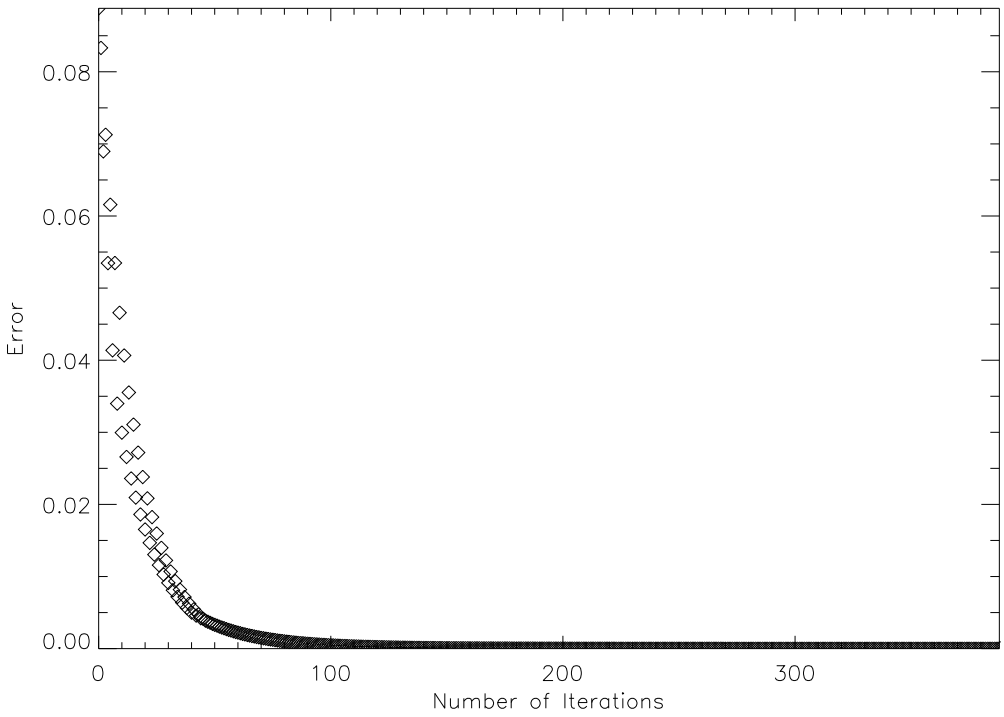

Figure 63.: Maximum error in H for each iteration versus number of iterations for $\omega = 1.9284489$. The total number of iterations to reach tolerance 10^{-6} was 469.

where N_{pix} is the number of pixels in object. Three levels of perception were considered (Bright, Newbury et al. 1997):

(1) **Visibility**: the ability to discern the object after knowing it is present. This level is acceptable for MREIM as an adjunctive imaging technique to characterize objects imaged in the simultaneous MRM examinations;

(2) **Detection**: the ability to find an object without a prior knowledge of its presence;

(3) **Shape outline**: the ability to outline an object.

Threshold values of d were taken from Rose (Rose 1948) and Bright et al. (Bright, Newbury et al. 1997):

- $d_{Rose} = 5$ for visibility;

- $d = 8$ for detection;

- $d = 12$ for shape outline.

Contrast-to-noise ratio and detectability were computed for difference MREIM simulation images (subtraction image of magnitude images obtained with current on and current off). The region of interest (ROI) for the object was outlined by the coordinates of the higher intensity disk in the template image. The ROI of the same shape and number of pixels (N_{pix}) was used to capture the signal from background.

8.2 Simulation Results: Simple (Idealized) Tumor Model

This Section provides the simulation results for a simple tumor model of a higher conducting sphere embedded in a lower conducting homogenous medium based on analytical solutions of aberrational magnetic field (Eq. (6.34)). First, the experimental images are replicated and analyzed with simulations. Then two MREIM effects are investigated with contrast diagrams to determine the SDSE sequence parameters providing the most conspicuous MREIM effect.

8.2.1 Replication of Experiment

Figures 64–67 show the comparisons of experimental images with simulations. Parameters such as TR, TE, N_p, fov, and dx were specified by the selected SDSE experimental sequence: $TR = 2$ s, $TE = 50$ ms, $N_p = 128$, $fov = 12.8$ cm, and $dx = 1$ mm. Geometry and conductivity ratio were estimated from the experimental phantom measurements: $R = 5$ mm and $\sigma_{ratio} \approx 23$. The current density through the phantom was estimated from the experiments and ranged from 10 to 17 A/m^2. Frequency resolution was varied ($df = 60$ Hz/pix in Figs. 60–62, and $df = 22$ Hz/pix in Fig. 63). For integer $TR = 2.0$ s, PE effect is observable at fractional generator frequencies. The Pasco Scientific PI-9587C Digital Function Generator-Amplifier resolution was 0.001 Hz with accuracy $0.01\% \pm 1$ digit. Zero mean Gaussian random variable, σ_{SD}, was added to the template image with a variance estimated from the experimental images. The method used to estimate the variance is discussed elsewhere (Sijberg, den Dekker et al. 1998).

Figure 64 shows the simulated MREIM images and their comparison with the experimental findings for the following experimental parameters: $i = 10$ A/m^2, $f \approx 300$ Hz, $df = 60$ Hz/pix, $\sigma_{SD} = 1.97$, and $contrast = 10\%$. In the simulation, $\sigma_{SD} = 2$ was used. The experimental images show that PE effect (shift in the $\hat{y}$ direction) is more pronounced than the FE effect (shift in the $\hat{x}$ direction). To reproduce this scenario, the shift in vertical direction was set to $\Delta y_{pix} = 2$, which resulted in fractional frequency $\{f\} = \frac{\Delta y_{pix}}{TR \cdot N} = \frac{2}{2 \cdot 128} = 0.008$ Hz. The shift in $\hat{x}$ direction is given as $\Delta x_{pix} = \frac{f}{df} = \frac{300}{60} = 5$ pix, which is equivalent to the tumor radius in pixels. For the shift equal or larger than tumor radius, two additional aberrational images of the tumor do not overlap (Fig. 42).

Experimental images in Figs. 65 and 66 show a different aspect of PE and FE effects combination. The MREIM parameters were the same as in the previous experiment (Fig. 64): $df = 60$ Hz/pix, $TR = 2$ s, and $TE = 50$ ms, but in Fig. 65, the applied current was increased to $i = 17$ A/m^2, and in Fig. 66, the generator frequency was increased to $f \approx 350$ Hz. Analysis of experimental images in Figs. 65 and 66 showed that the noise variance is 6 and 4.5 times higher in comparison with the previous example ($\sigma_{SD} = 12$ in Fig. 65 and $\sigma_{SD} = 9$ in Fig. 66).

Results obtained in Figs. 65 and 66 can be explained by considering the magnitude

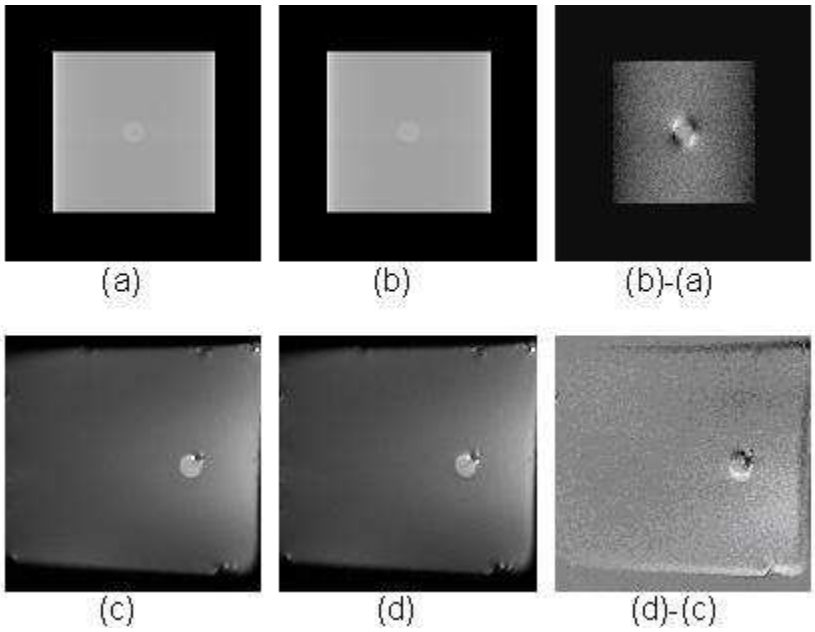

Figure 64.: Comparison of simulated MREIM images of higher conductive sphere ($R = 5$ mm) embedded in a lower conductive medium ($\sigma_{ratio} = 23$ and $contrast = 10\%$) with experimental results. The top row shows simulation images: (a) current off, (b) current on, $i = 10$ A/m^2 at $f = 300.008$ Hz, $df = 60$ Hz/pix, and $\sigma_{SD} = 2$, and (b)-(a) subtraction image of current on and current off. The second row shows the experimental images of (c) current off, (d) current on obtained at frequency set to $f \approx 300$ Hz, current density of $i = 10$ A/m^2, and frequency resolution $df = 60$ Hz/pix, and (d)-(c) subtraction image of current off and current on. The experimental conductivity ratio is estimated as 23, $contrast = 11\%$, and $\sigma_{SD} = 1.97$. Detectability of MREIM signal in experimental difference image was $d_{exp} = 7.8$, and in corresponding simulation image, $d_{sim} = 7.1$. Phase Encode effect is the most pronounced in this experiment.

subtraction images. Let the output pixel value (PV) at a given pixel with known value A with random noise in each channel be given by

$$PV_1 = [(A + n_{1x})^2 + (n_{1y})^2)]^{1/2} = [(A^2 + 2An_{1x} + (n_{1x})^2 + (n_{1y})^2]^{1/2}. \quad (8.7)$$

PV value for another signal is

$$PV_2 = [(B + n_{2x})^2 + (n_{2y})^2)]^{1/2} = [(B^2 + 2Bn_{1x} + (n_{2x})^2 + (n_{2y})^2]^{1/2}. \quad (8.8)$$

Finding the power of PV_1 and PV_2, subtracting and taking the square root will give

$$\sqrt{PV_2^2 - PV_1^2} = [A^2 - B^2 + 2(Bn_{2x} - An_{1x}) + (n_{2x})^2 - (n_{1x})^2 + (n_{2y})^2 - (n_{1y})^2]^{1/2}. \quad (8.9)$$

Note that the resulting signal is not just additive noise but also contains signal dependent noise terms. Subtraction images no longer display the shift, but show the aberration in the area of higher signal (higher conducting region).

In Fig. 67, experimental subtraction image of current on and off shows no MREIM effect. Here, the MREIM acquisition parameters were changed to $df = 22$ Hz/pix and $f = 200$ Hz, and the shift due to FE effect is $\Delta x_{pix} = \frac{f}{df} \approx 9$ pixels, which is almost equal to tumor diameter. Aberrational replications of original tumor due to FE effect are separated enough to be lost in noise. Noise variance in experimental images was found to be 10.

8.2.2 Study of the MREIM Effects

This Section provides the study of MREIM effects based on contrast diagrams. In the experiments, current was supplied during the entire image acquisition process. In practice, it is possible to apply current for selected parts of the sequence, for a Spin Echo sequence, the current pulse may be restricted to the signal acquisition time TS.

The MREIM simulation program provided the option of selectively turning on/off FE and PE effects. The parameters were optimized to produce the most conspicuous effect at the lowest applied current. This study was based on the simple tumor model using a simple SDSE sequence (used in experiment) with the following sequence parameters: $TR = 2$ s, $TE = 50$ ms, $N_p = 128$, $fov = 12.8$ cm, $dx = 1$ mm, and $G_{y_{max}} = 22$ mT/m. This parameter optimization based on the SDSE sequence can be used in future for more complex sequences and assist in designing generator pulse sequences time-coupled to MR sequences to produce the most conspicuous MREIM effect.

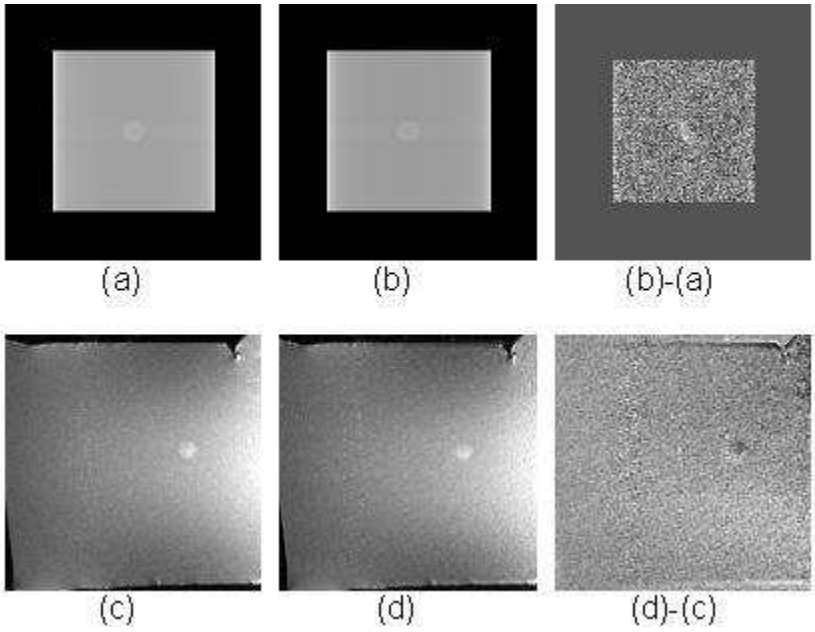

Figure 65.: Similar set-up to one in Fig. 64. Simulation parameters: $i = 17$ A/m^2, $f = 300.004$ Hz, $df = 60$ Hz/pix, $\sigma_{ratio} = 23$, $contrast = 9\%$, and $\sigma_{SD} = 12$. Experimental parameters: $i = 17$ A/m^2, $f = 300$ Hz, $df = 60$ Hz/pix, $\sigma_{ratio} = 23$, $contrast = 9\%$, and $\sigma_{SD} = 12$. MREIM signal detectability is $d_{exp} = 5.1$ for experimental subtraction image, and $d_{sim} = 5.4$ for corresponding simulation image. MREIM signal is affected by noise, which results in appearance of aberration in subtraction images in the area of higher signal in current on/off images.

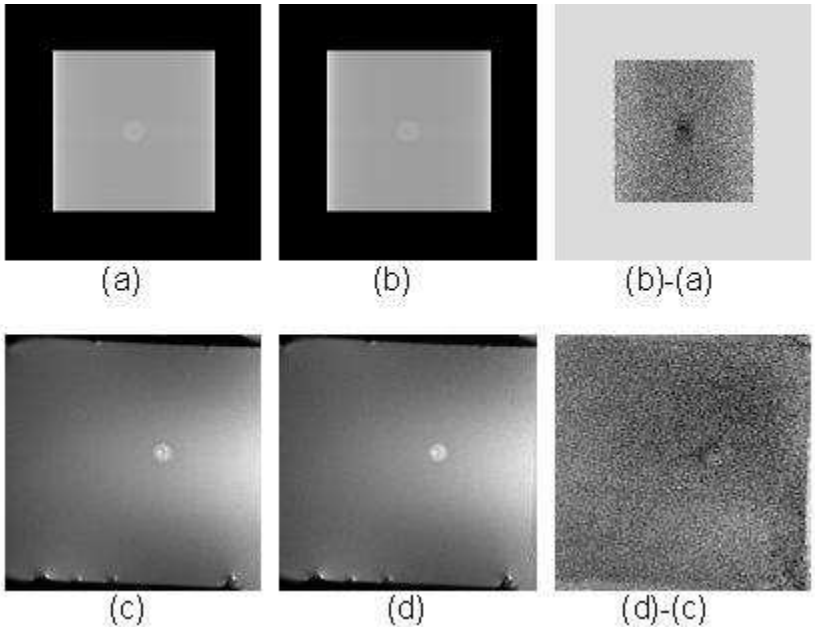

Figure 66.: Similar set-up as in Fig. 64: $i = 10$ A/m^2, $df = 60$ Hz/pix, $\sigma_{ratio} = 23$, $contrast = 10\%$, and $\sigma_{SD} = 9$, the driving frequency was set to $f = 350.004$ Hz. It is compared with corresponding experimental images acquired at the following parameters: $i = 10$ A/m^2, $df = 60$ Hz/pix, $\sigma_{ratio} = 23$, $contrast = 10\%$, and $\sigma_{SD} = 9$, and $f \approx 350.004$ Hz. MREIM signal detectability is $d_{exp} = 5.8$ from experiment and $d_{sim} = 6.2$ from simulation. MREIM signal is affected by noise, which results in appearance of aberration in subtraction images in the area of higher signal in current on/off images.

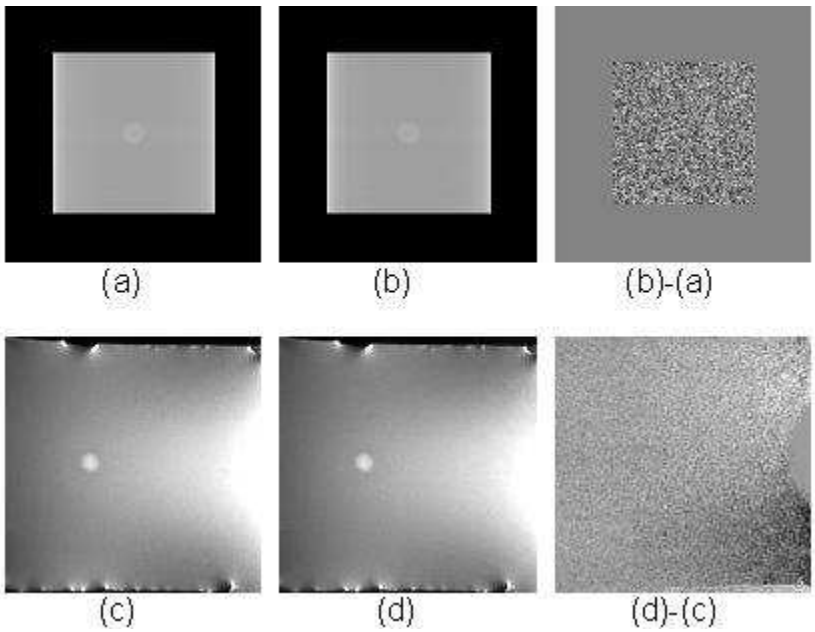

Figure 67.: Comparison of MREIM simulation images for the following set of parameters: $i = 10$ A/m^2 at $f = 200.004$ Hz, $df = 22$ Hz/pix, $\sigma_{ratio} = 23$, $contrast = 10\%$, and $\sigma_{SD} = 10$ with the corresponding experimental images acquired at the following parameters: $i = 10$ A/m^2 at $f = 200.004$ Hz, $df = 22$ Hz/pix, $\sigma_{ratio} = 23$, $contrast = 10\%$, and $\sigma_{SD} = 10$. MREIM signal detectability is considerably below the visibility threshold of 5, $d \approx 0.6$ for both experiment and simulation. The MREIM effect is not present since the shift due to FE effect is almost equal to tumor diameter, $\Delta x_{pix} = \frac{f}{df} \approx 9$ pixels.

FE Effect

In this section, the FE effect analysis is provided based on detectability diagrams. The signal generator is engaged for time, $TS = \frac{1}{df \cdot N}$, during the FE gradient application. The resulting perturbation signal for this case is expressed as

$$S(t, G_{y_p}) = \int\int \rho(x,y) e^{j\gamma G_x x t} e^{j\gamma G_{y_p} y \tau} e^{j\frac{\gamma\mu_0 h(x,y)}{\Omega}\sin\Omega t} dxdy, \tag{8.10}$$

which gives

$$\rho(x,y) - \frac{\gamma\mu_0}{2\Omega}\rho(x+\Delta x, y)h(x+\Delta x, y) + \frac{\gamma\mu_0}{2\Omega}\rho(x-\Delta x, y)h(x-\Delta x, y), \tag{8.11}$$

where $\Delta x = \frac{f}{df}$ and $\Omega = 2\pi f$.

From Eq. (6.34), we conclude that the entire image shifts since magnetic field strength for both regions is proportional to x. Subtracting the images obtained with current on and off yields

$$\frac{\gamma\mu_0}{2\Omega}[\rho(x-\Delta x, y)h(x-\Delta x, y) - \rho(x+\Delta x, y)h(x+\Delta x, y)]. \tag{8.12}$$

The FE effect depends on (a) the shift in $\hat{x}$, $\Delta x = \frac{f}{df}dx$, and its relation to tumor size, (b) aberrational magnetic field strength, which in turn depends on applied current and conductivity ratio. Influence of these parameters on FE effect detectability is tested in Figs. 68–71.

The FE effect detectability is characterized as the function of the shift produced by $\frac{f}{df}$ ratio (Fig. 68). Five frequency resolutions were used to explore detectability based on the experiments: *df* =20, 40, 60, 80, and 100 Hz/pix. The shift $\Delta x = 1$ produced the highest detectability for all frequency resolutions. Detectability is the highest with $f = 20$ Hz and *df* = 20 Hz/pix. Lower frequency resolution, *df*, produces higher signal-to-noise ratio. Also, *df* is proportional to FE gradient strength. At lower gradient strengths, the aberrational magnetic field has a stronger effect. The generator frequency is also preferable in lower range since the aberrational term in Eq. (8.10) is inversely proportional to Ω. Lower generator frequency agree with the real-value approximation. Also, the FSs coupling is based on lower generator frequencies.

The behavior of the FE effect as a function of shift Δx and tumor radius can be observed in Fig. 42. When $\Delta x > R$, the aberrational replicas of higher conducting region do not

overlap and no longer carry the information about tumor location, unless with known shift, they are shifted back and added.

Considering results from Fig. 68, we will use $f = 20$ Hz and $df = 20$ Hz/pix for investigation of FE effect behavior with other MREIM parameters. Figure 69 shows the dependence of the FE effect detectability on initial tumor contrast. The maximum *contrast* value of 10% was estimated from experimental images. Contrast is measured as $conrast = \frac{S_{in}-S_{out}}{S_{out}} \cdot 100\%$, where S_{in} and S_{out} are pixel intensities inside and outside the tumor, correspondingly. From Fig. 69, we conclude that FE effect does not depend on initial tumor contrast. Since the MREIM effect is observable in the low-contrast and zero-contrast images, MREIM has the potential to eliminate the use of contrast agents in current MRM.

Figure 70 shows the FE effect detectability as a function of conductivity ratio of the tumor and surrounding tissues. There are no tissues in breast that are less conductive than connective and adipose tissue (see Tables 2–5). Taking this into consideration, the conductivity ratio was varied from 1 to 40. From Fig. 70, the FE effect detectability passed the visibility threshold at conductivity ratio of 2. Starting with $\sigma_{ratio} = 17$, the detectability of the FE effect reached the plateau. Our experiments were conducted using a breast phantom with $\sigma_{ratio} = 23$.

Applied current limits for this specific sequence were found for the lowest cancer differentiation conductivity ratio $\sigma_{ratio} = 3$ and three tumor radii, $R = 5$, 2,5, and 1.5 mm based on the contrast diagram in Fig. 71. For all three radii, the lowest current density was 2 A/m^2. As predicted by theory (Eq. (6.34)), the detectability dependence on current density is linear since the aberrational magnetic field strength is directly proportional to current density.

PE Effect

This Section provides the analysis for periodic PE effect (SDSE sequence, sequential acquisition mode and PE mode). Other acquisition/PE modes are investigated in Section 9.1. When the signal generator is engaged for time $T_{seq} - \frac{TS}{2} = TR \cdot p + TE - \frac{TE}{2}$, the aberrational magnetic field will influence the phase encoding misregistering the spacial frequencies in $\hat{y}$. Then the signal for p-th encode line can be found as

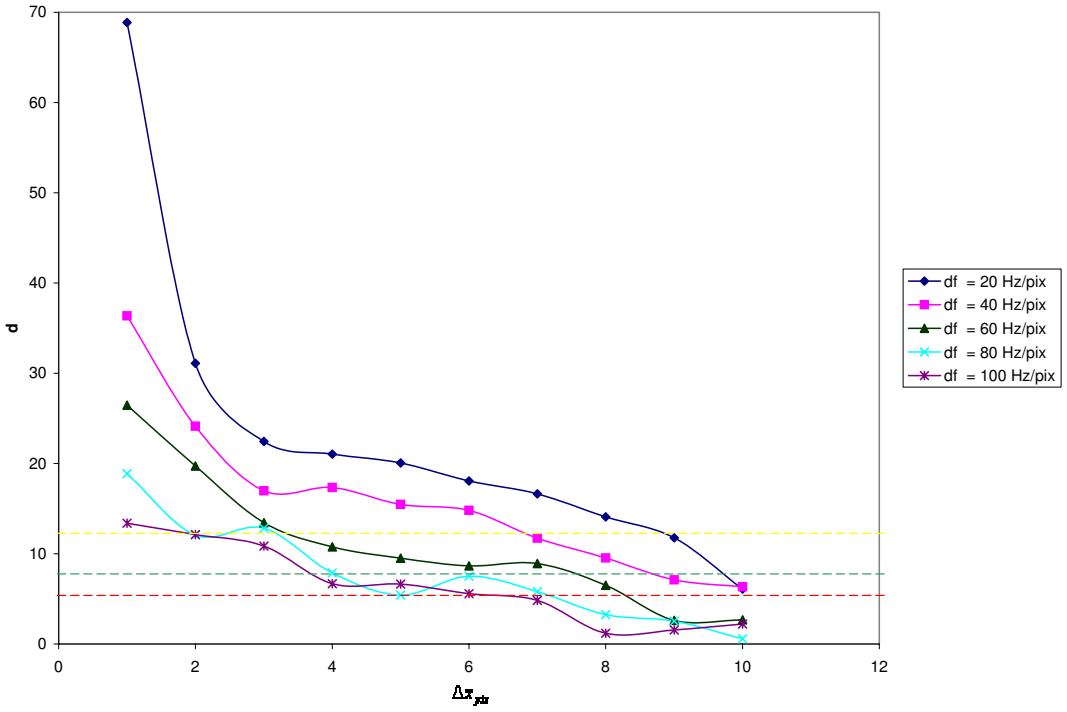

Figure 68.: Frequency Encode effect study: Dependence of detectability of MREIM signal on the shift in x, $\Delta x = \frac{f}{df}$. Simulation images were generated for the following parameters: $R = 5$ mm, $contrast = 10\%$, $\sigma_{ratio} = 20$, $\sigma_{SD} = 2$, and $i = 10$ A/m^2. Dotted colored lines denote (red) visibility threshold, (green) detection threshold, and (yellow) shape outline threshold.

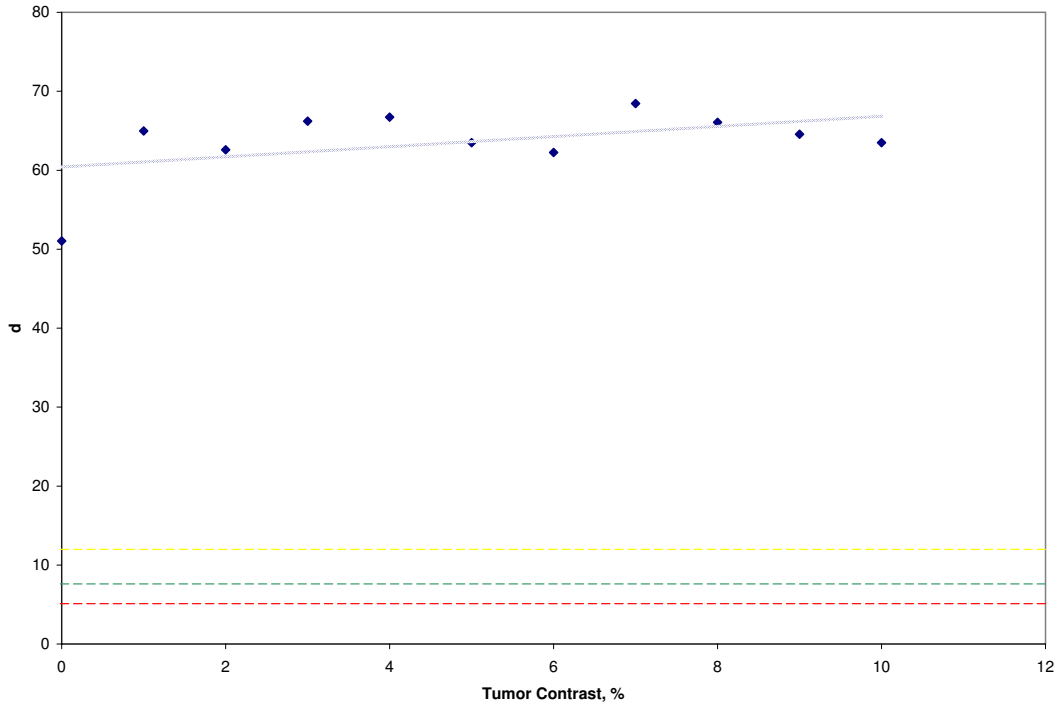

Figure 69.: Frequency Encode effect study: Dependence of detectability of MREIM signal on initial tumor contrast. The following parameters were used for simulation: $i = 10$ A/m^2, $f = 20$ Hz, $df = 20$ Hz/pix, $R = 5$ mm, $\sigma_{ratio} = 20$, and $\sigma_{SD} = 2$. Dotted colored lines denote (red) visibility threshold, (green) detection threshold, and (yellow) shape outline threshold.

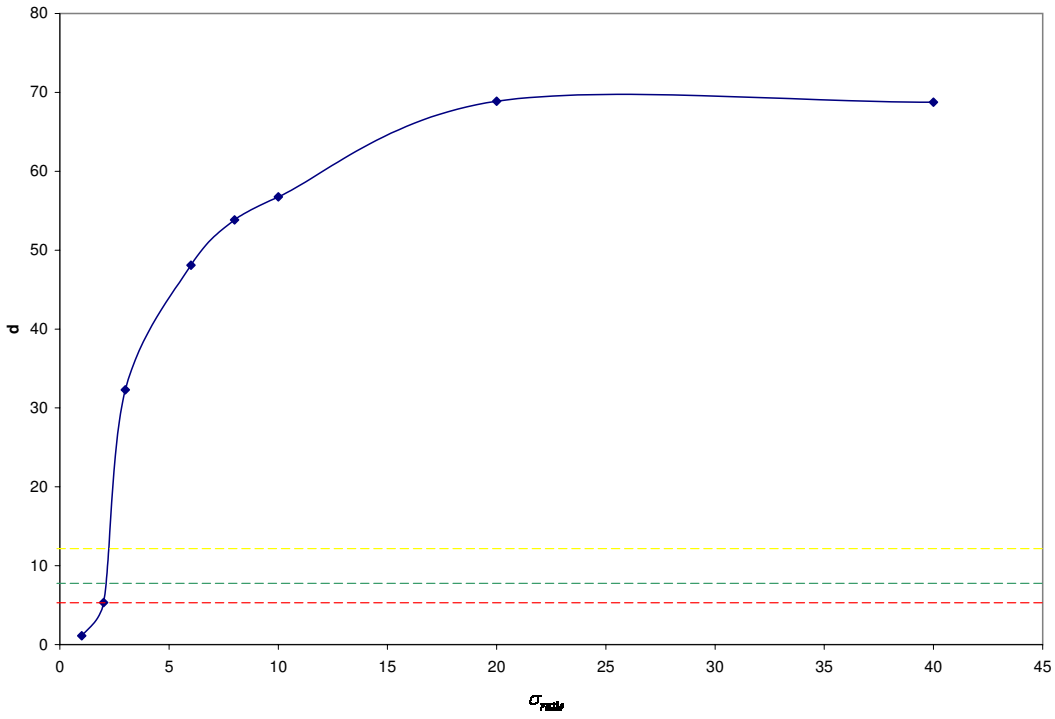

Figure 70.: Frequency Encode effect study: Dependence of detectability of MREIM signal on conductivity ratio between the tumor and surrounding tissue. The following parameters were used for simulation: $i = 10$ A/m^2, $f = 20$ Hz, $df = 20$ Hz/pix, $R = 5$ mm, $contrast = 0$, and $\sigma_{SD} = 2$. Dotted colored lines denote (red) visibility threshold, (green) detection threshold, and (yellow) shape outline threshold.

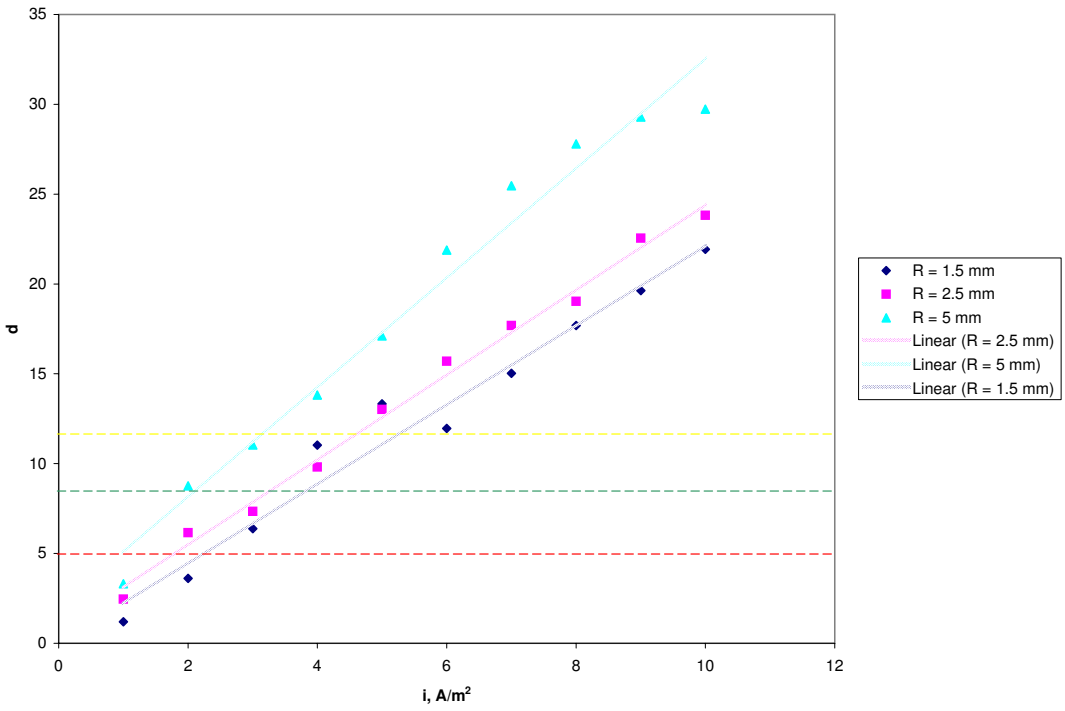

Figure 71.: Frequency Encode effect study: Dependence of detectability of MREIM signal on applied current for three tumor radii, $R = 5$, 2.5, and 1.5 mm. The following parameters were used: $f = 20$ Hz, $df = 20$ Hz/pix, $contrast = 0$, $\sigma_{ratio} = 3$, and $\sigma_{SD} = 2$. Dotted colored lines denote (red) visibility threshold, (green) detection threshold, and (yellow) shape outline threshold.

$$S(t, G_{y_p}) = \int\int \rho(x,y) e^{j\gamma G_x x t} e^{j\gamma G_{y_p} y \tau} e^{j\gamma\mu_0 h(x,y) \int_t \cos(\Omega t + \varphi_0) dt} dxdy. \tag{8.13}$$

The aberrational term for a Spin Echo sequence will go through two stages of phase accumulation: before 180° pulse and after 180° pulse with an opposite sign. This accumulation of phase is particular for a sequence, PE mode, and acquisition mode. It will be studied further in Chapter 9. For the SDSE sequence, Eq. (8.13) can be rewritten as follows:

$$S(t, G_{y_p}) = \int\int \rho(x,y) e^{j\gamma G_x x t} e^{j\gamma G_{y_p} y \tau} e^{j\frac{\gamma\mu_0 A}{\Omega} h(x,y) sin\Omega \cdot TR \cdot p} dxdy, \tag{8.14}$$

where A is a factor depending on sequence timing parameters TE and TS (inversely proportional to df) and generator frequency f (see Eq. (6.74)).

It is required for PE effect to be observable at integer repetition time $TR = 2$ s to supply current at fractional frequencies. In this case, the shift in y will be produced, $\Delta y = \{f\} \cdot TR \cdot N_p \cdot dy$, where $\{f\}$ is a fractional part of generator frequency. The resulting image will contain the original image and two aberrational versions of original image (scaled by $\frac{\gamma\mu_0 A}{2\Omega}$ and shifted by Δy) (Fig. 43). When subtracting current off and current on images, we obtain

$$\frac{\gamma\mu_0 A}{2\Omega}[\rho(x, y - \Delta y)h(x, y - \Delta y) - \rho(x, y + \Delta y)h(x, y + \Delta y)]. \tag{8.15}$$

Because aberrational magnetic field depends on y only at the boundaries of tumor, PE effect consists in shifting the boundaries of higher conducting areas (Fig. 43). For smaller shifts, in subtraction images the intensity of area inside and outside the tumor vanishes except for the boundaries. With the shift increase, the boundaries are smeared out, and when Δy reaches R, two separate replicas of higher conductive region can be observed. Unlike FE effect, these aberrational images have opposite intensity, such that, when added, they diminish.

Figure 72 proves the above assertion showing detectability diagram as a function of shift in $\hat{y}$. The values of detectability are well below visibility threshold and are mostly influenced by noise.

As a conclusion, PE effect influences the boundaries of higher conducting tumor, and smaller shifts in $\hat{y}$ are preferable in terms of carrying the information about tumor location.

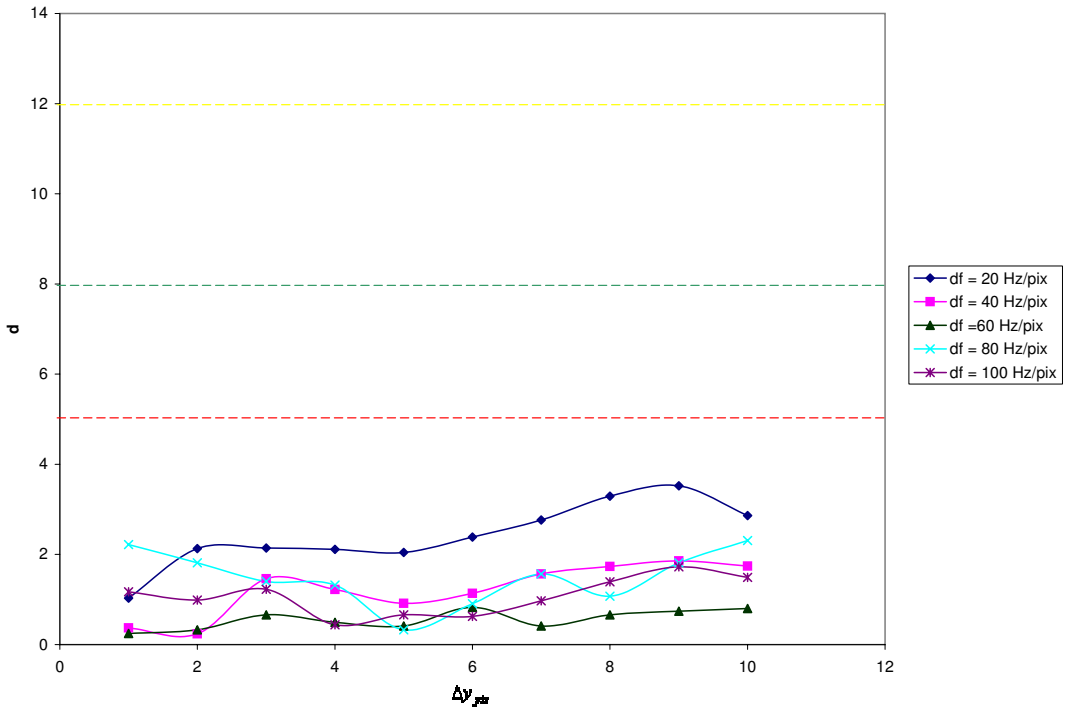

Figure 72.: Phase Encode effect study: Dependence of detectability of MREIM signal on the shift in the $\hat{y}$ direction, $\Delta y_{pix} = \{f\} \cdot TR \cdot N_p$, where $TR = 2$ s, and $N_p = 128$. Simulation images were acquired with the following parameters: $\Delta x_{pix} = 1$ (FE effect os off), $i = 10$ A/m^2, $R = 5$ mm, $contrast = 10\%$, $\sigma_{ratio} = 20$, and $\sigma_{SD} = 2$. Dotted colored lines denote (red) visibility threshold, (green) detection threshold, and (yellow) shape outline threshold.

Combination of Effects

When generator is engaged for the entire time of image acquisition, two effects conspire creating the shifts in both $\hat{x}$ and $\hat{y}$. When subtracting images obtained with current on and off we obtain

$$\begin{aligned}&\frac{\gamma\mu_0}{2\Omega}[\rho(x-\Delta x,y)h(x-\Delta x,y)-\rho(x+\Delta x,y)h(x+\Delta x,y)+\\&A\rho(x,y-\Delta y)h(x,y-\Delta y)-A\rho(x,y+\Delta y)h(x,y+\Delta y)].\end{aligned} \tag{8.16}$$

Figures 73–77 show detectability plots for combinations of FE and PE effects. The analysis is similar to the one used for FE. First, Δx and Δy that produce the most conspicuous combined effect (Figs. 73–74) are found.

The combination of FE and PE effects is characterized as function of tumor contrast (Fig. 75), conductivity ratio (Fig. 76), and, finally, current density limits are found for three tumor radii using $\sigma_{ratio} = 3$ and $contrast = 0$. The optimized values of shift were found to be $\Delta x_{pix} = 1$ and $\Delta y_{pix} = 1$ for $df = 20$ Hz/pix, resulting in generator frequency of $f = 20.004$ Hz. Overall, the contrast diagrams for combined MREIM effect resembled those for FE effect for the reasons specified in previous section. Minimum current limits remained the same for combined effects, $i = 2$ A/m^2 for R= 5, 2.5, and 1.5 mm (Fig. 77). Figure 78 provides the simulation difference images for spheres with three different radii with low conductivity ratio of $\sigma_{ratio} = 3$ at the lowest current limit of $i = 2$ A/m^2 that permits tumor visibility. Addition of PE effect allows for better differentiation of the tumor by enhancing the tumor boundaries.

8.2.3 Summary

For the simple tumor model using the SDSE sequence ($TR = 2$ s, $TE = 50$ ms, and $N_p = 128$) we obtained the following results:

1. MREIM images were simulated for experimental parameters that replicated the experiment:

- (Experiment 1, Fig. 64) $i = 10$ A/m^2 at $f = 300.008$ Hz, $df = 60$ Hz/pix, and $\sigma_{SD} = 2$ ($d_{exp} = 7.8$, $d_{sim} = 7.1$),

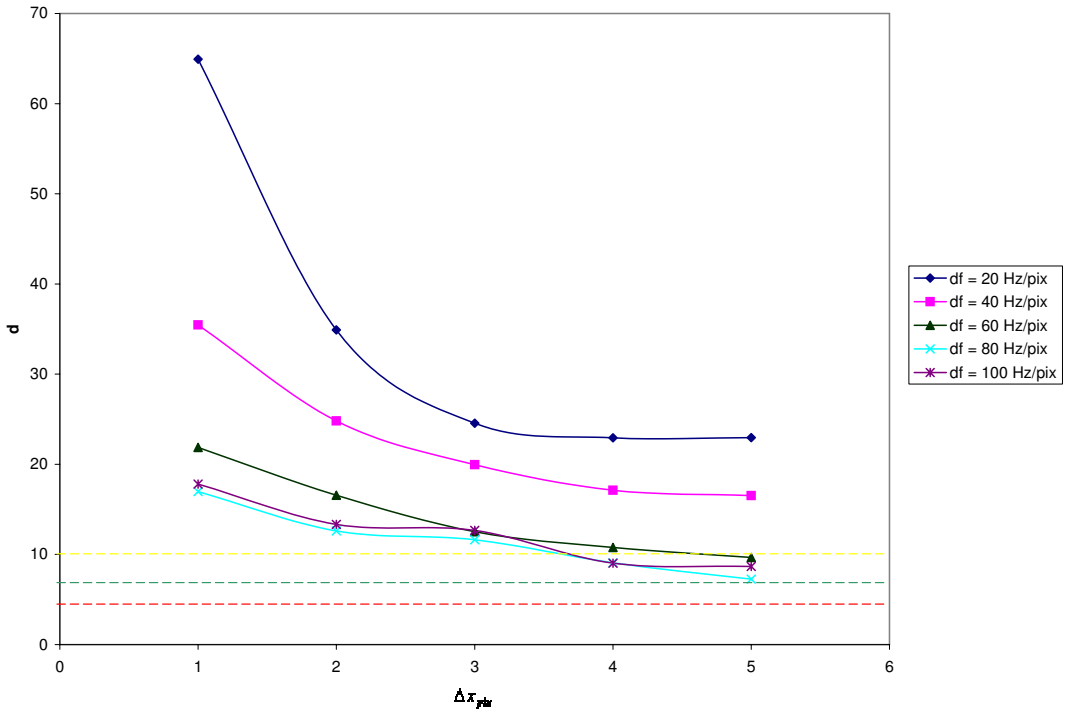

Figure 73.: Combination of effects: Dependence of detectability of MREIM signal on the shift in x, $\Delta x = \frac{f}{df}$. Simulation images were acquired with the following parameters: $\Delta y_{pix} = 1$, $\{f\} = 0.004$ Hz, $i = 10$ A/m^2, $R = 5$ mm, $contrast = 10\%$, $\sigma_{ratio} = 20$, and $\sigma_{SD} = 2$. Dotted colored lines denote (red) visibility threshold, (green) detection threshold, and (yellow) shape outline threshold.

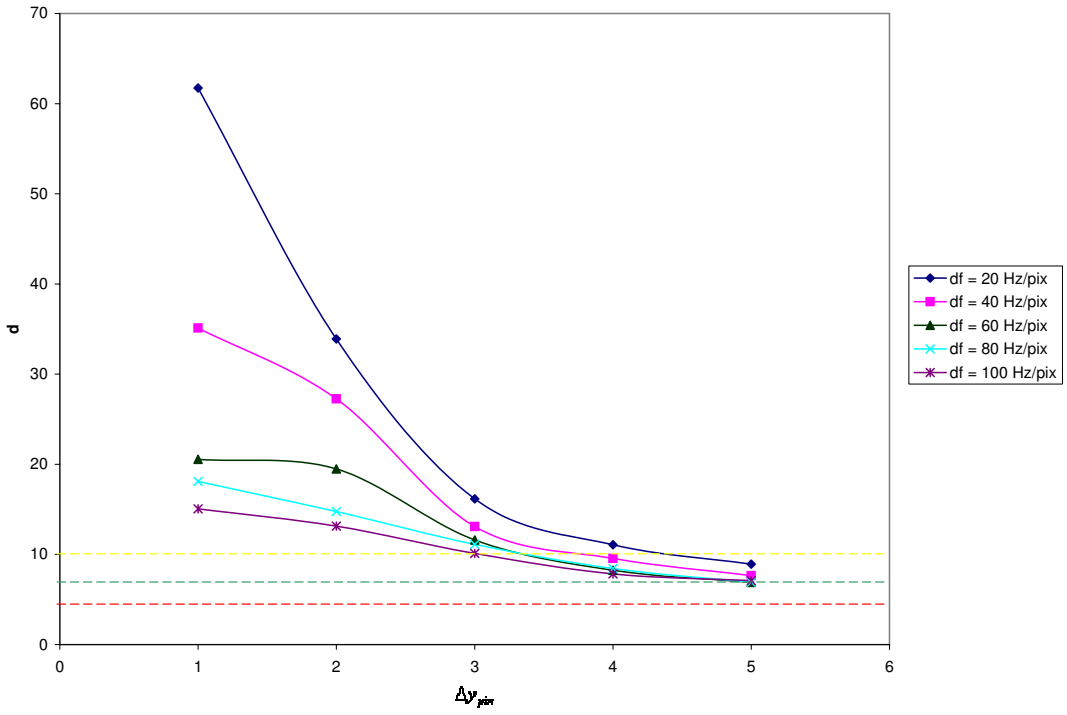

Figure 74.: Combination of effects: Dependence of detectability of MREIM signal on the shift in y direction, $\Delta y_{pix} = \{f\} \cdot TR \cdot N_p$, where $TR = 2$ s, and $N_p = 128$. Simulation images were acquired with the following parameters: $\Delta x_{pix} = 1$, $i = 10$ A/m^2, $R = 5$ mm, $contrast = 10\%$, $\sigma_{ratio} = 20$, and $\sigma_{SD} = 2$. Dotted colored lines denote (red) visibility threshold, (green) detection threshold, and (yellow) shape outline threshold.

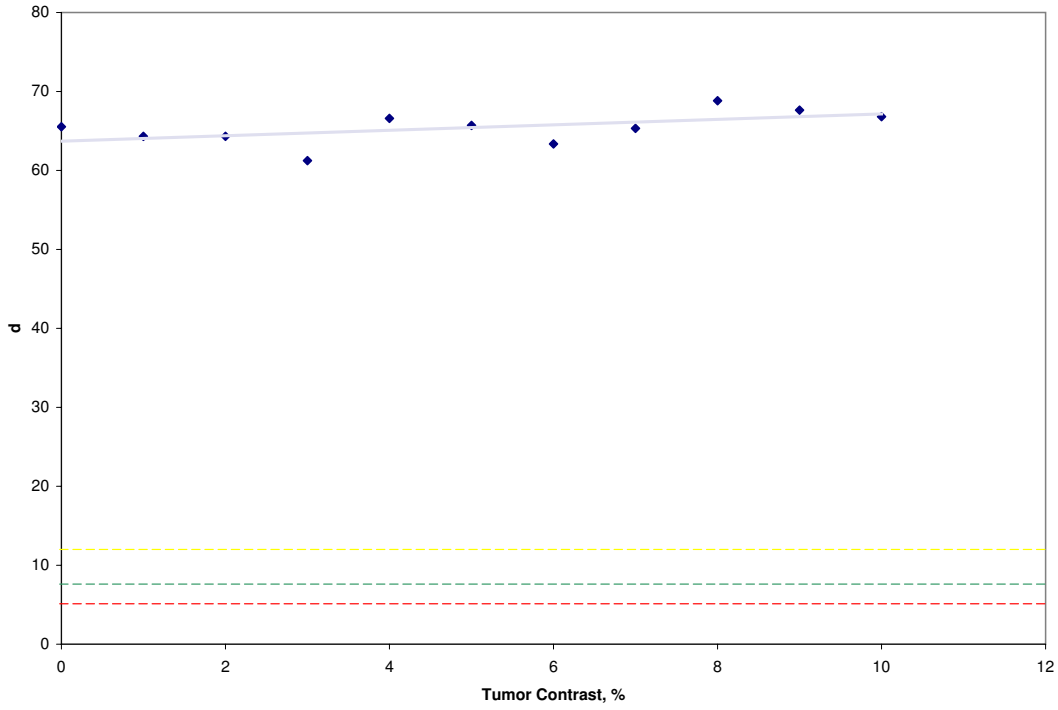

Figure 75.: Combination of effects: Dependence of detectability of MREIM signal on initial tumor contrast. The following parameters were used for simulation: $i = 10$ A/m^2, $f = 20.004$ Hz, $df = 20$ Hz/pix, $R = 5$ mm, $\sigma_{ratio} = 20$, and $\sigma_{SD} = 2$. Dotted colored lines denote (red) visibility threshold, (green) detection threshold, and (yellow) shape outline threshold.

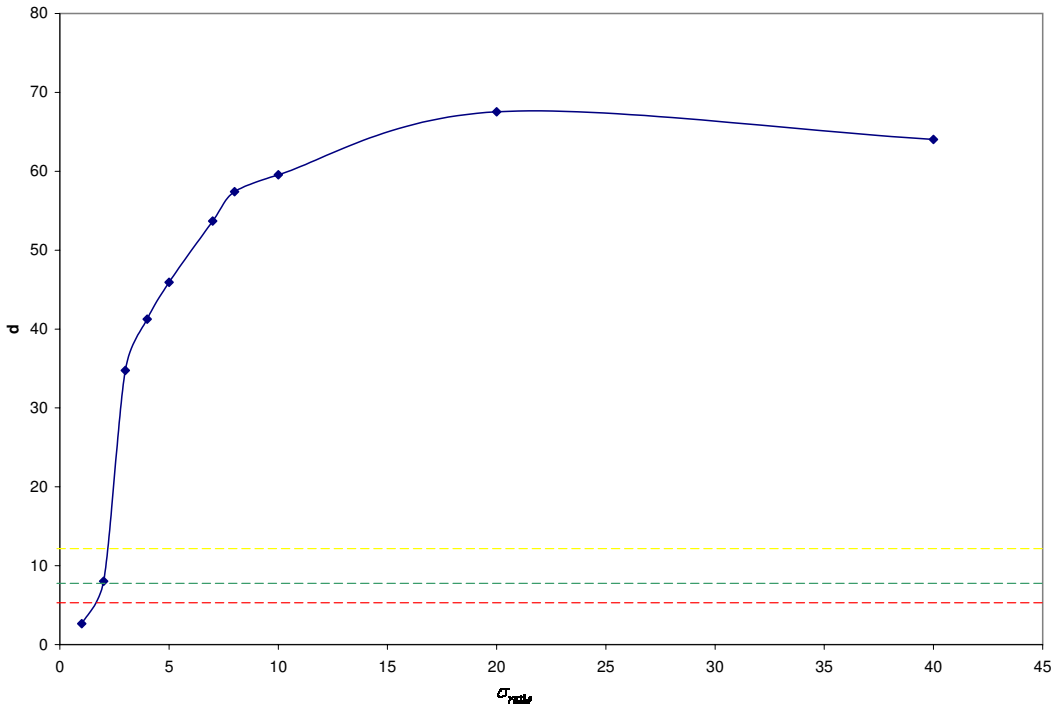

Figure 76.: Combination of effects: Dependence of detectability of MREIM signal on the conductivity ratio between the tumor and surrounding tissue. The following parameters were used for simulation: $i = 10$ A/m^2, $f = 20.004$ Hz, $df = 20$ Hz/pix, $R = 5$ mm, $contrast = 0$, and $\sigma_{SD} = 2$. Dotted colored lines denote (red) visibility threshold, (green) detection threshold, and (yellow) shape outline threshold.

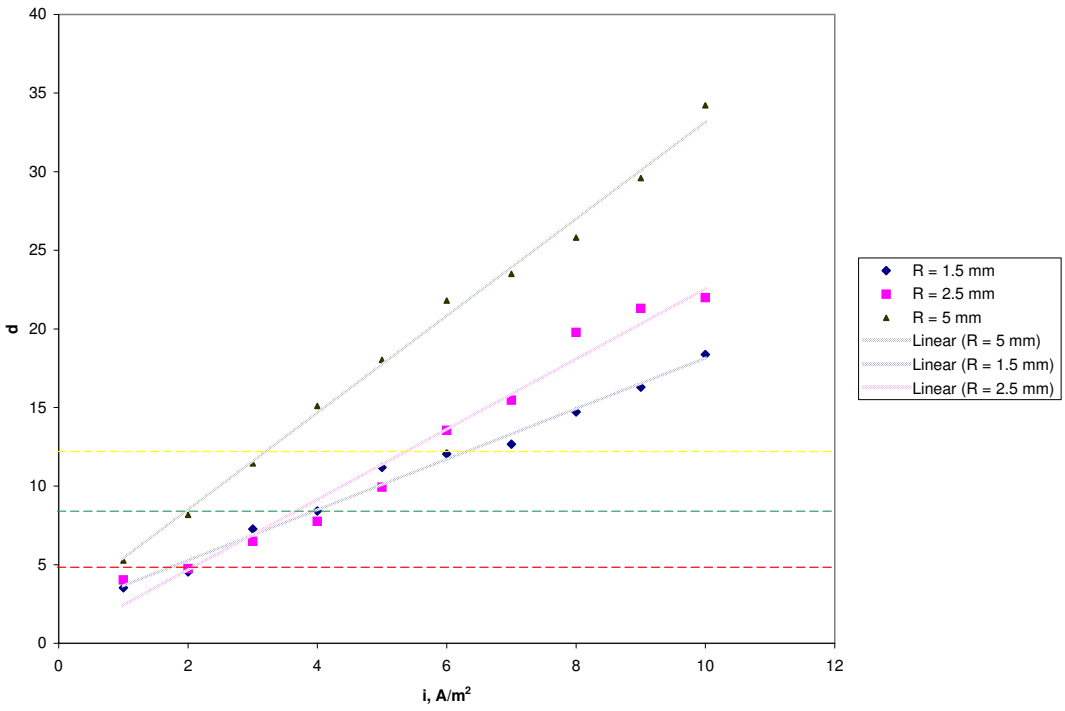

Figure 77.: Combination of effects: Dependence of detectability of MREIM signal on applied current for three tumor radii, $R = 5$, 2.5, and 1.5 mm. The following parameters were used: $f = 20.004$ Hz, $df = 20$ Hz/pix, $contrast = 0$, $\sigma_{ratio} = 3$, and $\sigma_{SD} = 2$. Dotted colored lines denote (red) visibility threshold, (green) detection threshold, and (yellow) shape outline threshold.

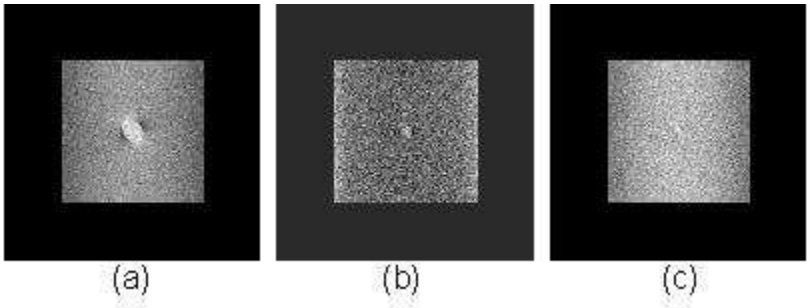

Figure 78.: MREIM simulation difference images for current limit of $i = 2$ A/m^2 for three tumor radii, $R = 5$, 2.5, and 1.5 mm with conductivity ratio $\sigma_{ratio} = 3$ and initial tumor contrast, $contrast = 0$.

- (Experiment 2, Fig. 65) $i = 17$ A/m^2 at $f = 300.004$ Hz, $df = 60$ Hz/pix, and $\sigma_{SD} = 12$ ($d_{exp} = 5.1$, $d_{sim} = 5.4$),

- (Experiment 3, Fig. 66) $i = 10$ A/m^2 at $f = 350.004$ Hz, $df = 60$ Hz/pix, and $\sigma_{SD} = 9$ ($d_{exp} = 5.8$, $d_{sim} = 6.2$),

- (Experiment 4, Fig. 67) $i = 10$ A/m^2 at $f = 200.004$ Hz, $df = 22$ Hz/pix, and $\sigma_{SD} = 10$ ($d_{exp} = d_{sim} = 0.6$);

2. Frequency Encode effect consists in creating the image consisting of three terms, original image and two filtered replicas of original image scaled by factor inversely proportional to f and directly proportional aberrational magnetic field and shifted by $\Delta x_{pix} = \frac{f}{df}$. The maximum MREIM signal detectability is observed at $\Delta x = 1$ and $df = 20$ Hz/pix;

3. Phase Encode effect (for SDSE sequence, sequential mode) consists in creating the image consisting of three terms, original image and two replicas of original image scaled by a factor inversely proportional to f and directly proportional to A (A_{max}=2) and aberrational magnetic field, and shifted by $\Delta y_{pix} = \{f \cdot TR\}N_p$. Phase Encode is studied for different acquisition/PE modes in Section 9.1;

4. Frequency Encode and Phase Encode effects conspire linearly;

5. For combined FE+PE effects:

- optimum generator frequency and frequency resolution are $f = 20.004$ Hz and $df = 20$ Hz/pix;

- initial tumor contrast does not influence tumor detectability. The MR sequence can be designed disregarding requirement of high tumor contrast;

- MREIM effect is detectable for conductivity ratio as low as $\sigma_{ratio} = 2$;

- minimum current density range for tumor detectability is $i = 1$–2 A/m^2 for the following tumor radii, $R = 5$, 2.5, and 1.5 mm, with low conductivity ratio of $\sigma_{ratio} = 3$ and $contrast = 0$.

8.3 Simulation Results: Realistic Tumor Models

This Section provides simulation results for realistic tumor models of complex tumor geometries and anisotropic conductivity distributions. The MREIM simulations were performed based on numerical solutions of aberrational magnetic field (Eq. (6.49)). First, the validity of field calculations was investigated in Section 6.2, then validity of MREIM simulation results is characterized with respect to the simulated MREIM images based on analytical expression of aberrational magnetic field (Eq. (6.34)) for a simple model of higher conducting sphere embedded in isotropic conducting medium. Comparison of difference MREIM images is provided in Fig. 78. The simulation was performed for the following parameters: $R = 5$ mm, $TR = 2$ s, $TE = 50$ ms, $N_p = 128$, $i = 10$ A/m^2 at $f = 20$ Hz, $df = 20$ Hz/pix, $\sigma_{ratio} = 3$, $contrast = 0$, and $\sigma_{SD} = 2$. For this case, only the FE effect is present. Detectability values obtained from the analytical and numerically calculated fields were were $d = 32.5$ and $d = 30.1$, correspondingly.

8.3.1 Spherical Tumor with Isotropic and Anisotropic Conductivity

This Section provides simulation images of realistic conductivity distributions. For comparison purposes, a set of MREIM field images and MREIM difference images is provided for an anisotropic conductivity distribution (Fig. 80).

The deviation in conductivity values is added to simulate realistic anisotropic conductivity breast tissue. Figure 81 shows the field images and MREIM difference images for

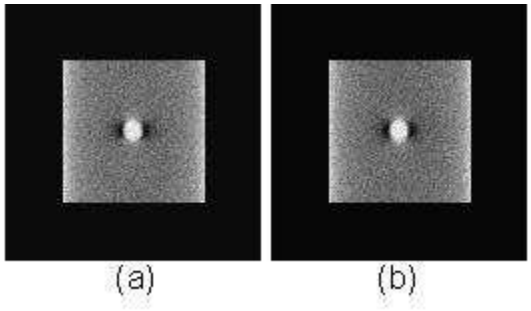

Figure 79.: Comparison of MREIM simulation difference images obtained using (a) analytical field solutions (d=32.5) and (b) numerical field solutions (d=30.1). The following parameters were used: $R = 5$ mm, $TR = 2$ s, $TE = 50$ ms, $N_p = 128$, $i = 10$ A/m^2 at $f = 20$ Hz, $df = 20$ Hz/pix, $\sigma_{ratio} = 3$, $contrast = 0$, and $\sigma_{SD} = 2$.

the following tumor model: a spherical cancer lesion ($R = 5$ mm) with randomly distributed conductivity ($\sigma = (0.3 \pm 0.01)$ S/m) with a variable conductivity background ($\sigma = (0.1 \pm 0.01)$ S/m). The deviation in conductivity values was achieved by adding normally distributed random variable with zero mean and standard deviation of 0.01 S/m to the conductivity image. Thus, the minimum conductivity ratio between tumor and surrounding tissue is $\sigma_{ratio} = 2.63$. When compared with the detectability value obtained for isotropic case ($d = 30.1$), the detectability for the isotropic case is slightly less, $d = 28.6$.

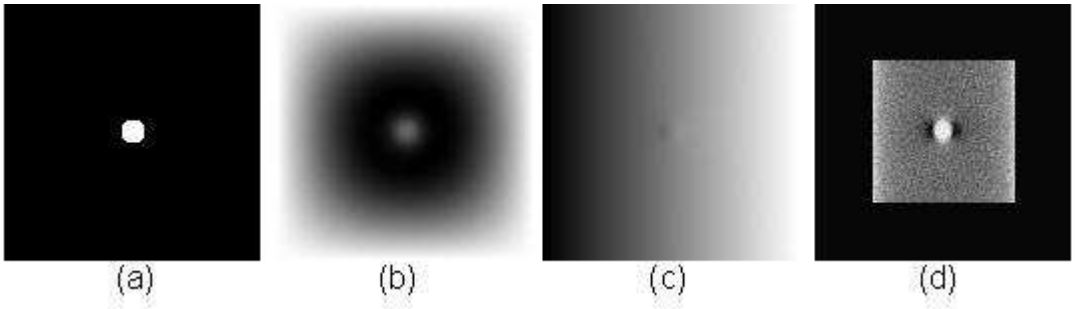

Figure 80.: Images of (a) conductivity, (b) electric potential, and (c) magnetic field strength at $z = N/2$ and $i = 10$ A/m^2 for a spherical cancer lesion with isotropic conductivity with $\sigma_{ratio} = 3$. MREIM simulation difference image is presented in (d). The following parameters were used in simulation: $R = 5$ mm, $TR = 2$ s, $TE = 50$ ms, $N_p = 128$, $f = 20$ Hz, $df = 20$ Hz/pix, $contrast = 0$, and $\sigma_{SD} = 2$. Detectability of MREIM signal is $d = 30.1$

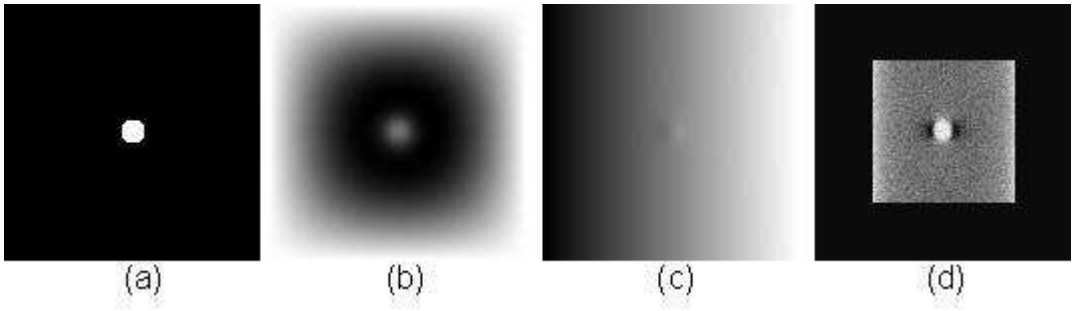

Figure 81.: Images of (a) conductivity, (b) electric potential, and (c) magnetic field strength at $z = N/2$ and $i = 10$ A/m^2 for a spherical cancer lesion with randomly distributed conductivity ($\sigma = (0.3 \pm 0.01)$ S/m) on a variable conductivity background ($\sigma = (0.1 \pm 0.01)$ S/m). MREIM simulation difference image is presented in (d). The following parameters were used in simulation: $R = 5$ mm, $TR = 2$ s, $TE = 50$ ms, $N_p = 128$, $f = 20$ Hz, $df = 20$ Hz/pix, $contrast = 0$, and $\sigma_{SD} = 2$. Detectability of MREIM signal is $d = 28.6$

8.3.2 Various Tumor Shapes with Anisotropic Conductivity

According to BI-RADS lexicon, masses are described by these four shapes:

- round
- oval
- lobular
- irregular.

The MREIM effect is investigated for oval, lobular, and irregular cancerous lesions. Figures 82–84 show the MREIM field images and corresponding MREIM difference images for oval, lobular, and irregular shapes. Resulting detectability values are provided in Table 11.

8.3.3 4-Tumor Model

The 4-tumor model is defined as follows: four spherical tumors with different conductivities are embedded into the normal breast tissue with anisotropic conductivity $\sigma = (0.1 \pm 0.01)$ S/m. The conductivity image for $z = N/2$ is shown in Fig. 98(a). The center locations,

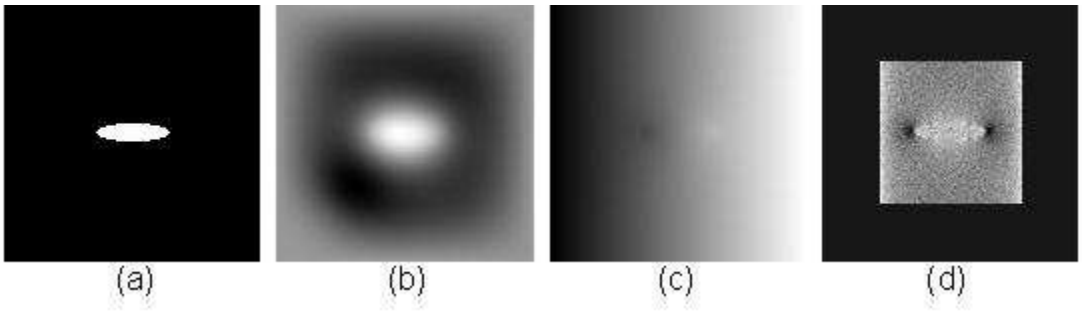

Figure 82.: Images of (a) conductivity, (b) electric potential, and (c) magnetic field strength at $z = N/2$ for an ellipsoidal cancer lesion at $i = 10$ A/m^2 with randomly distributed conductivity ($\sigma = (0.3 \pm 0.01)$ S/m) on a variable conductivity background ($\sigma = (0.1 \pm 0.01)$ S/m). MREIM simulation difference image is presented in (d). The following parameters were used in simulation: $R = 5$ mm, $TR = 2$ s, $TE = 50$ ms, $N_p = 128$, $f = 20$ Hz, $df = 20$ Hz/pix, $contrast = 0$, and $\sigma_{SD} = 2$.

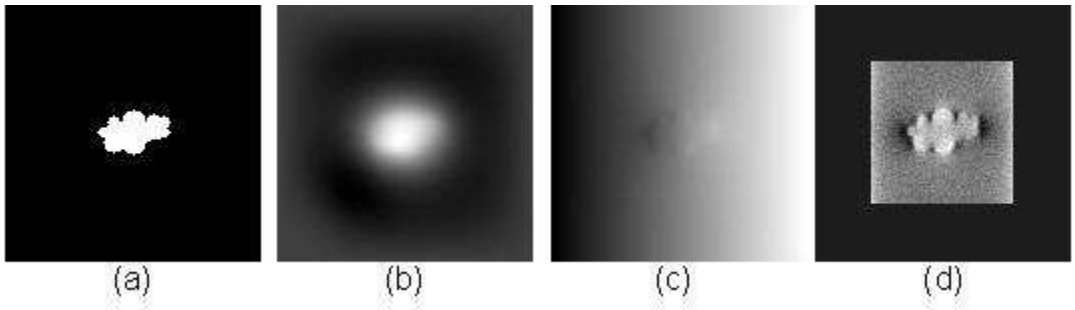

Figure 83.: Images of (a) conductivity, (b) electric potential, and (c) magnetic field strength at $z = N/2$ for a lobular cancer lesion at $i = 10$ A/m^2 with randomly distributed conductivity ($\sigma = (0.3 \pm 0.01)$ S/m) on a variable conductivity background ($\sigma = (0.1 \pm 0.01)$ S/m). MREIM simulation difference image is presented in (d). The following parameters were used in simulation: $R = 5$ mm, $TR = 2$ s, $TE = 50$ ms, $N_p = 128$, $f = 20$ Hz, $df = 20$ Hz/pix, $contrast = 0$, and $\sigma_{SD} = 2$.

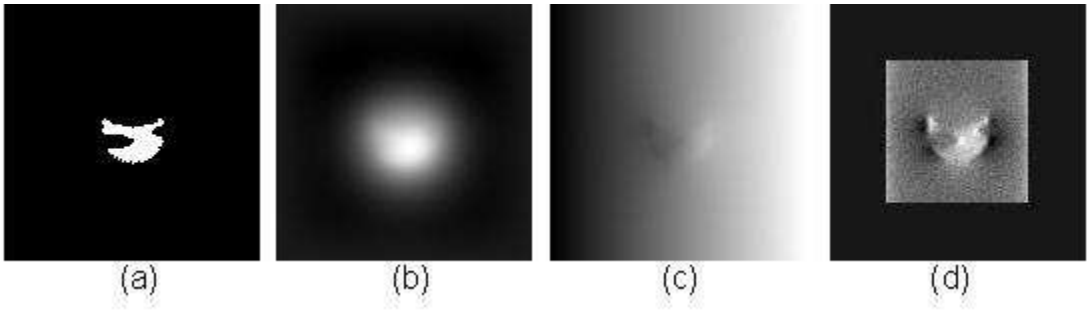

Figure 84.: Images of (a) conductivity, (b) electric potential, and (c) magnetic field strength at $z = N/2$ for an irregularly shaped cancer lesion at $i = 10$ A/m^2 with randomly distributed conductivity ($\sigma = (0.3 \pm 0.01)$ S/m) on a variable conductivity background ($\sigma = (0.1 \pm 0.01)$ S/m). MREIM simulation difference image is presented in (d). The following parameters were used in simulation: $R = 5$ mm, $TR = 2$ s, $TE = 50$ ms, $N_p = 128$, $f = 20$ Hz, $df = 20$ Hz/pix, $contrast = 0$, and $\sigma_{SD} = 2$.

radii, and conductivities are listed in Table 11. Tumor 1 and tumor 3 represent a close approximation to the conductivity of cancerous lesions according to Suroviec (Suroviec, Stuchly et al. 1988) with a higher conducting center and less conducting margins. Images of conductivity, electric potential, and aberrational magnetic field at $i = 2$ A/m^2 for the 4-tumor model are shown in Fig. 85. Corresponding MREIM images for $i = 2$ A/m^2, $f = 20.004$ Hz, $df = 20$ Hz, $\varphi \approx \pi/2$, $\sigma_{SD} = 2$, and $contrast = 0$ are shown in Fig. 85. Detectability values for tumors are as listed in Table 11: cancerous tumors 1, 2, and 3 can be detected ($d = 6.5$, $d = 8.6$, and $d = 6.4$), and the benign tumor 4 is not detectable ($d = 0.7$).

8.3.4 Summary

The values of detectability for tumors with various shapes and conductivity distribution are summarized in Table 11.

From the MREIM simulation results for numerically computed aberrational magnetic field values, the following conclusions can be drawn:

1. MREIM simulation images incorporating numerically computed aberrational magnetic field produced a perceptible effects comparable to those obtained with analytical H;

Table 10: 4-Tumor model.

Tumors	Coordinates of center	Radius, mm	Conductivity, S/m	Pathology
Tumor 1	$(N/2, N/2, N/2)$	9	1.0 ± 0.01	malignant
		6	1.5 ± 0.01	malignant
		3	2.0 ± 0.01	malignant
Tumor 2	$(N/3, N/3, N/2)$	5	2.0 ± 0.01	malignant
Tumor 3	$(2N/3, 2N/3, N/2)$	3	1.0 ± 0.01	malignant
		2	1.5 ± 0.01	malignant
		1	2.0 ± 0.01	malignant
Tumor 4	$(N/3, 2N/3, N/2)$	5	0.2 ± 0.01	benign

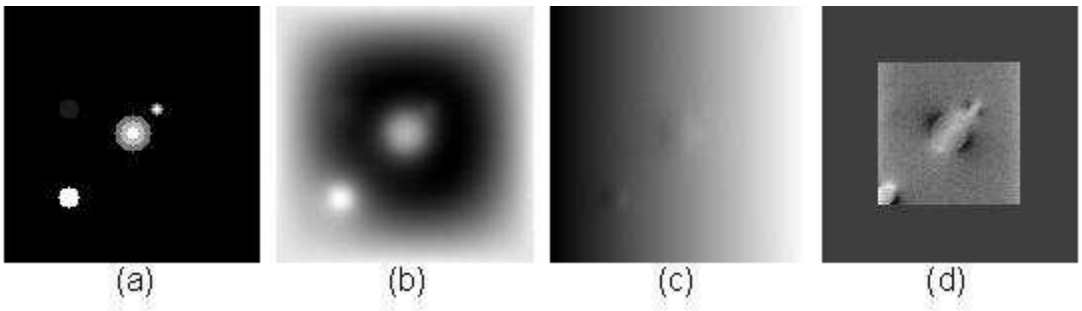

Figure 85.: Numerical simulation of a breast model with four tumors described in Table 10. Images at $z = L/2$: (a) conductivity image, (b) electric potential image, (c) aberrational magnetic field strength image, and (d) MREIM difference image at $f = 20.004$ Hz, $df = 20$ Hz, $STD_{noise} = 2$, and $contrast = 0$. Detectability values are listed in Table 11.

Table 11: MREIM difference images contrast-to-noise and detectability values for realistic tumor models.

Figs	Shape	i, A/m^2	f, Hz	df, Hz/pix	R, mm	σ_{ratio}	d
79(a)	round	10	20	20	5	3	32.5
79(b)	round	10	20	20	5	3	30.1
81	round	10	20	20	5	$\frac{0.3\pm0.01}{0.1\pm0.01}$	28.6
82	oval	10	20	20	-	$\frac{0.3\pm0.01}{0.1\pm0.01}$	25.3
83	lobular	10	20	20	-	$\frac{0.3\pm0.01}{0.1\pm0.01}$	28.4
84	irregular	10	20	20	-	$\frac{0.3\pm0.01}{0.1\pm0.01}$	24.2
85	tumor 1, round	2	20	20	< 9	$\frac{1.0\pm0.01}{0.1\pm0.01}$	6.5
					< 6	$\frac{1.5\pm0.01}{0.1\pm0.01}$	
					< 3	$\frac{2.0\pm0.01}{0.1\pm0.01}$	
85	tumor 2, round	2	20	20	5	$\frac{2.0\pm0.01}{0.1\pm0.01}$	8.6
85	tumor 3, round	2	20	20	< 3	$\frac{1.0\pm0.01}{0.1\pm0.01}$	6.4
					< 2	$\frac{1.5\pm0.01}{0.1\pm0.01}$	
					< 1	$\frac{2.0\pm0.01}{0.1\pm0.01}$	
85	tumor 4, round	2	20	20	5	$\frac{0.2\pm0.01}{0.1\pm0.01}$	0.7

discrepancies in detectability values are due to truncation errors and insufficient tolerance;

2. Effects are perceptible for a tumor model with anisotropic conductivity inside and outside the tumor; detectability value slightly dropped ($\approx 5\%$) as compared to corresponding results for a model with homogenous surrounding tissue;

3. Effects were simulated for various tumor shapes, i.e. oval, lobular, irregular, etc. Detectability for above tumor shapes decreased slightly compared to the corresponding detectability for spherical tumor;

4. Effects were simulated for 4-Tumor model consisting of spherical tumors with higher-conductivity bulk of a tumor and lower-conductivity margins. The detectability value for a tumor with $\frac{1}{r}$ conductivity behavior (tumor 1: $d = 6.5$) was found to be lower than for a tumor with randomly distributed conductivity (tumor 2: $d = 8.6$), tumor 3 with small radius $R = 3$ mm, and the conductivity gradient $\sigma_{ratio} = \frac{[1.0-2.0]\pm 0.01}{0.1\pm 0.01}$ was detected with $d = 6.4$ at the following parameters: $i = 2$ A/m^2, $f = 20$ Hz, $df = 20$ Hz, $\sigma_{SD} = 2$, and $contrast = 0$; benign tumor 4 with radius $R = 5$ mm and $\sigma_{ratio} \approx 2$ could not be detected ($d = 0.7$);

In conclusion, MREIM signal is observable for zero-contrast, low applied current, and low conductivity ratio for various shapes and conductivity distributions as long as the conductivity ratios are in the range of those for cancerous and benign lesions.

Chapter 9

MREIM Effect Enhancement: Reducing the Electrical Current and Future Directions

This Chapter discusses methods and techniques to increase the detectability of the MREIM effect. From Chapter 8, the current density limits providing visibility were to be in the range $i = 1$–2 A/m^2, which is equivalent to 10–20 mA for contact area of 10×10 cm^2. For MREIM to proceed to clinical trials, the applied electrical energy must be imperceptible to the patient and has to meet the applicable safety standard limits. The applied current amplitude should be lower than the level that can stimulate muscle or nerve tissues (AAMI 1993). The following points have to be taken into consideration:

- In our experiment, the voltage drop across the phantom was approximately 20 V, which creates an electric field of about 4 V/cm. The electric field strength is on the order of field strengths used in other experimental clinical trials for disrupting cancer cell differentiation (Miller 2007);

- The IEC 601 standard limit of applied auxiliary current is 0.1 mA at $f < 10$ Hz and 1 mA at $f > 10$ kHz (IEC 2001);

- American National Standard: safe current limits for electromedical apparatus is 0.5 mA for perceptible current (AAMI 1993);

- EIS TransScan 2000 operates at 5 mA for 47×47 mm^2, which results in an applied current density of $i = 2.26$ A/m^2. TransScan 2000 operates with up to 30 frequencies in the range from 58 Hz to 5 kHz (Scholz and Anderson 2000);

- To achieve MRI-comparable resolution in postmortem experiments on a canine head, MREIT required a minimum current of 40–50 mA (Kim, Lee et al. 2007).

Thus, it is necessary to search for sequences/methods to obtain the desired detectable MREIM cancer signature without compromising patient safety at levels of applied energy imperceptible to patient.

Based on MREIM effect analysis provided in Chapter 8, for a simple SDSE sequence, the FE effect consists in producing two aberrational images, replicas of the original image, scaled and shifted by a factor that is proportional to generator frequency and inversely proportional to frequency resolution. Since FE occurs in one direction, the FE effect in a SDSE sequence permits further optimization only by manipulation of k-space data, i.e., filtering/shifting before image reconstruction. The PE effect in SDSE sequence (sequential PE mode, sequential acquisition mode) consists in producing the shift of original image equal to $\{f \cdot TR\} \cdot N_p$ and for $TR = 2$ s is observable only at fractional frequencies. The PE effect is more pronounced at the boundaries of tumor, since the aberrational magnetic field is dependant on y at the boundaries (if PE occurs in y direction). Phase Encoding is not limited to a sequential mode; thus, more options arise to optimize PE effect. Besides, PE gradient strength varies throughout the acquisition and passes through small values of $\frac{\Delta G_y}{2} = \frac{2G_{y_{max}}}{2(N_p-1)} = \frac{2 \cdot 22}{2 \cdot (128-1)}$ mT/m = 0.17 mT/m (FE gradient is $G_x = \frac{df}{\gamma \cdot dx} = 0.47$ mT/m for $df = 20$ Hz/pix and $dx = 1$ mm). The native MR acquisition is more susceptible to magnetic field perturbations, e.g., the aberrational field gradient in $\hat{x}$ direction at $y = 0$, $G_{aber} = 0.0026$ mT/m inside the tumor and $G_{aber} = 0.00126$ mT/m outside the tumor for lowest detectable limits for MREIM signal ($\sigma_{ratio} = 3$ and $i = 2$ A/m^2) (Section 8.3.4).

This Chapter discusses different options of effect optimization by investigating various PE modes, acquisition modes, generator pulse sequence time-coupled to MR sequence, etc. The analysis is performed with simulations for the simple tumor model ($R = 5$ mm and $\sigma_{ratio} = 3$).

9.1 PE Effect Optimization

9.1.1 Phase Encode Mode

For Spin Echo sequence, there are three commonly used PE modes (Fig. 86): sequential mode (from the maximum to minimum phase encoding values, or vice versa), centric mode (from the center of k-space alternatively propagating toward the edges), and reverse centric

mode (from two edges of k-space going towards the center) (Bernstein, King et al. 2004). The Spin Density Spin Echo sequence used in our experiments was based on sequential PE mode. We simulated centric and reverse centric modes to investigate their influence on the PE effect. For $TR = 2$ s, $f = 20.004$ Hz, and $N_p = 128$, similar results to sequential PE mode were obtained (Fig. 87). For centric and reverse centric PE modes, the generalized formula for phase accumulation (Eq. (6.70)) will no longer contain p in the argument, but its scaled version, which is still an integer; thus, PE effect is periodic as well.

9.1.2 Image Acquisition Mode

Figure 88 shows difference between the algorithm for sequential and interleaved acquisition modes. In the sequential acquisition mode, multislice 2D imaging can be performed one slice at a time by acquiring all required k-space lines (one line for each PE line) for a given slice before moving to the next slice (Bernstein, King et al. 2004). If averaging is desired, it is usually performed before moving to the next PE line. Alternatively, interleaved acquisition is performed by obtaining a specific k-space line for multiple slice locations, again with the averaging done before moving to the next phase encode. The interleaved acquisition mode allows for reducing the scan time if $T_{seq} \ll TR$, where T_{seq} is the time the pulse sequence is active ($T_{seq} = TE + \frac{TS}{2}$). The number of slices that can be acquired within a TR can be obtained from $N_{slice} = [\frac{TR}{T_{seq}}]$.

Figure 89 shows the simulation result for the interleaved acquisition mode (slice 2). Since phase accumulation occurs with integer multiples of TR but shifted by constant phase angle, the effect produced by the interleaved acquisition mode is similar to sequential acquisition effect.

9.1.3 Direction of FE and PE

In the experiments and theoretical developments, PE was performed along the bore magnetic field so that PE effect perturbs mainly the regions where the aberrational magnetic field depends on y. Since the scaling factor in the aberrational replicas of original image in PE effect is A ($A_{max} = 2$) times larger than in the FE effect, an option of switching encod-

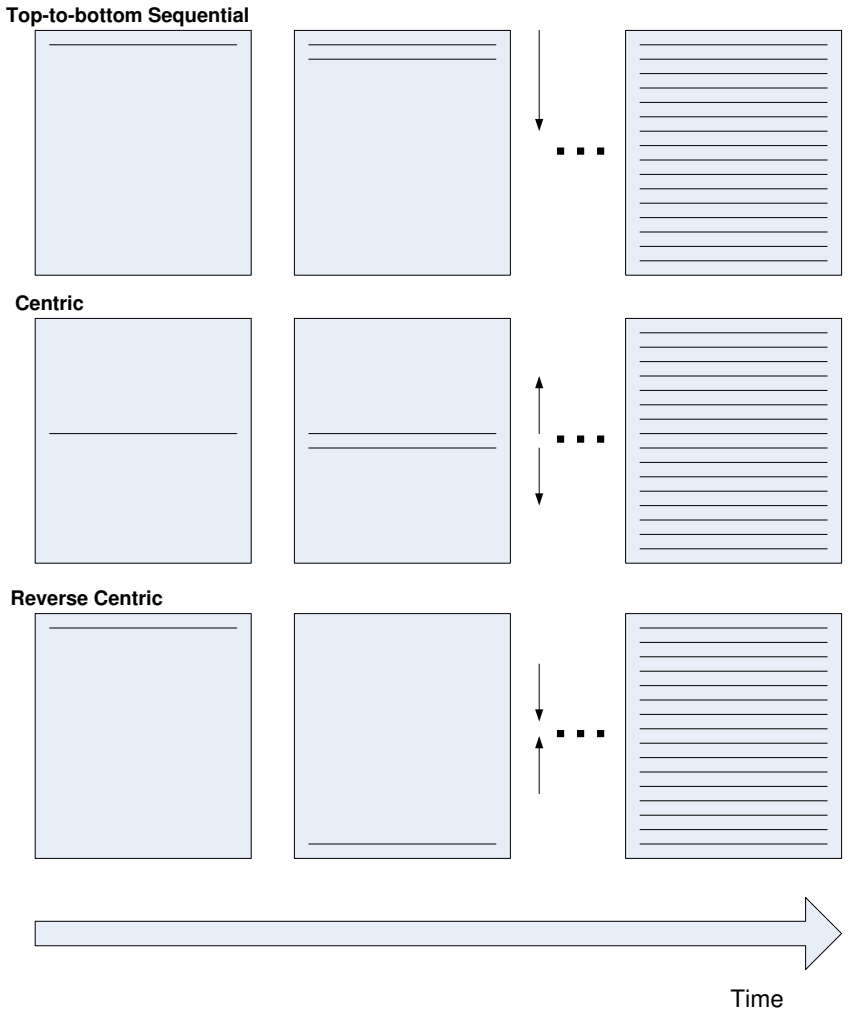

Figure 86.: Three schemes to cover a 2D rectilinear space: top-to-bottom sequential, centric ordering, and reverse centric ordering. Each box represents a 2D k-space raster. The arrows indicate the order of the k-space lines to be scanned as time progresses (adapted from Bernstein, King et al. 2004).

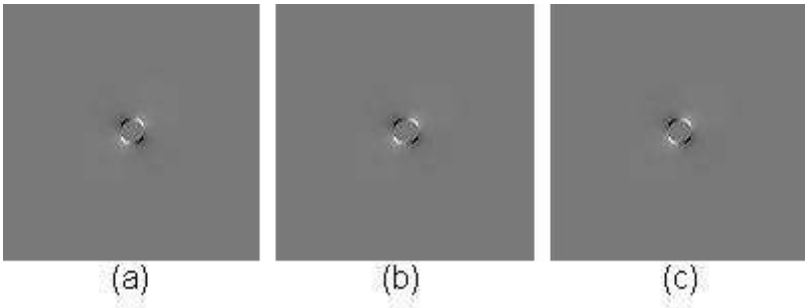

Figure 87.: MREIM difference image with PE effect only obtained for three PE modes: (a) sequential (top-to-bottom), (b) centric, and (c) reverse centric. The images were acquired with the following parameters: $TR = 2$ s, $f = 20.004$ Hz, $df = 20$ Hz/pix, $N_p = 128$, $i = 2$ A/m^2, $\sigma_{ratio} = 3$, $contrast = 0$, and $\sigma_{SD} = 0$. The PE mode does not influence appearance of the PE effect.

ing directions is investigated. Figure 90 shows the MREIM simulation images for switched encode directions (PE in the $\hat{x}$ direction, and FE in the $\hat{y}$ direction).

Figure 91 compares simulation MREIM images for $i = 2$ A/m^2, $f = 20.004$ Hz, $df = 20$ Hz/pix, $\sigma_{ratio} = 3$, $\sigma_{SD} = 2$, and $contrast = 0$ for FE in the $\hat{x}$ direction, PE in the $\hat{y}$ direction with the difference images obtained with encoding in opposite directions. The detectability value increased after switching the gradient encode directions.

9.2 Current Pulse Train Design

Figure 92 shows three cases for the sequential top-to-bottom PE mode when the signal generator is engaged for the time of the weakest PE gradient applications: (a) generator engaged for $p = 63$, $G_{y63} = 0.17$ mT/m, (b) generator engaged for $p = 64$, $G_{y64} = -0.17$ mT/m, and (c) generator engaged for both $p = 63$ and $p = 64$. It can be concluded that current can be supplied during the weakest PE gradient applications to produce observable PE effect.

In the experiments, the generator was in operation during the entire image acquisition. The phase accumulation before 180° refocusing pulse and after 180° pulse will have opposite signs. If the current is applied such that it changes polarity at 180° pulse, the phase accumulation will preserve its sign after the flip. This was implemented by a number of

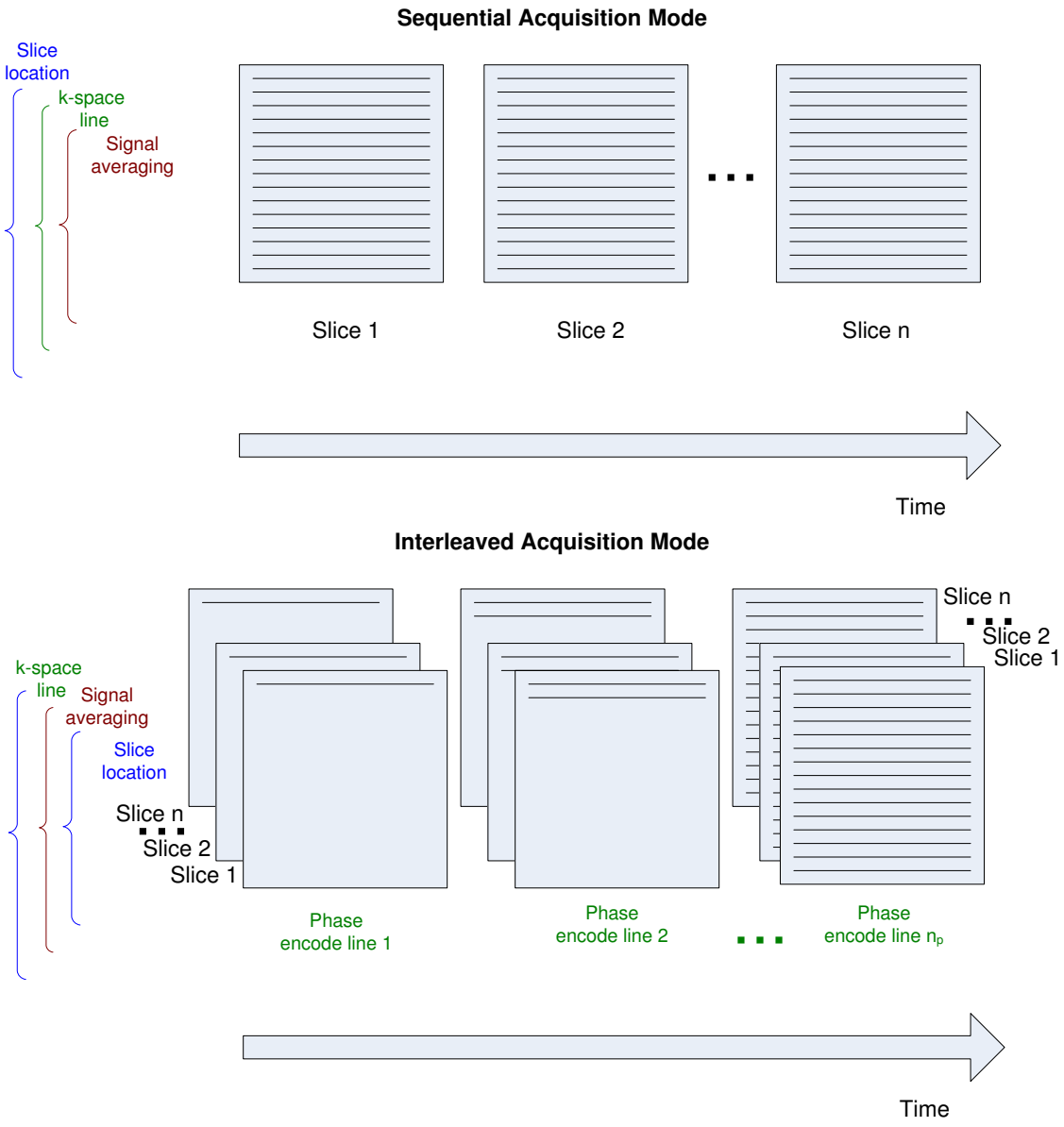

Figure 88.: Two types of acquisition for 2D imaging: sequential and interleaved. Each box represents a slice, and each line within the box denotes the k-space line (each k-space line includes the averaging, if any). The time axes are not to the same scale. The looping orders for each mode are summarized on the left (adapted from Bernstein, King et al. 2004).

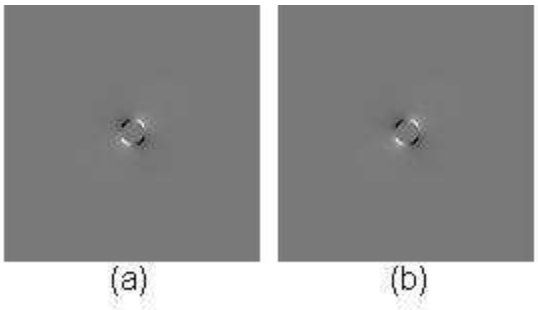

Figure 89.: MREIM difference image (with PE effect) for slice 2 acquired with (a) sequential and (b) interleaved acquisition modes. The images were acquired at the following parameters: $TR = 2$ s, $f = 20.004$ Hz, $df = 20$ Hz/pix, $N_p = 128$, $i = 2$ A/m^2, $\sigma_{ratio} = 3$, $contrast = 0$, and $\sigma_{SD} = 0$. Interleave acquisition mode does not influence PE effect appearance.

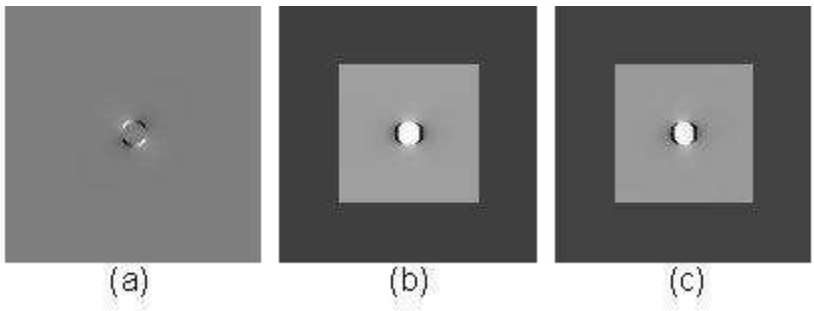

Figure 90.: MREIM simulation difference images for switched direction of encoding for PE and FE effects: (a) FE effect along $\hat{y}$, $CNR = 0.019$, (b) PE effect along $\hat{x}$, $CNR = 45.98$, (c) PE + FE, $CNR = 45.7$. The images were acquired at the following parameters: $TR = 2$ s, $f = 20.004$ Hz, $df = 20$ Hz/pix, $N_p = 128$, $i = 2$ A/m^2, $\sigma_{ratio} = 3$, $contrast = 0$, and $\sigma_{SD} = 0$.

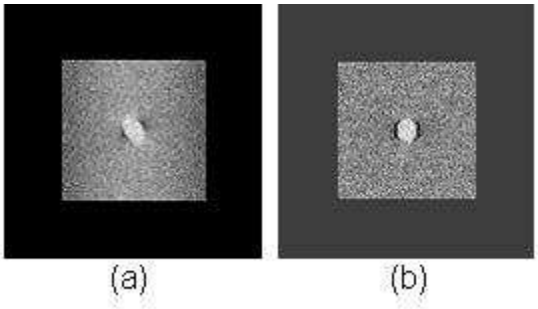

Figure 91.: MREIM simulation difference images for switched direction of encoding for PE and FE effects compared with images obtained with conventional encoding direction used for experiments: (a) FE effect along $\hat{x}$, PE effect along $\hat{y}$, $d = 4.54$, (b) PE effect along $\hat{x}$, FE effect along $\hat{y}$, $d = 12.84$. The images were acquired at the following parameters: $TR = 2$ s, $f = 20.004$ Hz, $df = 20$ Hz/pix, $N_p = 128$, $i = 2$ A/m^2, $\sigma_{ratio} = 3$, $contrast = 0$, and $\sigma_{SD} = 2$.

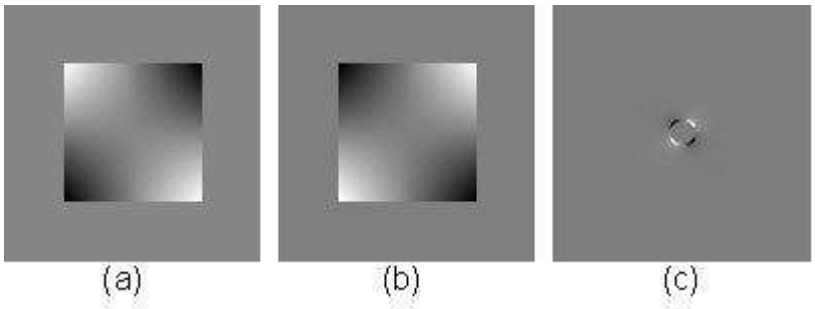

Figure 92.: MREIM simulation difference images for current pulse sequence that is active only for the weakest PE gradient application: (a) $p = 63$, $G_{y_{63}} = 0.17$ mT/m,(b) $p = 64$, $G_{y_{64}} = -0.17$ mT/m, and (c) $p = 63$ and $p = 64$. Top-to-bottom sequential PE mode was used. The images were acquired at the following parameters: $TR = 2$ s, $f = 20.004$ Hz, $df = 20$ Hz/pix, $N_p = 128$, $i = 2$ A/m^2, $\sigma_{ratio} = 3$, $contrast = 0$, and $\sigma_{SD} = 0$.

authors studying MRI of currents (Scott, Joy et al. 1991; Mikac, Demsar et al. 2001) and MREIT (Khang, Lee et al. 2002; Lee, Oh et al. 2003; Gao, Zhu et al. 2006; Kim, Lee et al. 2007). Some examples of sequences used are provided in Figs. 93–96(a).

A generator frequency of $f \approx 20$ Hz can be considered as the one providing two DC electric pulses that change polarity at the 180° RF pulse, since $\frac{TE}{2} = \frac{0.05}{2}$ s $= \frac{1}{2}(\frac{1}{f}) = \frac{1}{2}T_i$, where T_i is the period of signal generator pulse.

To investigate the MREIM effect for higher alternating frequencies, a pulse technique developed by Mikac et al. is suggested (Mikac, Demsar et al. 2001) (Fig. 96(b)). Using the same principle of approximating AC with a changing-polarity DC pulse, inserting refocusing RF pulses between each pair of electric pulses of opposite polarity will enable constructive accumulation phase shifts, and, in principle, should produce more conspicuous effect in PE.

There is an option of starting a current pulse with a different initial phase angle with each TR (initial phase angle φ_0 is dependant on p). Figure 97 shows how MREIM difference images change with adding PE dependant initial phase to current waveform. For example, for $\varphi_0 = \frac{\pi}{2} \cdot p$, where φ_0 goes through the cycle of $0, \frac{\pi}{2}, \pi, \frac{3\pi}{2}, 2\pi$. The difference image, if properly shifted, can produce a pronounced signal from a higher conducting region.

9.3 Suggested MREIM Protocol

Based on the MREIM effect analysis from previous sections, we suggest an MREIM protocol that consists of a combination of an MRI sequence and a current pulse train time-coupled to the MR image acquisition. A schematic diagram of the suggested MREIM sequence is presented in Fig. 98. The following parameters and encode directions should be used for the SDSE sequence combined with a time-coupled current pulse train:

- For sagittal slices: slice encode in the $\hat{z}$ direction (along applied electric field), FE encode in the $\hat{y}$ direction (along the bore field), and PE encode in the $\hat{x}$ direction;
- $TR = 2$ s;
- $TE = 50$ ms;
- $N_p = 128$;

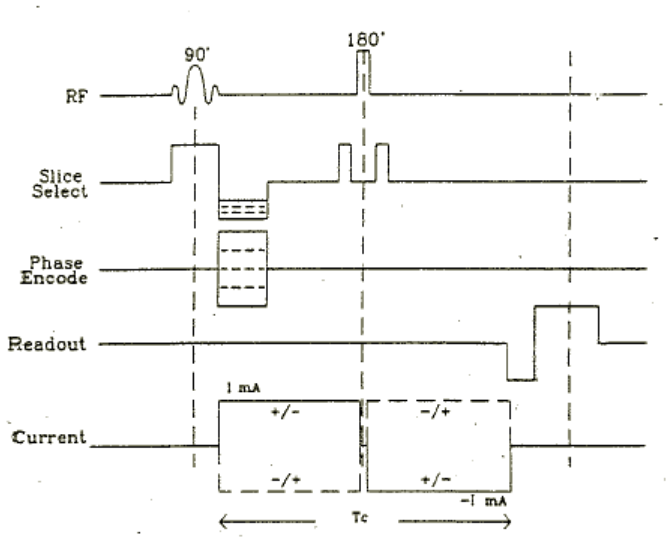

Figure 93.: The current density imaging sequence developed by Scott et al. (Scott, Joy et al. 1991). The DC current pulse is bipolar so that the phase shifts it produces are not canceled out by the non selective 180° pulse (from Scott, Joy et al. 1991).

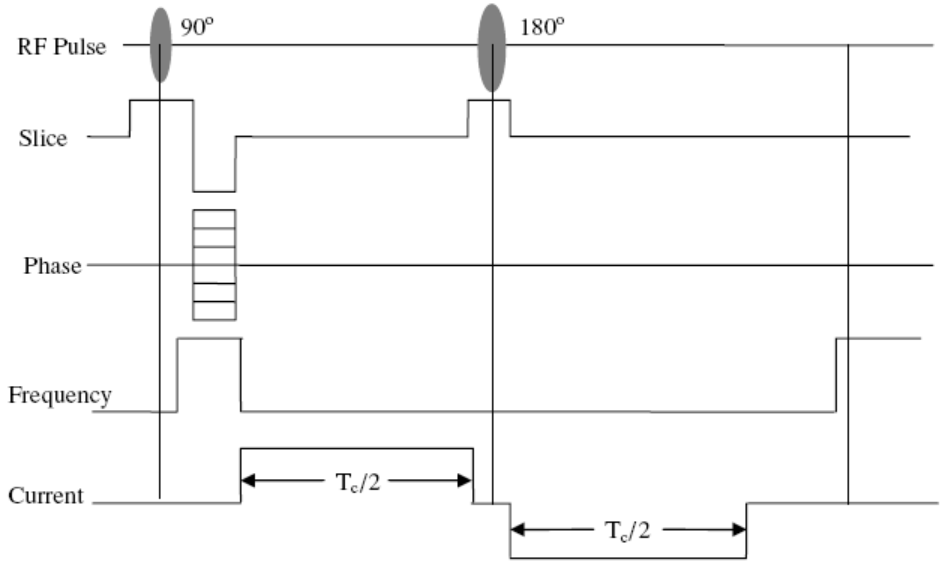

Figure 94.: Rectangular bipolar current used in MREIT (from Gao, Zhu et al. 2006). The bipolar rectangular current $I = 4$ mA, $T_c = 50$ ms, $f = \frac{1}{T_c} = 20$ Hz is injected into the human head through the pairs of scalp electrodes.

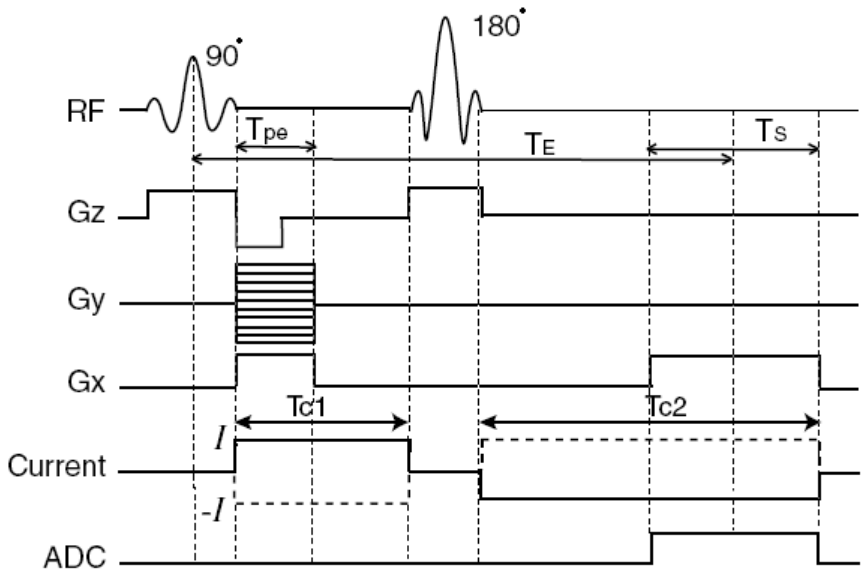

Figure 95.: Injection Current Nonlinear Encoding pulse sequence for MREIT (from Kim, Lee et al. 2007). Note that current pulse is applied during FE as well.

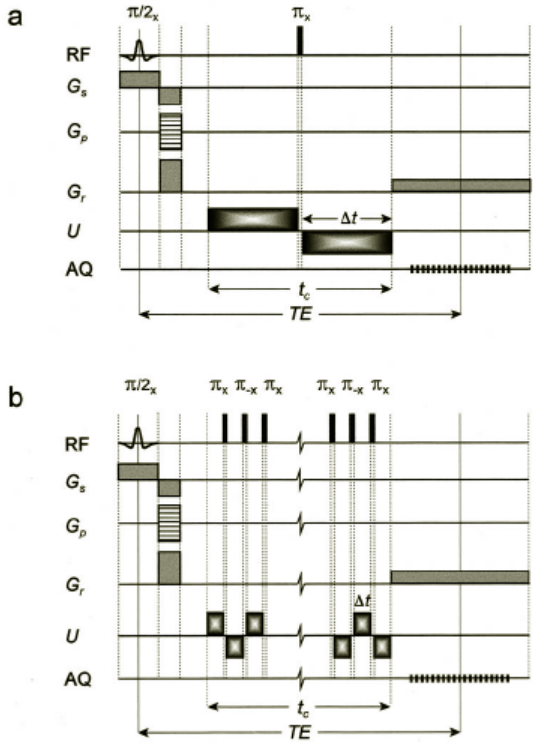

Figure 96.: (a) Direct current density imaging sequence (DC-CDI) and (b) alternating current density imaging sequence (AC-CDI) (from Mikac, Demsar et al. 2001). AC-CDI has a block of $(N-1)\pi$ pulses of alternating phase, which is inserted between N alternating electric pulses. A spin-echo is formed after the AC-CDI sequence only when N is even.

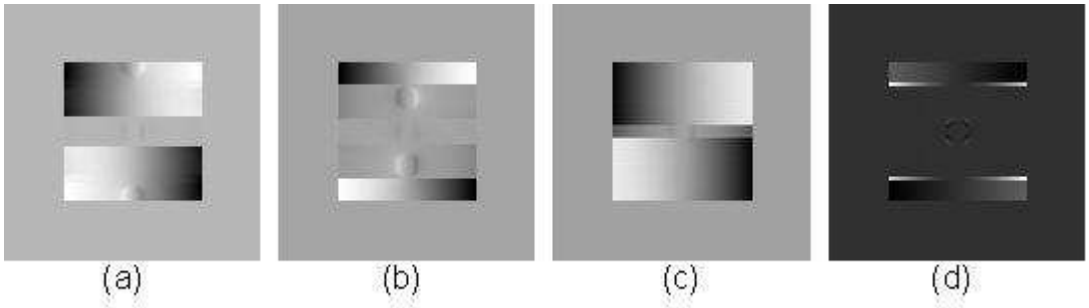

Figure 97.: MREIM simulation difference images for initial phase angle dependant on p: (a) $\varphi_0(p) = \frac{\pi}{2} \cdot p$, (b) $\varphi_0(p) = \frac{\pi}{4} \cdot p$, (c) $\varphi_0(p) = \frac{3\pi}{2} \cdot p$, and (d) $\varphi_0(p) = \pi \cdot p$. The images were acquired at the following parameters: $TR = 2$ s, $f = 20.004$ Hz, $df = 20$ Hz/pix, $N_p = 128$, $i = 2$ A/m^2, $\sigma_{ratio} = 3$, $contrast = 0$, and $\sigma_{SD} = 0$.

- $df = 20$ Hz/pix;

- $f = 20.004$ Hz/pix (sets the quasi-DC bipolar current pulse changing polarity at 180° RF pulse.

In general, the generator frequency should be chosen such that polarity of applied current flips at 180° refocusing pulse at $t = \frac{TE}{2}$; thus, $TE = \frac{1}{f}$. Also, f should be chosen such that $\{TR \cdot f\} \cdot N_p = 1$. If there is a need to use higher frequencies, the pulse suggested by Mikac et al. (Mikac, Demsar et al. 2001) should be used.

Applied current limits are found using the contrast diagram for three tumor radii, $R = 5$, 2.5, and 1.5 mm with conductivity ratio of $\sigma_{ratio} = \frac{0.3 \pm 0.01}{0.1 \pm 0.01}$. The minimum current allowing for MREIM effect visibility was found to be $i = 0.4$ A/m^2 for $R = 5$ mm and $i \approx 0.5$ A/m^2 for $R = 2.5$ and 1.5 mm, which is equivalent to the range of 4–5 mA for 10×10 cm^2 breast-FSs contact area.

Figure 100 shows the simulation difference images obtained with the lowest current limits at which MREIM is still detectable. The images were generated following the protocol suggested above.

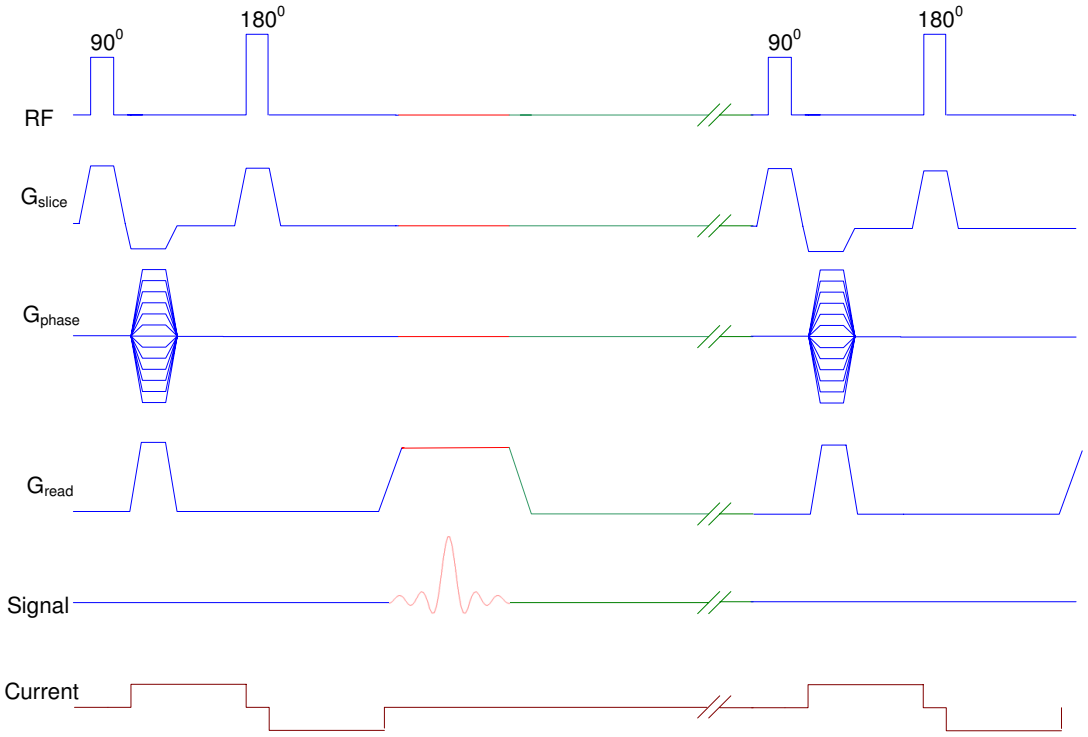

Figure 98.: A schematic diagram of suggested MREIM sequence.

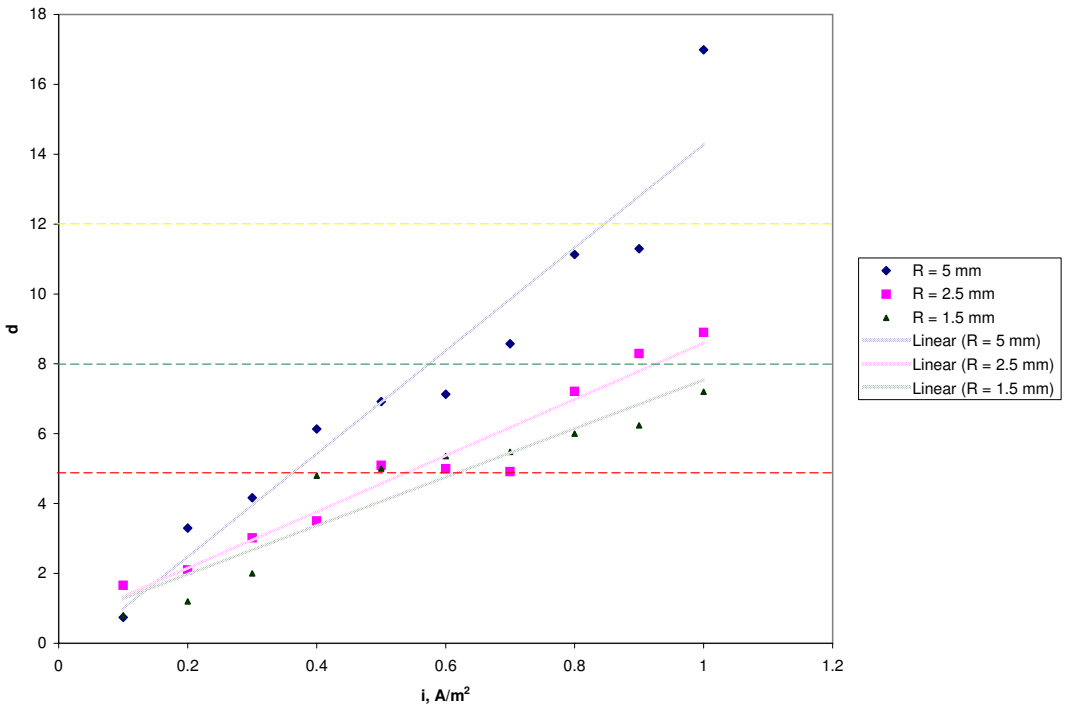

Figure 99.: Dependence of detectability of MREIM signal produced by suggested MREIM sequence on applied current for $R = 5$, 2.5, and 1.5 mm. The following parameters were used: $f = 20.004$ Hz, $df = 20$ Hz/pix, $contrast = 0$, $\sigma_{ratio} = \frac{0.3 \pm 0.01}{0.1 \pm 0.01}$, and $\sigma_{SD} = 2$. Dotted colored lines denote (red) visibility threshold, (green) detection threshold, and (yellow) shape outline threshold.

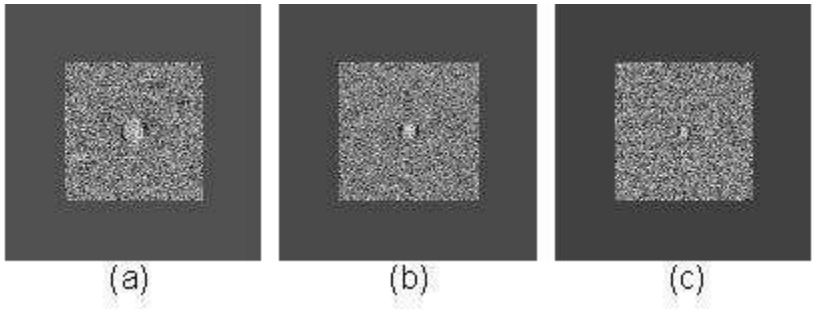

Figure 100.: MREIM simulation difference images obtained using suggested protocol for the lowest current limits permitting MREIM effect visibility: (a) $R = 5$ mm, $i = 0.4$ A/m^2, $d = 6.1$, (b) $R = 2.5$ mm, $i = 0.5$ A/m^2, $d = 5.1$, and (c) $R = 1.5$ mm, $i = 0.5$ A/m^2, $d = 5.0$. The images were acquired at the following parameters: $TR = 2$ s, $f = 20.004$ Hz, $df = 20$ Hz/pix, $N_p = 128$, $\sigma_{ratio} = \frac{0.3\pm0.01}{0.1\pm0.01}$, $contrast = 0$, and $\sigma_{SD} = 2$.

9.4 Further Suggestions

MREIM effect optimization was performed using a simple SDSE sequence. The algorithm of MREIM sequence optimization can be applied for various MRI sequences including Echo Planar Imaging (EPI), Gradient Spin Echo (GSE), FLASH, etc. Also, there is an option of raw data analysis and, possibly, manipulations. The following suggestions should be considered:

- Half-Fourier Imaging Phase Correction Method

  The MREIM aberrational field distorts the symmetry of k-space data by accumulating phase. This phase accumulation can be found using phase data estimation as in Half-Fourier imaging (Bernstein, King et al. 2004).

  Half-Fourier imaging was developed based on the fact that for real function $\rho(x)$, its frequency representation $S(k)$ is redundant due to its Hermitian symmetry. Instead of acquiring all k-space lines, only $-n_0 \leq n < N$ lines are acquired, where $n_0 \ll N$, and typically equals to $n_0 = 16$ for 128×128 image matrix.

  In practice, however, the Hermitian symmetry of raw data is violated due to object motion and magnetic field inhomogeneities (Bernstein, King et al. 2004). In half-Fourier imaging, addition of a non-zero phase $\varphi(x)$ to image function is corrected by extracting

the symmetric k-space data from the center of k-space, filtering it with Hamming filter (low-pass filter) so that the extracted filtered data is $S^{'}(n) = S(n)(0.45 + 0.46 \cdot cos\frac{n\pi}{n_0})$, where $-n_0 \leq n < n_0$ (Bernstein, King et al. 2004). Then the phase estimate can be found from phase data after Fourier transformation.

- White-Marker Imaging (Seppenwoolde, Vincken et al. 2007)

- Estimation of phase accumulation due to magnetic field inhomogeneities in: GSE (Reichenbach, Venkatesan et al. 1997), EPI (Stevick, Harding et al. 2008), FLASH (Frahm, Merboldt et al. 1988), etc.

Chapter 10

Conclusion

Theory, simulation, and experimental phantom imaging results presented in this work supply strong evidence that MREIM can provide a differential signal based on electrical conductivity differences and that the effect is observable in the magnitude image data.

As MREIM is based on the conductivity differences between malignant and normal breast tissue, a review of the electric properties of the breast tissue was provided in the form of a survey that can be used as a reference for further development of bio-impedance based applications (Heine, Kovalchuk et al. 2008a). Although the conductivity ratio between cancerous and normal breast tissue varies in the range of 3–40 (Chapter 3), extensive in-vivo research is required at the lower frequencies to specify the conductive properties of breast tissue in the MREIM application ranges.

A novel breast phantom was designed and developed, and phantom MREIM imaging tests were conducted. The custom-made phantom realistically reproduced malignancy and normal breast tissue in terms of conductive properties and relative signal intensities in MREIM images. The MREIM apparatus was able to validate the MREIM theory producing the MR magnitude images with the differential signature of a higher-conducting cancer surrogate (Heine, Kovalchuk et al. 2008b).

A MREIM simulation program was developed. Using this program, the experimental phantom imaging results were replicated and explained by supporting theoretical developments.

A method for calculation of electric potential and induced magnetic field distribution in objects with realistic tumor shapes and anisotropic conductivities was developed. The simulation based on the developed method showed that the MREIM signal is detectable for tumors with realistic shapes and conductivity distributions. The MREIM effect detectabil-

ity value for anisotropic conductivity distribution decreased by 5% compared to isotropic conductivity for a spherical tumor.

MREIM effects were investigated using a contrast diagram method. An MREIM sequence protocol that produces a detectable MREIM effect at the lowest applied electric energy was suggested. According to simulation results, utilizing this protocol, the minimum applied current at which a detectable MREIM effect for a 3 mm-diameter tumor is found to be 0.5 A/m^2, which meets safety standards.

To produce a clinically viable MREIM product, a significant effort should be put into further optimization of imaging sequences (EPI, GSE, FLASH, RODEO, etc.) at minimum current without compromising patient safety or signal quality. Optimization of the hardware includes: (a) a temporally stable and more sophisticated phantom containing various breast abnormalities, (b) MR-compatible power supplies and Faraday shields incorporated in commercially available MR systems. In future work, prototype FSs components and power supply, including all connecting hardware, should be professionally manufactured to meet both MR safety and clinical patient-safety standards. This equipment will permit more exact testing that will lead to clinical human-subject experimentation to validate MREIM applicability.

In the work presented here, the magnitude data was analyzed, because the phase data was not accessible. Future work should investigate phase contrast with the phase data as well as magnitude contrast.

The work on the Magnetic Resonance Electrical Impedance Mammography project has resulted in patent application, publications, presentations, and abstracts (Wollin 2004; Kovalchuk, Kallergi et al. 2006; Kallergi, Wollin et al. 2006a; Kallergi, Wollin et al. 2006b; Heine, Kovalchuk et al. 2008a; Heine, Kovalchuk et al. 2008b).

References

AAMI 1993 *American National Standard: Safe Current Limits for Electromedical Apparatus* (Document ANSI/AAMI ES1 - 1993)

Ackmann J J and Seitz M A 1984 Methods of complex impedance measurements in biologic tissue *Crit Rev Biomed Eng* **11** 281-311

Adams S V, Orton P Z and Scott V 2001 *Cliffs Quick Review: Statistics* (New York, New York: Wiley Publishing, Inc.)

Assenheimer M, Laver-Moskovitz O, Malonek D, Manor D, Nahaliel U, Nitzan R and Saad A 2001 The T-SCAN technology: electrical impedance as a diagnostic tool for breast cancer detection *Physiol Meas* **22** 1-8

Bernstein M A, King K F and Zhou Z J 2004 *Handbook of MRI pulse sequences* (Amsterdam; Boston: Academic Press)

Beutel J, Kundel H L, and Van Metter R L 2000 *Handbook of Medical Imaging: Volume 1. Physics and Psychophysics* (Bellingham, Washigton: SPIE Press)

Binns K J, Lawrenson P J and Trowbridge C W 1992 *The analytical and numerical solution of electric and magnetic fields* (Chichester [England]; New York: Wiley)

Birgul O and Eyuboglu B M 2003 Experimental results for 2D magnetic resonance electrical impedance tomography (MR-EIT) using magnetic flux density in one direction *Phys Med Biol* **48** 3485-504

Birgul O, Eyuboglu B M and Ider Y Z 2001 New technique for high resolution absolute conductivity imaging using magnetic resonance electrical impedance tomography (MR-EIT) *SPIE Physics of Medical Imaging* **2** 880-8

Birgul O, Eyuboglu B M and Ider Y Z 2003 Current constrained voltage scaled reconstruction (CCVSR) algorithm for MR-EIT and its performance with different probing current patterns *Physics in medicine and biology* **48** 653-71

Birgul O and Ider Y Z 1995 Use of magnetic field generated by the internal distribution of injected currents for electrical impedance tomography. In: *IXth Int Conf on Bio-Impedance,* pp 418-9

Bloch F, Hansen W W and Packard M 1946 Nuclear induction *Phys Rev* **69** 127

Breast Cancer Facts and Figures 2007-2008 (Atlanta: American Cancer Society, Inc.)

Breast Imaging Reporting and Data System (BI-RADS) Atlas 2007 (Reston, VA: American College of Radiology)

Brigham E O 1988 *The fast Fourier transform and its applications* (Englewood Cliffs, N.J.: Prentice Hall)

Bright D S, Newbury D E and Steel E B 1997 Visibility of objects in computer simulations of noisy micrographs *J Microscopy* **189** 25-42

Charman R A 1996 *Clayton's Electrotherapy,* ed S Kitchen, Bazin, S. (London, UK: Saunders Company Ltd.)

Chauveau N, Hamzaoui L, Rochaix P, Rigaud B, Voigt J J and Morucci J P 1999 Ex vivo discrimination between normal and pathological tissues in human breast surgical biopsies using bioimpedance spectroscopy *Ann N Y Acad Sci* **873** 42-50

Chen X, Lehman C D and Dee K E 2004 MRI-guided breast biopsy: clinical experience with 14-gauge stainless steel core biopsy needle *AJR Am J Roentgenol* **182** 1075-80

Cherepenin V, Karpov A, Korjenevsky A, Kornienko V, Mazaletskaya A, Mazourov D and Meister D 2001 A 3D electrical impedance tomography (EIT) system for breast cancer detection *Physiological measurement* **22** 9-18

Cherepenin V A, Karpov A Y, Korjenevsky A V, Kornienko V N, Kultiasov Y S, Ochapkin M B, Trochanova O V and Meister J D 2002 Three-dimensional EIT imaging of breast

tissues: system design and clinical testing *IEEE transactions on medical imaging* **21** 662-7

Cole K S 1928 Electric impedance of suspensions of spheres *J. Gen. Physiol.* **12** 29-36

Cole K S 1932 Electric phase angle of cell membranes *J. Gen. Physiol.* **15** 641-9

Cole K S and Cole R H 1941 Dispersion and absorption in dielectrics. I. Alternating current *J. Chem. Phys.* **9** 341-51

Cone C D, Jr. 1970 Variation of the transmembrane potential level as a basic mechanism of mitosis control *Oncology* **24** 438-70

Cone C D, Jr. 1974 The role of the surface electrical transmembrane potential in normal and malignant mitogenesis *Ann N Y Acad Sci* **238** 420-35

Cone C D, Jr. 1985 *Transmembrane Potential and Characteristics of Immune and Tumor Cells* (Boca Raton, Florida: CRC Press)

Cope F W 1978 A medical application of the Ling association-induction hypothesis: the high potassium, low sodium diet of the Gerson cancer therapy *Physiol Chem Phys* **10** 465-8

Cure J C 1991 Cancer: an electrical phenomenon. *Resonant* **1**

Diebold T, Jacobi V, Scholz B, Hensel C, Solbach C, Kaufmann M, Viana F, Balzer J, Peters J and Vogl T 2005 Value of electrical impedance scanning (EIS) in the evaluation of BI-RADS III/IV/V-lesions *Technology in cancer research & treatment* **4** 93-7

Duchesne N, Burbank F and Duchesne S eds 2006 *Breast Diseases: Detection, Intervention, and Therapy* (St. Bruno, Canada: DTR Inc.)

Esserman L, Hylton N, Yassa L, Barclay J, Frankel S and Sickles E 1999 Utility of magnetic resonance imaging in the management of breast cancer: evidence for improved preoperative staging *J Clin Oncol* **17** 110-9

Eyübolu B M, Leigh J S and Reddy R 2002 Magnetic resonance-electrical impedance tomography. (US: 6397095)

F-D-C Reports 1998 *The Grey Sheet, Medical Devices, Diagnostics & Instrumentation* **24**

Fitzpatrick R 1996 Advanced Classical Electromagnetism (Austin: The University of Texas)

Foster K R and Schepps J L 1981 Dielectric properties of tumor and normal tissues at radio through microwave frequencies *J Microw Power* **16** 107-19

Foster K R and Schwan H P 1989 Dielectric properties of tissues and biological materials: a critical review *Crit Rev Biomed Eng* **17** 25-104

Frahm J, Merboldt K D and Hanicke W 1988 Direct FLASH MR Imaging of Magnetic Field Inhomogeneities by Gradient Compensation *Magnetic Resonance in Medicine* **6** 474-480

Fricke H and Morse S 1926 The electric capacity of tumors of the breast *J. Cancer Res.* **10** 340-76

Gabriel C 1996 Compilation of the dielectric properties of body tissues at RF and microwave frequencies. In: *Occupational and environmental health directorate, Radiofrequency Radiation Division,* (Texas (USA): Brooks Air Force Base)

Gao N, Zhu S A, He B 2006 A new magnetic resonance electrical impedance tomography (MREIT) algorithm: the RSM-MREIT algorithm with applications to estimation of human head conductivity *Phys Med Biol* **51** 3067-83

Glickman Y A, Filo O, Nachaliel U, Lenington S, Amin-Spector S and Ginor R 2002 Novel EIS postprocessing algorithm for breast cancer diagnosis *IEEE transactions on medical imaging* **21** 710-2

Haake E M, Brown R W, Thompson M R, Venkatesan R 1999 *Magnetic Resonance Imaging: Physical Principles and Sequence Design* (New York: Wiley)

Heine J J 1993 Computer Simulations of Magnetic Resonance Imaging and Spectroscopy. In: *Physics Department* (Tampa: University of South Florida)

Heine J J, Kovalchuk N and Wollin E 2008a (under review in Medical Physics) Magnetic Resonance Electrical Impedance Mammography Part2: Tissue models and field equations

Heine J J, Kovalchuk N, Manohar A, Kallergi M, and Wollin E and Wollin E 2008b (under review in BioMedical Engineering Online) Magnetic Resonance Electrical Impedance Mammography

Heywang S H, Viehweg P and Heining A 1997 Contrast enhanced MRI of breast: Accuacy, value, solutions *Europ J Radiol* **24** 94-108

Ider Y Z and Muftuler L T 1997 Measurement of AC magnetic field distribution using magnetic resonance imaging *IEEE transactions on medical imaging* **16** 617-22

IEC 2001 *International Standard: Medical Electrical Equipment - Part 1-2: General Requirements for Safety* (Document IEC 60601-1-2)

Jossinet J 1996 Variability of impedivity in normal and pathological breast tissue *Med Biol Eng Comput* **34** 346-50

Jossinet J 1998 The impedivity of freshly excited human breast tissue *Physiol Meas* **19** 61-75

Jossinet J and Schmitt M 1999 A review of parameters for the bioelectrical characterization of breast tissue *Ann N Y Acad Sci* **873** 30-41

Kahan W 1958 Gauss-Seidel methods of solving large systems of linear equations In: *PhD Thesis* (Toronto: University of Toronto)

Kallergi M, Wollin E, Heine J J, Kovalchuk N and Manohar A 2006a *Lecture Notes in Computer Science,* (Berlin/Heidenberg: Springer) pp 468-74

Kallergi M, Wollin E, Heine J J, Kovalchuk N and Manohar A 2006b Magnetic Resonance Electrical Impedance Mammography: A Pilot Study. In: *8th IWDM,* ed S Astley*, et al.* (Manchester, UK: Springer-Verlag)

Khang H S, Lee B I, Oh S H, Woo E J, Lee S Y, Cho M H, Kwon O, Yoon J R and Seo J K 2002 J-substitution algorithm in magnetic resonance electrical impedance tomography (MREIT): phantom experiments for static resistivity images *IEEE Trans Med Imaging* **21** 695-702

Kim H J, Lee B I, Cho Y, Kim Y T, Kang B T, Park H M, Lee S Y, Seo J K and Woo E J 2007 Conductivity imaging of canine brain using a 3 T MREIT system: postmortem experiments *Physiological Measurements* **28** 1341-53

Kneeshaw P J, Drew P J and Hubbard A 2002 Electrical impedance scanning: a new imaging technique for evaluating microcalcifications in the breast? *Breast Cancer Res* **4** 20

Kovalchuk N, Kallergi M, Wollin E, Heine J J, Manohar A and Rabson D 2006 Magnetic Resonance Electrical Impedance Mammography: A Feasibility Study. In: *48th Annual Meeting AAPM,* (Orlando, US: Med. Phys.) p 2183

Kraft K A, Fatouros P P, Clarke G D and Kishore P R 1987 An MRI phantom material for quantitative relaxometry *Magn Reson Med* **5** 555-62

Kwon O, Woo E J, Yoon J R and Seo J K 2002 Magnetic resonance electrical impedance tomography (MREIT): simulation study of J-substitution algorithm *IEEE Trans Biomed Eng* **49** 160-7

Lee J W, Kim D M, Lim H G, Park I Y and Cho JH 2002 A characteristics of human skin impedance including at biological active points *ITC-CSCC-2002*

Lee B I, Oh S H, Woo E J, Lee S Y, Cho M H, Kwon O, Seo J K, Back W S 2003 Static resistivity image of cubic saline phantom in magnetic resonance electrical impedance tomography (MREIT) *Physiol Meas* **24** 579-89

Liney G P, Tozer D J and Turnbull L W 1999 A simple and realistic tissue-equivalent breast phantom for MRI *J Magn Reson Imaging* **10** 968-71

Macdonald J R 1987 *Impedance Spectroscopy: Emphasizing Solid Materials and Systems* (New York: Wiley)

Madsen E L and Fullerton G D 1982 Prospective tissue-mimicking materials for use in NMR imaging phantoms *Magn Reson Imaging* **1** 135-41

Malich A, Boehm T, Facius M, Freesmeyer M G, Fleck M, Anderson R and Kaiser W A 2001a Differentiation of mammographically suspicious lesions: evaluation of breast ultrasound,

MRI mammography and electrical impedance scanning as adjunctive technologies in breast cancer detection *Clinical radiology* **56** 278-83

Malich A, Bohm T, Facius M, Freessmeyer M, Fleck M, Anderson R and Kaiser W A 2001b Additional value of electrical impedance scanning: experience of 240 histologically-proven breast lesions *Eur J Cancer* **37** 2324-30

Malich A, Bohm T, Facius M, Kleinteich I, Fleck M, Sauner D, Anderson R and Kaiser W A 2003 Electrical impedance scanning as a new imaging modality in breast cancer detection - a short review of clinical value on breast application, limitations and perspectives *Nuclear Instruments and Methods in Physics Research A* **497** 71-81

Malich A, Fritsch T, Anderson R, Boehm T, Freesmeyer M G, Fleck M and Kaiser W A 2000 Electrical impedance scanning for classifying suspicious breast lesions: first results *European radiology* **10** 1555-61

Martin G, Martin R, Brieva M J and Santamaria L 2002 Electrical impedance scanning in breast cancer imaging: correlation with mammographic and histologic diagnosis *European radiology* **12** 1471-8

McAdams E T and Jossinet J 1995 Tissue impedance: a historical overview *Physiol Meas* **16** A1-13

Melloul M, Paz A, Ohana G, Laver O, Michalevich D, Koren R, Wolloch Y and Gal R 1999 Double-phase 99mTc-sestamibi scintimammography and trans-scan in diagnosing breast cancer *J Nucl Med* **40** 376-80

Mikac U, Demsar F, Beravs K and Sersa I 2001 Magnetic resonance imaging of alternating electric currents *Magnetic resonance imaging* **19** 845-56

Miller J 2007 Electric fields have potential as a cancer treatment. In: *Physics Today,* pp 19-20

Mitra A K 2007 Finite Difference Method for the Solution of Laplace Equation [*www.public.iastate.edu/ akmitra/aero*361/*designweb/Laplace.pdf*]

Morimoto T, Kimura S, Konishi Y, Komaki K, Uyama T, Monden Y, Kinouchi Y and Iritani T 1993 A study of the electrical bio-impedance of tumors *J Invest Surg* **6** 25-32

Morimoto T, Kinouchi Y, Iritani T, Kimura S, Konishi Y, Mitsuyama N, Komaki K and Monden Y 1990 Measurement of the electrical bio-impedance of breast tumors *Eur Surg Res* **22** 86-92

Morris E A ed 2006 *Breast MRI* (St. Bruno: DTR Inc.)

Morris P G 1986 *Nuclear magnetic resonance imaging in medicine and biology* (Oxford: Oxford University Press)

Morucci J P, Valentinuzzi M E, Rigaud B, Felice C J, Chauveau N and Marsili P M 1996 Bioelectrical impedance techniques in medicine *Crit Rev Biomed Eng* **24** 275

Muftuler L T, Hamamura M, Birgul O and Nalcioglu O 2004 Resolution and contrast in magnetic resonance electrical impedance tomography (MREIT) and its application to cancer imaging *Technology in cancer research & treatment* **3** 599-609

Nieper H A 1985 *Dr. Nieper's Revolution in Technology, Medicine and Society* (Oldenburg, Germany: MIT Verlag)

Oh S H and Han J Y 2003 Electrical conductivity imaging by magnetic resonance electrical impedance tomography (MREIT) *Magn Reson Med* **50** 875-8

Oh S H, Lee B I, Park T S, Lee S Y, Woo E J, Cho M H, Seo J K and Kwon O 2004 Magnetic resonance electrical impedance tomography at 3 Tesla field strength *Magn Reson Med* **51** 1292-6

Oh S H, Lee B I, Woo E J, Lee S Y, Cho M H, Kwon O and Seo J K 2003 Conductivity and current density image reconstruction using harmonic Bz algorithm in magnetic resonance electrical impedance tomography *Phys Med Biol* **48** 3101-16

Ohmine Y, Morimoto T, Kinouchi Y, Iritani T, Takeuchi M and Monden Y 2000 Noninvasive measurement of the electrical bioimpedance of breast tumors *Anticancer Res* **20** 1941-6

Perlet C, Kessler M, Lenington S, Sittek H and Reiser M 2000 Electrical impedance measurement of the breast: effect of hormonal changes associated with the menstrual cycle *Eur Radiol* **10** 1550-4

Piperno G, Frei E H and Moshitzky M 1990 Breast cancer screening by impedance measurements *Front Med Biol Eng* **2** 111-7

Piperno G and Lenington S 2002 Breast electrical impedance and estrogen use in postmenopausal women *Maturitas* **41** 17-22

Polk C and Postow W eds 1986 *CRC Handbook of Biological Effects of Electromagnetic Fields* (Boca Raton, FL: CRC Press)

Purcell E M, Torrey H C and Pound R V 1946 Resonance absorption by nuclear magnetic moments in a solid *Phys Rev* **69** 37-8

Rakow-Penner R, Daniel B, Yu H, Sawyer-Glover A and Glover G H 2006 Relaxation times of breast tissue at 1.5T and 3T measured using IDEAL *J Magn Reson Imaging* **23** 87-91

Reichenbach J R, Venkatesan R, Yablonskiy D A, Thompson M R, Lai S and Haake E M 1997 Theory and Application of Statistic Field Inhomogeneity Effects in Gradient Echo Imaging *J Magn Reson Imaging* **7** 266-279

Rose A 1948 The sensitivity performance of the human eye on an absolute scale *J Opt Soc Am* **38** 196-200

Scholz B and Anderson R 2000 On electrical impedance scanning - principles and simulations *Siemens Electromedica 2000* **68** 35-44

Schwan H P 1957 Electrical properties of tissue and cell suspensions *Adv Biol Med Phys***5** 147-209

Schwan H P 1963 *Physical Techniques in Biological Research,* ed W L Nastuk (New York: Academic) pp 327-407

Schwan H P and Kay C F 1957 The conductivity of living tissues *Ann N Y Acad Sci* **65** 1007-13

Scott G C, Joy M L G, Armstrong R L and Hankelman R M 1991 Measurement of non-uniform current density by magnetic resonance *IEEE transactions on medical imaging* **10** 362-74

Scott G C, Joy M L G, Armstrong R L and Hankelman R M 1995 Rotating frame rf current density imaging *Magn Reson Med* **33** 355-69

Seeger P G and Wolz S 1990 Succesful biological control of cancer: By combat against the causes *Gesamtherstellung: Neuwieder Verlagsgesellschaft mbH*

Seppenwoolde J H, Vincken K L and Bakker C J G 2007 White-Marker Imaging - Separating Magnetic Susceptibility Effects from Partial Volume Effects *Magn Reson Med* **58** 605-609

Sijbers J, den Dekker A J, Van Audekerke J, Verhoye M and Van Dyck D 1998 Estimation of the noise in magnitude MR images *Magnetic resonance imaging* **16** 87-90

Singh B, Smith C W and Hughes R 1979 In vivo dielectric spectrometer *Med Biol Eng Comput* **17** 45-60

Slichter C P 1978 *Principles of Magnetic Resonance* (New York: Springer) Ch VII

Stark D D and Bradley W G 1999 *Magnetic resonance imaging* (St. Louis: Mosby)

Stevick J W, Harding S G, Paquet U, Ansorge R E, Carpenter T A and Williams G B 2008 Gaussian Process Modeling for Image Distortion Correction in Echo Planar Imaging *Magnetic Resonance in Medicine* **59** 598-606

Stojadinovic A, Nissan A, Gallimidi Z, Lenington S, Logan W, Zuley M, Yeshaya A, Shimonov M, Melloul M, Fields S, Allweis T, Ginor R, Gur D and Shriver C D 2005 Electrical impedance scanning for the early detection of breast cancer in young women: preliminary results of a multicenter prospective clinical trial *J Clin Oncol* **23** 2703-15

Stuchly M A and Stuchly S S 1990 *Electrical Properties of Biological Substances* (Eaglewood Cliffs, NJ, USA: Prentice Hall Inc.)

Surowiec A J, Stuchly S S, Barr J B and Swarup A 1988 Dielectric properties of breast carcinoma and the surrounding tissues *IEEE Trans Biomed Eng* **35** 257-63

Walsh M and Lee M 1991 A review of false negative mammography in symptomatic population *Clinical radiology* **44** 13-5

Wersebe A, Siegmann K, Krainick U, Fersis N, Vogel U, Claussen C D and Muller-Schimpfle M 2002 Diagnostic potential of targeted electrical impedance scanning in classifying suspicious breast lesions *Investigative radiology* **37** 65-72

Wollin E 2004 Apparatus and Method for Magnetic Resonance Measurement and Mapping of Electrical Impedance Complex Permittivity and Complex Conductivity as Applied to Detection and Detection of Sample Pathology. (Int. Patent No. WO2004/019763

World Health Organization Cancer Fact Sheet N297 2006 World Health Organization

Zhang N 1992 Electrical impedance tomography based on current density imaging. In: *Dept of EE, MS Thesis* (Toronto: University of Toronto)

About the Author

Nataliya Kovalchuk received a Bachelor's Degree in Physics from Drohobych State University, Ukraine in 2002 and M.S. in Physics from Minnesota State University, Mankato in 2004. She has graduated with Honors from both Universities, and her Master's Thesis was awarded as the MSU Best Thesis of the Year in 2002. She entered the Ph.D. program at the University of South Florida in 2004. While in the Ph.D. program, Ms. Kovalchuk joined the Digital Medical Imaging Group at the H. Lee Moffitt Cancer Center & Research Institute, where she worked on Magnetic Resonance Electrical Impedance Mammography project. Nataliya Kovalchuk is a coauthor of several publications on this new imaging technique. She also made a presentation on Magnetic Resonance Electrical Impedance Mammography at the 48th Annual Meeting of American Association of Physicists in Medicine in Orlando, FL.